Fakultät für Medizin
Technische Universität München

Gene reporters and actuators based on prokaryotic nano-compartments

Felix Andreas Sigmund

Vollständiger Abdruck der von der Fakultät für Medizin der Technischen Universität München zur Erlangung des akademischen Grades eines

Doktor der Naturwissenschaften (Dr. rer. nat)

genehmigten Dissertation.

Vorsitzender:

Prof. Dr. Radu Roland Rad

Prüfende der Dissertation:

1. Prof. Dr. Gil G. Westmeyer
2. Prof. Dr. Friedrich C. Simmel
3. Prof. Dr. Michael Sattler

Die Dissertation wurde am 23.01.2019 bei der Technischen Universität München eingereicht und durch die Fakultät für Medizin am 8.10.2019 angenommen.

Acknowledgements

First of all, I am obliged to thank my mentor and PhD supervisor Prof. Gil Westmeyer for giving me the unique opportunity to work on these interesting and challenging topics during my PhD. I have always greatly enjoyed the scientific discourse with him that led to new exciting concepts and ideas. From him, I learned that it will always pay off to do all things in the best possible way. I was given exceptional freedom to develop my own ideas, which made me encounter many challenges to overcome but ultimately made me into an independent thinker and researcher.

Second of all, I would like to thank Prof. Friedrich Simmel and Dr. Bernhard Gleich for being members of my thesis committee supporting me with valuable suggestions during our joint thesis committee meetings.

Furthermore, I'd like to thank Dr. Philipp Erdmann and Prof. Jürgen Plitzko for the collaboration on visualizing encapsulins in cells using cryoEM techniques. Also, I would like to thank Prof. Vasilis Ntziachristos and Prof. Dr. Daniel Razansky for the collaborations on genetically-encoded markers for Optoacoustic imaging and supplying institute resources. Also, I would like to thank for Prof. Wolfgang Wurst for supplying all IDG resources that we were kindly allowed to use. A special thanks goes to Dr. Michaela Aichler for help with TEM to visualize Encapsulins in various sample preparations. For support with native MS analysis, I'd like to thank Dr. Tobias Wörner, Dr. Joost Snijder and Prof. Albert Heck. I would also like to thank Prof. Alan Jasanoff and his lab for enabling the encapsulin in vivo work in rats. Another special thanks goes to Dr. Arie Geerlof for his support with protein purification and analysis throughout the years.

In general, I would like to thank my amazing colleagues, that I shared my everyday life with over the years. You made my PhD some much more rich and enjoyable and many of you have become good friends. In particular, I want to thank Christoph Massner, who I first encountered in the lab when I arrived at the lab in summer 2013. We worked closely together on the topic of Magnetogenetics, which was always good fun and resulted in very good publications. He has also sparked my interest in many topics beyond science and has become a good friend. Giorgio Pariani and Carlos Cruz for being great colleagues and semi-decent kicker opponents over the years. I'd also thank Yuanyuan Yiang for the fruitful collaborations and the great support throughout the years. A special thanks goes to Ahne Mylathun, a great scientist and friend from the most beautiful country in the world. Panos Symvoulidis, who was always extremely helpful with any problem you approached him with. I will miss his unconventional way of finding solutions, his great humor and good heart and his scientific vision. Anja Stelzl, who

is the best technician that I have encountered throughout my scientific career and has abilities that go way beyond her profession. Thank you very much for being a great support and a good friend. I'd like to thank Jeff Truong for sparking my thrive to broaden my knowledge in the field of synthetic biology and the initial AviLabel design. A big thanks to Hannes as excellent support for all kinds of experiments and logistics over the years. Another big thanks goes to Susanne, who especially towards the end of my PhD helped me greatly to expand on all topics related to encapsulins. I would also like to thank Silviu Bodea, who joined the lab also close to the end of my PhD but immediately integrated into the lab and reignited my interest in climbing and mountaineering. I feel also obliged to thank my students Leonie, Neha, Ann-Kristin and Moritz for their support. Thanks to all my office mates: Tanja, Elen and Theresa. We always had a good laugh together in between our daily lab routines. A very special thanks goes to Dr. Antonella Lauri, who has become a real friend over the years. She has taught me many important insights about life and has become a (scientific) role-model for me. I would also like to thank my best friend Michl, who became an outstanding scientist. He was always exceptional support when I was feeling down and we have shared so many unforgettable moments together. I would also like to thank my circle of friends in and around Munich: Daniel, Lisa, Wolfi, Maxi and David. I'd like to thank you in particular for being a great support and distraction from the daily routine over the years.

Importantly, I would like to thank my family for being unconditional support during all my life and this PhD. My parents have always given me the freedom to explore all my interests ranging from rocket science to biology, while at the same time giving me the right boundaries and teaching me the importance of values such as respect for oneself and the people around you. Without you, I would not be the person that I am today and I want to thank you for that wholeheartedly.

In the end, I would like to thank all the people that I forgot to mention or cannot mention by their names. You were good companions over all this time without whom I wouldn't have been able to accomplish this PhD. I thank you all.

Abstract

For understanding biological systems in their physiological and diseased state, researchers require tools to image cellular processes with high resolution and penetration depth while at the same time extracting molecular information. Furthermore, to probe causal relationships in cellular networks, complementary tools to manipulate the system non-invasively without perturbing its natural function are demanded.

Existing techniques such as fluorescence imaging in combination with genetically encodable tools such as fluorescent sensor proteins and optogenetics both are powerful tools to study biological systems in detail, however, are limited by the penetration depth of visible light into tissue.

In order to overcome this hurdle, non-invasive techniques for imaging such as magnetic resonance imaging (MRI) and optoacoustic imaging (OA) are being developed. Similarly, actuation techniques based on magnetic fields and near-infrared light are upcoming.

However, there are few robust genetically-encodable tools for these imaging modalities and existing magnetogenetic manipulation tools are highly debated.

Thus, to enrich the genetic toolbox for imaging and actuation based on magnetic fields, we exploit bacterial encapsulins, a class of proteinaceous spherical 32 nm diameter nanocompartments, as tools for molecular imaging and manipulation. By expressing them in mammalian cells, we create auto-assembling orthogonal compartments to which a set of native and engineered cargo proteins can be addressed via a short terminal targeting peptide. Expressing the shell and the native cargo yields mega iron stores in mammalian cells enabling detection via MRI and magnetic manipulation. Importantly, the isotropic nanostructures can be readily detected in cryo-electron tomography (cryo-ET) for which iron loading affords extra contrast.

By targeting a soluble bacterial tyrosinase into the encapsulins, we created synthetic 'nano-melanosomes' that can serve as low-toxicity genetic reporters for optoacoustic imaging.

More generally, we demonstrate that designer multi-component processes can be targeted to the encapsulin lumen in mammalian cells highlighting the generalizability of genetically controlled compartmentalization.

With respect to genetic imaging reporters for optoacoustic imaging, we showcase that bio-synthetic pigments can serve as a novel class of gene reporters. We demonstrate this by expressing the five-gene Vio operon of *Chromobacterium violaceum* encoding five enzymes catalyzing the turnover of L-tryptophane to the colored pigment 'Violacein' in *Escherichia coli*. The pigment features high absorbance extending into near-infrared range and high resistance against photobleaching, which is a requirement for robust detection in optoacoustic imaging. Isolated bacterial suspensions of Violacein-expressing *E.coli* were characterized in a custom built optoacoustic spectrometer and could be ro-

bustly detected *in vivo* in murine tumors in depths up to several millimeters.

In summary, we show that genetically-controlled compartmentalization is a powerful generalizable extension to the mammalian cell engineering toolbox with applications in molecular imaging and manipulation. Furthermore, we introduce a new class of chromogenic gene reporters for optoacoustic imaging that might also be applicable in mammalian cells by targeting all components to the encapsulin lumen possibly yielding better turnover and lower toxicity.

Contents

List of Figures

Acronyms

BOLD	blood oxygen level–dependent.
CC	Coiled-coil.
CNS	Central nervous system.
DAB	3,3-diaminobenzidin.
DNA	deoxyribonucleic acid.
DREADD	Designer receptor exclusively activated by designer drug.
EM	Electron microscopy.
FIB	Focused-Ion-Beam milling.
FMR	Ferromagnetic Resonance.
fMRI	Functional magnetic resonance imaging.
Gd	Gadolinium.
LDLr	low-density lipoprotein receptor.
LGIC	Ligand-gated ion channel.
LRP	Lysine-rich protein.
MEMRI	Manganese-enhanced magnetic resonance imaging.
MnP	Manganese peroxidase.
MRI	Magnetic resonance imaging.
NIR	Near-infrared.
nm	Nanometer.
OA	Optoacoustic.
RF	Radio frequency.
SQUID	Superconducting Quantum Interference Device.
TEM	Transmission electron microscopy.

Tfr	Transferrin receptor.
TRP	Transient receptor potential.
VSM	Vibrating sample magnetometery.

1 Preface

This document is a cumulative dissertation, which was produced during summer 2013 and spring 2019 in the laboratory of Prof. Gil Westmeyer at Technical University of Munich (TUM) in the Department of Nuclear Medicine and the Helmholtz Center Munich in the Institute of Biological and Medical Imaging.

The initial impetus of this thesis was the creation of novel genetically-encodable tools that would allow the imaging and manipulation of biological processes non-invasively. The prime examples for genetic tools that can be utilized for imaging or actuation are the green fluorescent protein (GFP) and the light-inducible channelrhodopsins respectively. They allow imaging protein dynamics within cells and yield activation or inhibition of neurons using photons. Since photons in the visible range cannot propagate deeply in biological tissue, the application of fluorescence-based genetically-encodable tools is limited when deep tissue regions in larger *in vivo* models are targeted.

Therefore, it was set out to develop gene reporters and actuators, that rely on physical principles that can penetrate tissue more potently such as magnetic fields and near-infrared light. First, strategies were developed to produce hyper-magnetic cells, that would be detectable in magnetic resonance imaging (MRI) and manipulable with magnetic gradients. In search of protein components that could make cells magnetic, the applicability of the bacterial iron mega-store protein encapsulin was evaluated in mammalian systems. This initial idea resulted in a comprehensive publication (Sigmund *et al.*, 2018 [1]), where it is demonstrated that bacterial iron-storing encapsulins can be expressed in mammalian cells, which affords their detection in MRI as well as their manipulation in magnetic gradients. More generally, the publication shows that encapsulins expressed in mammalian cells can constitute orthogonal synthetic nano-organelles, that can be genetically programmed to encapsulate tailor-made multi-component processes, which is a fundamental capability for synthetic biology of mammalian cells. Besides detection in MRI, it is also shown that encapsulins can serve as gene reporters for electron microscopy (EM) in mammalian cells and engineered 'nano-melanosomes' based on encapsulins constitute a non-toxic gene reporter for optoacoustic imaging (OA), an imaging modality which utilizes near-infrared (NIR) light for penetrating tissue.

Secondly, a novel gene reporter strategy empowering optoacoustic (OA) bacterial tumor imaging based on enzymatic chromophore generation was developed, which is summarized in Jiang, Sigmund *et al.*, 2015 [2]. Herein, it is shown that an enzymatic cascade catalyzed by five genes from the bacterium *Chromobacterium violaceium* can be transferred to *E.coli*, where they yield large quantities of the chromogenic compound

'Violacein'. Since Violacein has substantial absorption in the near-infrared range and is highly photo-stable, it enables the robust detection of engineered bacteria *in vivo* in murine tumors at depths up to several millimeters. Moreover, it is shown that Violacein possesses anti-tumoral activity. Thus, engineered bacteria producing Violacein could serve as theranostic agents for imaging and treating cancer in the future.

2 Publication Record

This publication-based cumulative dissertation consists of the following peer-reviewed first-author publications:

1. Jiang Y.*, **Sigmund F.***, Reber J., Deán-Ben X. L., Glasl S., Kneipp M., Estrada H., Razansky D., Ntziachristos V., Westmeyer G. G. (2015) 'Violacein as a genetically-controlled, enzymatically amplified and photobleaching-resistant chromophore for optoacoustic bacterial imaging.', *Scientific Reports*. Sci Rep. 2015 Jun 19;5:11048. doi: 10.1038/srep11048 (* = authors contributed equally to this work)

2. **Sigmund F.**, Massner C., Erdmann P., Stelzl A., Rolbieski H., Desai M., Bricault S., Wörner T. P., Snijder J., Geerlof A., Fuchs H., Hrabě de Angelis M., Heck A. J. R., Jasanoff A., Ntziachristos V., Plitzko J., Westmeyer G. G. (2018) 'Bacterial encapsulins as orthogonal compartments for mammalian cell engineering.', *Nature Communications*. Nat Commun. 2018 May 18;9(1):1990. doi: 10.1038/s41467-018-04227-3.

Publications on pre-print servers:

1. **Sigmund, F.**, Massner, C., Erdmann, P., Stelzl, A., Rolbieski, H., Fuchs, H., de Angelis, M.H., Desai, M., Bricault, S., Jasanoff, A., Ntziachristos, V., Plitzko, J., Westmeyer, G.G. (2017) 'Eukaryotically expressed encapsulins as orthogonal compartments for multiscale molecular imaging.' bioRxiv, doi:10.1101/222083

2. **Sigmund, F.**, Pettinger, S., Kube, M., Schneider, F., Schifferer, M., Aichler, M., Schneider, S., Wach, A., Miesgeld, T., Dietz, H., Westmeyer, G.G. (2019) Iron-sequestering nanocompartments as multiplexed Electron Microscopy gene reporters. bioRxiv, doi: 10.1101/516955

Publications as a co-author and manuscripts in preparation:

1. Roberts, S., Seeger, M., Jiang, Y., Mishra, A., **Sigmund, F.**, Stelzl, A., Lauri, A., Symvoulidis, P., Rolbieski, H., Preller, M., Deán-Ben, X.L., Razansky, D., Orschmann, T., Desbordes, S.C., Vetschera, P., Bach, T., Ntziachristos, V., Westmeyer, G.G. (2017) 'Calcium Sensor for Photoacoustic Imaging.' *Journal of the American Chemical Society*, doi:10.1021/jacs.7b03064

2. Massner, C., **Sigmund, F.**, Pettinger, S., Seeger, M., Hartmann, C., Ivleva N., Niessner, R., Fuchs H., Hrabé de Angelis, M., Stelzl, A., Koonakampully, N., Rolbieski, H., Wiedwald, U., Spasova, M., Wurst, W., Ntziachristos, V., Winklhofer, M., Westmeyer, G.G. (2018) 'Genetically controlled lysosomal entrapment of superparamagnetic ferritin for multimodal and multiscale imaging and actuation with low tissue attenuation.' *Advanced Functional Materials* 11, 1706793. doi:10.1002/adfm.201706793

3. **Sigmund, F.**, Myklatun. A., Massner, C., Pariani, G., Mishra, A., Jiang, Y., Roberts, S., Troung, J., Stelzl, A., Rolbieski, H., Ntziachristos, V., Westmeyer, G.G. (2018) Bioengineered high-affinity cell surface receptors for cell manipulation and non-invasive multi-modal in vivo imaging. (in preparation)

3 Introduction

The following chapter is supposed to introduce the reader to the basic concepts of molecular imaging and molecular control of biological systems. Since it is the scope of this dissertation to develop genetically-encodable tools to empower these techniques in mammalian models, I will focus on the state of the art of currently available gene-reporters and molecular actuators that rely on different physical principles and discuss their advantages and disadvantages.

In the second part of this chapter, I will briefly introduce the concept of biological compartmentalization based on proteinaceous nano-compartments found in prokaryotes and discuss the state of the art of genetic manipulation over this fundamental principle from which several molecular marker and manipulation strategies can be derived. **Figure 3.1** shows an overview of molecular imaging and control based on genetic tools introduced in this chapter. **Figure 3.2** shows an overview of biological proteinaceous nano and micro-compartments found in nature that could be exploited for molecular imaging and control purposes and mammalian cell engineering in general.

At the end of the chapter, I will formulate the aims of this dissertation based on the aforementioned.

3.1 Molecular Imaging

Molecular Imaging can be defined as the spatiotemporal visualization of cellular processes at a molecular level allowing to study cellular mechanisms of biological systems in the healthy and diseased state [3, 4].

There are several molecular imaging modalities that function based on different physical principles. For instance, fluorescence imaging and microscopy, which is based on visible light, optoacoustic (OA) imaging, which relies on near-infrared light for excitation and ultrasonic pressure waves for detection, ultrasound (US) imaging, which solely relies on sound for excitation and detection or magnetic resonance imaging (MRI), which is based on magnetic fields and RF-pulses for image generation. Each of these modalities can generate intrinsic contrast in biological tissue, delivering anatomical information. Beyond tissue-intrinsic contrast, contrast can also be generated from synthetic exogenous contrast agents, e.g. a small fluorescent molecule in the case of fluorescence imaging. These exogenous contrast agents can furthermore be targeted by coupling them to specific targeting moieties. Besides synthetic exogenous contrast agents, a large set of

powerful genetically-encodable contrast agents have been developed in the past decades for many of these imaging modalities, which will be covered in the following chapters.

3.2 Genetically Encoded Reporters/Labels

Genetically-encoded reporters or bio-sensors are based on proteins that can be encoded in DNA. Thus, the genetic information of the reporters can be delivered as DNA and integrated into the genome of the model organism or cell line of interest. This allows for a tissue-specific targeting when using tissue-specific promoters [5]. Moreover, genetic targeting not only works on the tissue or cell type level but also extends to the sub-cellular scale by targeting reporters to specific sub-cellular structures by attaching specific targeting signals or fusing them to other proteins that usually localize into the organelle or cellular structure of interest [6]. Furthermore, the integration of the DNA encoding the genetic label into the genome of the model organism supersedes the need to endogenously deliver an agent because the cells produce and replenish their contrast agents themselves and therefore no dilution of the contrast agent is to be expected upon cell division. The most famous and widely used genetically-encodable reporter is the green fluorescent protein (GFP) that has revolutionized cell biology in the past two decades. GFP offers all the advantages mentioned in the paragraph above and will be covered in more detail in the following chapter.

3.2.1 Fluorescence Imaging

Fluorescence imaging is one of the most widely used imaging modalities in bio-medical research that relies on the detection of emitted photons by fluorescent molecules in cells or tissues. Its applications span several scales from optical nanoscopy techniques to full body tomographic fluorescence imaging and are empowered by an impressive set of genetically-encodable fluorescent tools that enable the studying of different cellular and sub-cellular processes [7].

The first genetically encodable fluorescent protein marker is named 'Green Fluorescent Protein' (GFP) and was discovered by Shimomura *et al.*, [8] in the jellyfish *Aequorea victoria* as a fusion to the luminescent protein Aequorin. In the jellyfish, it converts the blue light emitted from the aequorin, which peaks around 470 nm, into green light with a peak emission of around 500 nm. Structural studies of the protein showed that it forms a very stable beta-barrel structure and the internal chromophore is auto-catalytically formed from the three amino acids serine, tyrosine, and glycine. The breakthrough came, when several groups showed that the cloned gene encoding GFP could be heterologously expressed in other cell types and organisms and would show fluorescence without further modification or co-factors [9, 10, 11]. The fact that GFPs could easily be fused to other endogenous proteins to monitor their localization and dynamics is also a hallmark of what turned them into the revolutionizing tools that define how researchers conduct cell biology research today [12]. Another important aspect for its success was that researchers applied rational protein engineering and directed evolution methods to GFP

to yield variants with increased brightness, better quantum yield, faster maturation, more suitable oligomerization states and other optical characteristics of which the latter allowed for multiplexed detection within one cell [13, 14, 15, 16]. Also, its stability and ability to function as a fusion protein partner allowed to generate an impressive set of fully genetic protein bio-sensors that are able to report on all kinds of cellular analytes [6, 17]. One famous example is the genetically-encoded one-component Ca^{2+} indicator 'GCaMP', which is based on a circularly-permuted GFP fused to calmodulin and a calmodulin-binding peptide, which allows monitoring neuronal activity in vivo when expressed in the nervous system of model organisms such as zebrafish [18, 19, 20].

3.2.2 Optoacoustic Imaging (OA)

Optoacoustic imaging (OA) is a hybrid imaging modality that maps the distribution of light-absorbing molecules in tissues by recording ultrasound pulses emitted from absorbing molecules upon excitation using near-infrared (NIR) pulsed-laser illumination in deep tissue regions up to several centimeters at high resolution [21]. Importantly, OA imaging can obtain volumetric and multi-spectral information by using large ultrasound-detector arrays and scanning the samples at multiple wavelengths. By using different wavelengths, it is possible to spectrally un-mix and map the distribution of intrinsic absorbers such as hemoglobin and melanin and even detect changes in blood oxygenation [22].

OA relies on light-absorbing molecules to generate signals and thus requirements for OA gene reporters are simple: (1) The gene reporter has to constitute or generate absorbing molecules in the near-infrared range with high extinction coefficient with a low quantum yield. The lower the quantum yield, the more absorbed energy is converted into mechanical waves that can be picked up with the ultrasound detectors. (2) The probe has to be highly photo-stable since OA requires high-laser energies for excitation of absorbers (3) The reporter has to be non-toxic for the biological system.

Since fluorescent proteins are absorbent molecules by themselves, they can serve as OA gene reports in several biological model systems including *in vivo* models. For instance, the expression of the engineered fluorescent proteins EGFP and a red-shifted variant named mCherry were visualized in *Drosophila melanogaster* and zebrafish [23]. In recent years, near-infrared fluorescent proteins have been engineered from bacterial phytochromes and applied in heterologous systems [24]. For instance, the engineered near-infrared (NIR) fluorescent protein designated 'iRFP' has an excitation maximum around 690 nm, shifting it into the near-infrared window, where the absorption of intrinsic chromogenic biological molecules is low [25]. Besides its NIR absorption, it also has a low quantum yield of around 6 %, which is desired because the of strong non-radiative energy conversion yielding a strong OA signal.

Besides the phytochrome-derived iRFPs, there is also a set of 'GFP-like' fluorescent proteins such as E2 Crimson and its non-fluorescent derivatives aeCP597 and cjBlue,

that have absorption spectra reaching the NIR range and offer advantages in terms of photo-stability and signal generation, while at the same time not requiring co-factors such as biliverdin as in the case of iRFP [26].

However, since the signal generation expected from GFP-like proteins is relatively low because their spectral characteristics are not ideal and their absorption overlaps with highly abundant blood, another approach using switchable fluorescent proteins such as 'Dronpa' was developed that increases the contrast-to-noise (CNR) ratio of switchable fluorescent proteins by temporally un-mixing their photoacoustic signal based on their switching characteristics, which enables their robust detection even when highly absorbing blood is present [27]. Besides Dronpa and its mutant, there is a whole set of switchable fluorescent proteins that can potentially allow for multiplexed temporally-unmixed OA imaging [28]. Besides increasing the CNR, switchable fluorescent proteins have also been exploited to increase the spatial resolution of optoacoustic imaging employing similar principles as in optical nanoscopy [29].

Another class of OA gene reporters is based on enzymatically generated absorbers. The first published system is based on the enzymatic turn-over of a substrate called 'X-Gal', which is a lactose analog, to a blue product (5,5-dibromo-4,4-dichloroindigo) by β-galactosidase, which is encoded by the *LacZ* gene [30, 31]. The resulting blue product is highly absorbing in the spectral region between 600-700 nm, making it an attractive OA probe. Although this genetic system creates strong contrast, it suffers from an inefficient delivery of the substrate *in vivo* [32].

Another potent enzymatic OA gene reporter is based on the enzyme 'Tyrosinase'. It catalyzes the turnover of L-tyrosine into dopaquinone, which then undergoes several auto-catalytic steps yielding the absorbing pigment polymer melanin, which has a wide absorption spectrum extending into NIR range and a high photo-stability [33]. Tyrosinase has been shown to serve as an OA reporter in cell culture [34], in an inducible expression system *in vivo* [35] as well as virally transduced into different tumor models [36, 33]. Importantly, concerns remain about the toxic side effects of tyrosinase overexpression, which was the reason for establishing an inducible expression systems in the first place [34].

3.2.3 Magnetic Resonance Imaging (MRI)

Magnetic resonance imaging (MRI) is a non-invasive imaging technique that uses strong static magnetic fields, magnetic gradients and radio-frequency (RF) pulses to generate images. Most often, the technique maps the distribution of water in samples by using RF pulses to induce a nuclear spin energy transition in protons (present in biological tissues) that yields a discernible RF signal that is being localized by magnetic field gradients [37].

Due to the high penetration depth of magnetic fields into tissue, MRI can obtain images at near-cellular resolution (<100 μm) at a relatively good temporal resolution in living organisms non-invasively yielding good anatomical contrast [38].

However, in order to investigate cellular functions in the context of whole model organisms beyond anatomical information, the development of genetic reporters for MRI based on different contrast mechanisms was necessary. (1) Genetic targeting of reporters allows the monitoring of proliferation and migration of genetically-defined cells. (2) Furthermore, it allows the sequential observation of gene-expression in a certain cell type or tissue. (3) Gene reporters that can translate dynamic cellular processes such as the fluctuation of intracellular calcium concentration into an MR read-out are the highly demanded and are especially valuable tools for neuroscience research [39].

3.2.3.1 Enzyme-based MRI reporters

The first class of MR reporters developed were based on enzymatic reactions. For instance, creatine kinase, the enzyme yielding phosphocreatine while turning over ATP to ADP, was expressed in the liver of mice to report on the expression of the low-density lipoprotein receptor (LDLr). The accumulation of phosphocreatine can be detected in ^{31}P MRI [40, 41]. Furthermore, the well-characterized enzyme β-galactosidase (β-gal) was turned into a semi-genetic MR reporter by combining it with a substrate that upon β-gal cleavage exposes gadolinium (Gd) coordination sites influencing water relaxation time and thus modulating the MR signal [42]. Another enzyme-based MR reporter system is based on the expression of human tyrosinase, leading to higher amounts of melanin, which may be able to bind metal ions, yielding enhanced MR signals when expressed in the human breast cancer cell line MCF-7 [43]. With respect to secreted enzymatic MR reporters, secreted alkaline phosphatase (SEAP) was exploited as a semi-genetic MR reporter. In this system, SEAP cleaves adenosine 2-monophosphate (2'-AMP) generating adenosine, which is then detected by a superparamagnetic iron oxide (SPIO)-based sensor that uses an adenosine-binding aptamer to switch aggregation states yielding a change in T_2 contrast [44]. Similarly, SEAP can also cleave soluble metalloporphyrins yielding less soluble reaction products that can be detected using MRI [45].

3.2.3.2 Iron-based MRI reporters

Besides enzymatic reporters, MR contrast can also be generated by importing and sequestering additional amounts of the metal iron, which in its ferric (3+) state is paramagnetic and expected to enhance T_2 contrast [39].

Since mammalian cells take up iron via the transferrin receptor (Tfr), which takes up ferric iron that is tightly bound to the protein transferrin, an early iron-based gene reporter approach was the over-expression of Tfr in mammalian cells combined with administration of magnetic nanoparticles coupled to transferrin resulting in targeted

uptake and thus an enhanced T_2 contrast [46, 47].

Another way of generating iron-related MR contrast is the expression of additional iron storage proteins such as ferritin. Mammalian ferritin is an ubiquitous iron storage protein that assembles from 24 sub-units into a ∼12 nm diameter spherical assembly that can store up to ∼4500 iron atoms in an antiferromagnetic ferrihydrite form. Mammalian ferritin consists of light chain (L) and heavy chain (H) sub-units of which the heavy chain possesses ferroxidase activity, which can oxidize Fe^{2+} to ferrihydrite [48, 49].

In a number of pioneering studies, different variants of heavy chain ferritin (HHF) were over-expressed in several different cell lines and virally-transduced *in vivo*, generating substantial T_2 changes [50, 51, 52, 53]. Since the ferritin ferrihydrite core is only weakly magnetized, there have been several efforts to design hyper-magnetic ferritins as fully-genetic MR reporters. For instance, a chimeric fusion construct of L-chain and H-chain ferritin connected by a flexible linker (LHFT) showed superior iron loading and enhanced T_2 contrast compared to wild-type ferritin [54, 55]. Subsequently, LHFT was used to visualize neuroblast migration in the olfactory bulb in mice *in vivo* [56]. Similarly, an engineered version of mitochondrial ferritin, which was mutated to localize to the cytoplasm, yielded superior T_2 contrast, when virally-expressed in the mouse olfactory epithelium [57]. Interestingly, the ferritin of the thermophilic archaeon *Pyrococcus furiosus*, which is homo-oligomeric and highly thermostable, was subjected to random mutagenesis in order to screen for hypermagnetic variants in the yeast *Saccharomyces cerevisiae*. The screen yielded variants with five-fold higher MR contrast and better iron-loading efficiency that potentially represent superior genetically-encoded MR contrast agents [58]. A similar screen was conducted in *Escherichia coli*, in which the wild-type *ftnA* of *E.coli* was subjected to random mutagenesis, yielding hyper-magnetic variants affording superior magnetic properties than its wild-type counterparts [59].

Another approach for importing additional iron is the over-expression of the ferritin receptor Tim2d in mammalian HEK293T cells, resulting in increased ferritin uptake from the environment. Upon supplementation of ferritin into the cell culture medium, the resulting cell pellets of Tim2d over-expressing cells showed significantly increased R_1 and R_2 values as compared to control cells [60]. Similarly, the L-chain receptor SCARA5 was used to import gadolinium (Gd) and Curcumin-doped apo-ferritin into different breast cancer cell lines in a theranostic approach [61].

Interestingly, MagA, a gene product found in the magnetotactic bacterium *A. magnetotacticum*, that is hypothesized to be an iron pump in the magnetosome membrane, was heterologously expressed in HEK293FT cells, which showed increased R_2 values upon expression and supplementation with iron [62].

3.2.3.3 Functional MRI reporter genes

With respect to functional imaging, MRI can record cerebral hemodynamics by observing magnetic changes of hemoglobin depending on its oxygenation state [38]. This functional MRI (fMRI) technique is called 'blood oxygen level–dependent' (BOLD) fMRI. Despite the huge impact of this technique, which based on endogenous contrast, on the field of neuroscience, it is only an indirect read-out of neuronal activity and suffers from low signal-to-noise ratios. Thus, genetically-encoded responsive agents delivering a high signal-to-noise MR read-out of dynamic processes are highly demanded.

In a pioneering effort, the Jasanoff laboratory used directed evolution to turn the heme-binding domain of the bacterial cytochrome P450-BM3 (BM3h) into an extracellular sensor for the neurotransmitter dopamine. In an absorbance-based screen, they selected for BM3h variants, that were able to bind dopamine. This binding of dopamine close to the paramagnetic heme iron led to restricted access of water and thereby to an altered MR signal. The authors demonstrated that the sensor could detect induced dopamine release from PC12 cells and *in vivo* in rat via MRI [63]. In a follow-up study, an improved BM3h-derived sensor is utilized to map reward-related lateral hypothalamic brain stimulation-evoked dopamine release in living rats [64]. However, in these studies, the sensor was heterologously produced and injected into the animals, and neuronal expression has not been shown yet.

3.2.3.4 Other novel MR reporter genes

Since the sensitivity of the aforementioned gene reporters is low, other genetically-encodable tools based on other MR contrast mechanisms are being developed to boost sensitivity.

For instance, a contrast mechanism called chemical-exchange saturation transfer (CEST) relying on selective radio-frequency pulses saturating the magnetization of protein exchangeable protons, which due to the rapid chemical exchange with surrounding bulk water protons yielding a reduced water MR signal has been proposed [65]. Since rapidly-exchanging amide protons in poly-L-lysine have been to shown to generate contrast in bulk solution, a set of lysine-rich proteins (LRPs) has been designed as a prototypical CEST gene reporter [39]. In follow up studies, LRPs were used to image virally-transduced tissues via CEST MRI *in vivo* [66, 67].

With regards to hyper-polarization-based MR techniques, the Shapiro laboratory has introduced genetically-encodable bacterially-derived nano-scale gas-vesicles, that can serve as reporters for hyper-polarized ^{129}Xenon MRI, that can still be detected down to the picomolar range [68, 69]. Interestingly, the authors also show that due to the different magnetic susceptibility compared to water, the gas-filled nano-structures can also generate T_2 and T_2* contrast at concentrations in the sub-nanomolar range, that

is erasable upon applying high-intensity ultrasound pulses [70].

Another MR gene reporter approach exploits membrane proteins, that enhance the diffusion rate of water in and out of cells, generating contrast in diffusion-weighted magnetic resonance imaging. For instance, the aquaporin AQP1 over-expressed in different mammalian cell lines yielded robust contrast in diffusion-weighted MRI and could also be robustly detected when xeno-grafted into the brain of mice [71]. The Brindle laboratory showed similar effects upon expression of the water-diffusion rate altering urea transporter UT-B [72].

3.2.4 Electron Microscopy

Electron microscopy (EM) is a microscopy technique that employs electrons to interrogate a sample and has applications ranging from material science to biological samples. Importantly, electron microscopy methods have gained importance in structural biology since it is possible to determine protein structures down to atomic resolutions of several Å in a single-particle analysis of protein complexes [73]. Furthermore, it is now possible to observe proteins in their cellular environment by combining Focused-Ion-Beam milling (FIB) of plunge-frozen cellular samples with subsequent cryo-electron tomography (cryoET) of the resulting lamella [74]. Another important application besides *in situ* structural biology with regards to biological research is 'Connectomics' research. Connectomics aims to obtain a 'wiring diagram' of all neurons in the nervous system of a model organism and is considered a necessary intermediate step to understand the brain as a whole. There is a lot of research on how to decipher connectomes using fluorescence-based methods but only EM delivers the required resolution to capture all neuronal components such as the number of synapses [75].

In order to label a certain cell type or a sub-cellular structure in EM, several (semi-)genetic marker strategies have been developed in the past years. Most of the EM reporters currently described rely all on the same principle: They catalyze a localized chemical reaction that yields an electron dense phase that generates additional contrast in EM [75]. The most widely employed class is based on the enzyme peroxidase. For instance, endogenously added horseradish peroxidase (HRP) has already been used in the 1970s for axonal tracing [76]. However, its applicability as a genetically-encodable tag was limited by that fact that it was not functional in the reducing environment of the cytosol because of impaired disulfide-bond formation. This obstacle was overcome by the usage of an ascorbate peroxidase (APX) from pea, that was shown to be functional when produced in the cytosol [77]. The engineered protein named 'APEX' generates contrast in EM by locally catalyzing the polymerization of 3,3-diaminobenzidine (DAB) creating osmiophilic polymers attracting osmium, which is used in EM counter-staining. In a follow-up study, APEX was further improved using a directed evolution scheme, which aimed to screen for variants that have a higher catalytic activity under EM conditions [78]. For instance, APEX2 has been employed to stain the sub-mitochondrial protein MICU1 effectively. Another genetically-encoded EM reporter is based on a

small fluorescent flavoprotein from Arabidopsis, that upon light exposure generates singlet oxygen, which then catalyzes the polymerization of DAB, yielding an osmiophilic electron dense precipitate, as in the case of APEX. This EM tag named 'miniSOG' has been shown to be functional when fused to the pre-synaptic protein SynCAM1, allowing to stain pre-synapses in cultured neurons in EM [79]. Furthermore, there are genetically-encoded EM-tags, that are based on heavy-metal binding proteins called 'metallothioneins'. These small proteins can be fused to other cellular proteins, like a GFP, and afford extra contrast when the plastic sections are treated with heavy metal solutions such as gold or zinc. The authors use these labels to stain microtubules in EM selectively [80].

3.3 Genetic/Molecular Actuation Techniques

In order to empower closed-loop control over cellular systems to gain causal insight in their function, genetically-encodable tools to control the biological system are demanded in addition to reporter genes for non-invasive molecular imaging [81]. Indeed, in the past decade, several genetic tools have been developed to tune the activity of cells, particularly in the context of neuronal cells.

3.3.1 Pharmacogenetics/Chemogenetics

Shedding light upon casual relationships between different neuronal cell types and behaviors and physiology is a key capability to understand the brain as a whole. An elegant approach for perturbing neuronal activity is based on the application of small molecules to either evoke or inhibit neuronal firing by acting on engineered proteins, which goes by the name of 'Chemogenetics' or 'Pharmacogenetics' [82].

3.3.1.1 Chemogenetic control of ion channels

Ligand-gated ion channels (LGIC) have been early on widely used to elicit ion fluxes in neurons and controlling animal behavior. For instance, agonists for GABA (4-aminobutanoic acid) and glutamate receptors have been injected intracranially to perturb neuronal activity [83, 84]. However, this method relies on the locally targeted injection to the region of interest and suffers from the lacking orthogonality due to the widespread expression of these receptors in neuronal tissues.

In order to overcome this drawback, several strategies for the ectopic expression of LGICs have been devised: **(1)** For instance, invertebrate ion channels such as *C.elegans* glutamate-gated chloride (GluCl) channels, that can be activated with the anti-parasite drug ivermectin (IVM), were heterologously expressed in mammalian brains yielding neuronal inhibition upon application of IVM [85]. In order to achieve better orthogonality, GluCls have been engineered for lower affinity towards the abundant neurotransmitter glutamate, whereas the affinity towards IVM remained almost unperturbed [86]. Similarly, the mammalian glycine receptor has been rendered responsive to IVM

by introducing several point mutations, making it a useful tool for silencing neurons with improved kinetics [87]. **(2)** Another approach for perturbing neuronal activity is the ectopic expression of mammalian LGICs. However, this method also suffers from the lacking orthogonality because these ion channels are also endogenously expressed. Therefore, this system requires to be used in the context of global knock-out backgrounds. For instance, the cation-conducting channel TRPV1 can be selectively activated by the small lipophilic compound capsaicin, which is responsible for the spiciness of red peppers. Hence, TRPV1 has been used in *TRPV1 -/-* mice to activate dopaminergic neurons by applying capsaicin yielding increased locomotive activity [88]. Interestingly, the zebrafish (*Danio rerio*) TRPV1 is insensitive towards capsaicin [89]. This fact was exploited by expressing the heterologous rat TRPV1 as an orthogonal chemogenetic tool for neuro-modulation and ablation in zebrafish [90].

3.3.1.2 DREADDs (designer receptor exclusively activated by designer drug)

G protein–coupled receptors (GPCRs) are a class of membrane proteins that are important signal transducing molecules in neuronal tissue. Depending on the downstream signaling cascade, these receptors can either excite, inhibit or modulate neuronal activity in other ways [91].

Early on, efforts were undertaken to render GPCRs responsive to synthetic ligands by introducing mutations: For instance, a β2-adrenergic receptor was mutated to bind a synthetic compound designated 'L185,870' (1-(3,4-dihydroxyphenyl)-3-methyl-L-butanone) while at the same time reducing its affinity towards its natural ligand adrenaline [92]. This first generation of designer GPCRs was suffering from several shortcomings such as the low affinity of the ligands towards the receptor, lacking orthogonality because of synthetic ligands still being able to activate the non-engineered receptors, modest signaling efficacy and constitutive activity of the engineered receptor.

In pursuit of a more suited system for *in vivo* applications, the Roth laboratory proposed a system designated 'DREADD' (designer receptor exclusively activated by designer drug) that used directed evolution to select GPCR variants that were exclusively activated by a small inert molecule [93, 82]. The initial engineered receptor was derived from the human M3-muscarine receptor, in which random mutations were introduced. The resulting proteins were expressed in yeast that was grown in media supplemented with the small molecule clozapine N-oxide (CNO) that could only survive when CNO was able to activate the mutated receptors [94, 95, 96]. The molecule CNO was chosen as the activator because of its superior penetration capabilities into to the central nervous system (CNS), its inert pharmacology and its advantageous pharmacokinetics [82]. The first DREADD fulfilling all criteria to serve as an orthogonal chemogenetic tool was designated '*hM3Dq*' (Y149C, A239G) and featured nanomolecular potency, low constitutive activity and low activation by its natural ligand acetylcholine [94]. hM3Dq is selectively coupling to the Gαq signaling pathway and thus yields neuronal activation. Another variant known as '*hM4Di*' coupling to the Gαi signaling pathway causes

neuronal inhibition by activating inward-rectifying potassium channels. Furthermore, a chimeric muscarinic-adrenergic receptor DREADD was created which couples to Gαs actuating neuronal cAMP-signalling [97, 91]. Moreover, another laboratory reported the construction of a mutant M3 muscarine receptor that was able to stimulate β-arrestin signaling selectively [98].

Taken together, these studies demonstrate that DREADDs are powerful orthogonal tools in neuroscience research with plentiful downstream effectors enabling the interrogation of behavioral and physiological outputs upon the manipulation of genetically-defined neuronal sub-types [82]. Notably, it was recently found, that CNO cannot easily enter the CNS and that only the metabolized clozapine is entering the CNS and occupying DREADDs. Since clozapine has many endogenous targets, this might have an impact on the interpretation of many studies based on this technology [99].

3.3.2 Thermogenetics

Since the aforementioned TRP (transient receptor potential) channels are also thermosensitive non-selective cation channels, researchers have also started exploiting them as neuro-modulation tools based on thermal stimuli offering an alternative to chemogenetics [100].

Before employing thermo-sensitive TRP channels, a thermo-sensitive mutant of a Dynamin GTPase involved in endocytosis in the ectotherm *Drosophila melanogaster* has been used to silence neuronal activity and has become a widely employed tool to dissect neuronal circuits in fly [101, 102]. However, since Dynamin re-modeling is also involved in many processes other than neuronal transmission, TRP channels became the focus of thermogenetic tools.

Besides, TRP channels also offer a set of advantages over existing chemically and light-gated ion channels: (1) TRP channels feature single-channel conductance that is three orders of magnitude higher than that of channelrhodopsin [103]. This allows the usage of weaker promoters yielding lower protein levels avoiding heavy over-expression that might cause toxic side effects. (2) Delivering thermal stimuli into small animals such as flies can be non-invasively achieved by switching ambient temperature.

To date, several thermo-sensitive TRP channels are being used as thermogenetic tools: For instance, *Drosophila melanogaster* TRPA1 has been used to drive fly motor neuron activation at temperatures above 25 °C [104]. Furthermore, rat TRPM8 is a cold-responsive ion channel that has been used to drive neuronal activation in flies at a temperature below 18 °C [105]. Similarly, rattlesnake TRPA1 has been used in zebrafish for thermogenetic neuronal control and ablation [90].

Despite the availability of a large number of thermogenetic tools, the technique suffers from several shortcomings: First, the temporal resolution is poor and often reflects the

slow heating kinetics when heating a whole environment. Second, the spatial resolution is very poor, especially when the whole organism is heated. Overall cooling or heating might have adverse systemic effects on the whole organism since all these model organisms are inherently sensitive to thermal changes. Therefore, Thermogenetics can only be viewed as orthogonal, when the stimulus is highly localized. To compensate this shortcoming, researchers have built devices to locally apply infrared (IR) laser pulses to freely walking flies using computer vision yielding highly improved temporal and spatial resolution [106].

3.3.3 Optogenetics

The most famous molecular actuation technique called 'Optogenetics' combines the use of genetic and optical components to elicit or suppress responses in cellular systems. The method is based on the heterologous expression of microbial opsins, a class of light-gated ion channels [107]. These membrane proteins transduce light into ionic currents. In order for this technique to work, many obstacles had to be overcome. For instance, the photocurrents from these opsins were predicted to be small, requiring strong expression and high light intensities to yield efficient neuronal stimulation. However, it was known that neurons are highly sensitive to over-expression of membrane proteins, often resulting in cell death. On the other hand, the high light intensity can also yield cellular toxicity due to photo-toxicity or heating, whereas heating itself could also elicit cellular responses mediated via heat sensitive molecular machinery. Furthermore, expression of microbial opsins in metazoan host cells could result in non-functional aggregates that required fusion strategies to mammalian targeting sequences enabling efficient membrane targeting [108]. Also, the availability and the delivery of all-trans-retinal, a molecule that opsins require to operate, was a concern.

Despite all these obstacles, the Deisseroth laboratory published a proof-of-concept study in 2005 demonstrating that lentiviral-mediated over-expression of Channelrhodopsin-2 (ChR2) of *Chlamydomonas reinhardtii* enables robust light-evoked millisecond-timescale control of neuronal spiking in mammalian neurons [109, 110].

In the following years, the development of robust delivery vectors enabling non-toxic high-level expression and neuronal interfaces for delivering light *in vivo* have ultimately empowered control over behavior in living mammals [111, 112]. These studies have finally substantiated the confidence that optogenetics would be useful for neuroscience research and cellular circuit control in general [113].

There are three classes of opsins, that are being used in the context of optogenetics: (1) Bacteriorhodopsins, that pump protons out of cells upon light exposure, (2) channelrhodopsins that yield the influx of positively charged ions, which in neurons leads to an action potential and (3) naturally occurring chloride channels, that yield a hyperpolarizing current that hinders neurons from firing [113], a feature that cannot easily be

achieved with other techniques such as electrostimulation.

Based on emerging high-resolution crystal structures of channel-rhodopsin [114], researchers have engineered variants that have modified ions conductance [115, 116], altered kinetics, red-shifted peak activation wavelengths and bi-stable characteristics [113].

Despite the many advantages of optogenetics, which enables millisecond control of neuronal spiking and inhibition in genetically distinct cell populations, there is a demand for techniques with higher penetration depth than that of visible light, that do not rely on the insertion of optical fibers into the brain and allow for fully freely-moving animal models.

3.3.4 Magnetogenetics

Since optical approaches have the shortcoming of being limited by the penetration depth of visible light into tissue, researches started exploring other physical principles to evoke cellular responses. Since magnetic fields penetrate deeply into tissue without perturbation, the Pralle laboratory pioneered an approach based on the radio-frequency (RF) heating of synthetic nanoparticles that were tethered to the heat-sensitive ion channel TRPV1 [117]. The radio-frequency magnetic field heating of the tethered particles lead to TRPV1 channel opening, which was monitored via genetically-encoded calcium sensors in mammalian cells. The researchers went on to show that RF-field heating of magnetic nanoparticles could also cause behavioral responses in the nematode worm *C.elegans*. However, in this *in vivo* demonstration, the engineered TRPV1 variant was not expressed and thus RF magnetic particle heating was only acting on the endogenous heat-sensitive proteins of the worm.

Since the approach presented by the Pralle laboratory relies on a genetic component (TRPV1) and a synthetic component (nanoparticles), it can be termed a 'semi-genetic' approach that the requires the exogenous addition of the particles. This can be an obstacle, especially in an *in vivo* situation where deep brain stimulation in larger animal models such as mice are desired. However, the injection of such magnetic nanoparticles into deep brain regions of mice has been accomplished, and magneto-thermal stimulation of neurons that were virally-transduced to over-express TRPV1 via RF magnetic fields *in vivo* has been demonstrated several years later [118].

In an attempt to create a fully-genetic system, the Friedmann laboratory proposed to substitute the synthetic nanoparticles with engineered genetically-encoded ferritin nanoparticles [119, 56]. In their proof-of-concept study, the authors suggest that RF-heating of ferritin particles evokes calcium transients via heat sensitive TRPV1 channels that via a calcium-sensitive promoter can regulate plasma glucose levels by switching on the expression of insulin in xenografted cells. In follow up studies, the authors improve their system by bringing the ferritin particles directly into proximity to the TRPV1 channels via unspecific membrane targeting signals or specifically via a nanobody fused

to TRPV1 recognizing GFP that is fused to ferritin [120]. Furthermore, the authors claim that their system works in fully transgenic animals and that they can also inhibit neuronal spiking by rendering a TRPV1 channel more selective for chloride ions with one point mutation [121]. Similar results were obtained in an independent study, in which the authors employ a fusion protein of the mechanosensitive ion channel TRPV4 and an engineered ferritin [122]. In this study, the authors rely on applying magnetic gradients to evoke calcium transients proposing a magneto-mechanical gating mechanism. The authors propose that their designer protein designated 'Magneto' works in cell culture and even *in vivo* controlling the behavior of mice by just applying a simple bar magnet.

Furthermore, a study in 2016 reports the discovery of a protein complex, that consists of an assembly of an iron-sulfur cluster protein termed 'MagR' which is supposed to have a permanent magnetic dipole moment, rendering it a putative magneto-receptor [123]. The ∼24 nm rod-like complex is shown to interact with cryptochromes (Cry), which are a class of photo-receptors, that are also implicated in the sensing of magnetic fields. Intriguingly, another laboratory claimed that the over-expression of 'MagR' in mammalian HEK293 cells and the nematode worm *C.elegans* renders them sensitive to magnetic fields. They report membrane-depolarization and calcium influx, as monitored via the genetically-encoded calcium sensor GCaMP6s when they expose HEK293 cells and cultured hippocampal neurons to magnetic fields. Beyond that, they show that when expressed in the nervous system of *C.elegans*, they can trigger behavioral responses upon exposure to magnetic fields [124].

All these studies have created a lot of interest into the topic of controlling cells using magnetic fields but all of them await independent reproduction, and the respective genetic constructs are not being used routinely in neuroscience research. In a comprehensive criticism published by Markus Meister, he questions the working mechanism of the published magnetogenetic tools by Stanley and Wheeler and points out that the MagR complex only containing 40 iron atoms cannot have a permanent magnetic dipole moment [125]. Meister notes that all proposed working mechanisms described in these studies disagree with the basic laws of physics by several log units. Interestingly, in the meantime, another group has proposed a gating mechanism the relies on the 'magneto-caloric' effect that could explain the findings of Wheeler *et al.*, 2016 [122] but these results also await independent confirmation [126]. Although magneto-mechanical gating of TRP channels fused to ferritin seems to be implausible, another study shows that the gating probabilities of PIEZO channels can be modulated when large exogenously-added magnetic particles are tethered to it and actuated via an electromagnetic needle [127].

3.3.5 Sonogenetics

Another promising approach for non-invasive cellular control relies on ultrasonic pressure waves. It has been recently shown that low frequency, low-intensity ultrasound that can non-invasively propagate through bones and tissue to reach even deep brain regions, can modulate neuronal activity making it a powerful tool for basic research and clinical

applications [128]. It was proposed that the underlying mechanism relies on non-thermal effects that act on biological membranes and force-transducing ion channels [129, 130].

However, these systems rely on spatially targeting the ultrasound to a region on interest and lack an orthogonal genetic component that can sensitize specific cellular subtypes. Furthermore, thermal effects might be influencing the stimulation as well. In order to get a genetic handle on this problem, researchers have over-expressed force-sensing TRP-4 channels in the nematode worm *C.elegans* to sensitize neurons for mechanical stimulation via ultrasonic pressure waves [131]. The authors show that they can reliably influence the activity of sensory and interneurons and cause behavioral responses upon exposure to ultrasound. However, to transduce the ultrasound waves into a mechanical stimulus that can be sensed by the TRP-4 channels, synthetic gas-filled micro-bubbles need to be added to the surrounding medium, making the approach semi-genetic only. Also, it is not clear if miss-expression of force-sensitive channels such as TRP-4 in neurons, that is also known to respond to thermal stimuli [132], will yield other non-physiological side effects.

Interestingly, in 2016 the IGEM team of Slovenia has presented a fully-genetic approach that is based on the expression of force-sensitive ion channels and bacterially-derived genetically-encoded gas vesicles [68], which substitute the synthetic micro-bubbles *(http://2016.igem.org/Team:Slovenia)*. However, the proposed system still awaits publication in a peer-reviewed research journal.

3.4 Prokaryotic encapsulins

Compartmentalization is a basic principle in biology that is represented on different scales: Starting from organs to tissues down to cells and even smaller sub-cellular organelles. The different compartments are usually required to create and preserve localized reaction conditions and detach anabolic from catabolic actions. In eukaryotic organisms, sub-cellular compartments such as lysosomes or peroxisomes are usually enclosed by a lipid bilayer [133]. In prokaryotes, however, such membrane-enclosed organelles are sparse with some exceptions such as the membrane-surrounded magnetosome or mesosomes. Interestingly, nature has evolved proteinaceous semi-permeable micro and nano-compartments in prokaryotes. One class of these prokaryotic proteinaceous nano-compartments is named 'encapsulins' and will be covered in more detail below.

Encapsulins are a class of proteinaceous nano-compartments that are structurally related to the HK97-like major capsid protein of archaeal and bacterial viruses [134, 135]. They have been reported to assemble into T=1 (18-24 nm diameter) and T=3 icosahedral semi-permeable capsids [136, 137, 138]. Interestingly, these encapsulins are filled with cargo proteins that are specifically enriched inside their lumen via a short C-terminal targeting sequence [136]. The encapsulins of *Myxococcus xanthus* [138], *Thermotoga maritima* [136] and *Rhodospirillum rubrum* [139] have been shown to carry ferritin-like

cargo proteins (Flps) whereas the encapsulin system of *Pyrococcus furiosus* [140] employs a Ferritin-like-protein (Flp)-shell fusion. For the Flp of *Rhodospirillum rubrum*, it was shown that it adopts an 'open' decameric assembly that is structurally different to canonical four-helix bundle ferritins [139].

Besides ferritin-like cargo-proteins, the encapsulins of *Brevibacterium linens* [141], *Mycobacterium tuberculosis* and *Rhodococcus erythropolis* [142] have been shown to enclose DyP-type peroxidases that were also hypothesized to play a role in oxidative stress response. Recently, it was demonstrated that encapsulation of enzymatic reactions in proteinaceous nano-compartments in bacteria and archaea is much more common than previously thought. Systematic bioinformatic and phylogenetic analysis has revealed hundreds of new encapsulin-cargo systems [137]. Furthermore, previously unknown cargotypes responsible for different functions were described: (1) Hemerythrin-like cargo, that is anticipated to adopt a 4-helix bundle structure and was suggested to be involved in O_2 and NO sensing and in responses to oxidative stress. (2) A novel iron-mineralizing 4-helix bundle cargo protein found in firmicutes (IMEF), conferring protection against oxidative stress. (3) A nitrite-reductase-hydroxylamine oxidoreductase (NIR-HAO) fusion protein cargo found in bacteria that carry out anaerobic ammonium oxidation (anammox). Furthermore, a number of secondary cargo proteins including Ferredoxins (Fer), that can be located outside the core operon, have been identified. Interestingly, all these newly discovered encapsulin-cargo systems have been heterologously expressed in *E.coli* indicating a robust and conserved mechanism for their auto-assembly into nano-compartments [137].

3.4.1 Encapsulins as prokaryotic iron stores

Interestingly, Sutter *et al.*, 2008 [136] already found that the cargo protein of the *T.maritima* T=1 encapsulin system adopts a ferritin-like fold. However, it was not experimentally shown that iron is actually being mineralized inside the encapsulin lumen. Similarly, Akita *et al.*, 2007 [140] solved the structure of the *P.furiosus* T=3 encapsulin but focused on structural characterization and only speculated on its N-terminal fraction, which later turned out to be a ferritin-like protein fused to the shell monomer. Although there were many hints that some encapsulin systems actually could bio-mineralize iron, the first experimental evidence was presented by McHughs *et al.*, 2014 [138] that the encapsulin system of *M.xanthus*, which also contains ferritin-like cargo proteins, actually contains iron-rich phases in its interior when the bacteria were exposed to oxidative stress conditions. The iron-rich cores were shown by electron microscopy of purified compartments. The authors found that the encapsulins contained about 30,000 iron atoms on average, which is about one order of magnitude more than what can be stored in mammalian ferritins, making it the largest iron-storing protein complex found in nature to date. Besides encapsulin systems harboring ferritin-like cargo proteins, there is a recently described encapsulin system found in firmicutes that contains a four-helix bundle protein (IMEF) that does not have a canonical ferritin or half-ferritin like fold but is also able to bio-mineralize iron as shown in *E.coli* [137].

3.4.2 Genetic engineering of encapsulins

Since the terminal targeting peptides (TPs) of encapsulin cargo proteins are well conserved, several studies have demonstrated that loading of foreign cargo protein is possible when expressed in other bacterial hosts. For instance, it was shown that the encapsulin of *Brevibacterium linens* could be filled with the foreign cargo protein teal fluorescent protein (TFP) by fusing it to the C-terminal portion of DyP when expressed in bacterial hosts [143, 144]. Similarly, it was demonstrated that the encapsulin of *Rhodococcus erythropolis* could encapsulate the foreign guest proteins EGFP and firefly luciferase when the 37-amino acid C-terminal portion of *R. erythropolis* N771 DypB was C-terminally fused to these proteins [145]. Furthermore, cargo loading of foreign guest molecules was demonstrated for the encapsulin of *Thermotoga maritima* employing a minimal C-terminal targeting motif when heterologously expressed in *E.coli* [146]. With respect to metal-biomineralization, the inner surface of the *Thermotoga martima* encapsulin was equipped with silver-binding peptides that enabled the mineralization of antimicrobial silver nanoparticles highlighting that encapsulins can serve as a platform for the generation of biogenic functional nano-materials [147].

Besides packaging engineered cargo molecules inside encapsulins, it was shown that functionalizing the outer surface with specific targeting signals such as the SP94 hepatocellular carcinoma (HCC) cell binding peptide either via a genetic fusion or chemical conjugation is feasible and enables cell-type specific targeting of encapsulins [148, 149].

Beyond heterologous expression in bacterial hosts, it was recently shown, that encapsulin expression and loading of foreign cargo are also feasible in lower eukaryotes such as yeast [150]. Apart from using encapsulins as intracellular factories or targeting vehicles, encapsulins haven also been secreted from HEK293 cells to present multimeric glycosylated epitopes to serve as highly potent vaccination and immunostimulating tools [151, 152, 153]. Moreover, it was shown that expressed encapsulins of *Pyrococcus furiosus* that were functionalized with fluorescent proteins in a fusion construct could serve as a tool to study cellular microrheology [154].

3.4.3 Other proteinaceous nano- and microcompartments

Besides encapsulins, there is several other natural and non-natural proteinaceous nano- and microcompartments that have been used as platforms for bioengineering. For instance, the capsid of the cowpea chlorotic mottle virus (CCMV) has been used to encapsulate single molecules of horseradish peroxidase [155]. Similarly, the CCMV capsid has been equipped with iron binding sites on its inner surface to yield iron mineralization [156]. Moreover, the capsid of the bacteriophage P22 has been shown to be a promising scaffold for generating functional nanomaterials: It was shown to be able to accommodate fluorescent proteins, enzymes, and even multi-enzymatic cascades [157, 158, 159, 160]. Besides, these virus-like particles (VLPs) that are in the nanometer size range, there are several types of larger bacterial microcompartments

such as carboxysomes and Eut compartments. Both scaffolds have already been genetically engineered to load foreign cargo proteins such as fluorescent proteins or enzymes [161, 162, 163, 164]. Regarding targetable proteinaceous nanostructures in mammalian systems, vault proteins (vaults), which are hollow elongated ribonucleoprotein complexes of 60 nm in length, have been genetically-modified to load non-endogenous cargo proteins such as enzymes or fluorescent proteins [165, 166, 167, 168]. With respect to the bottom-up design of proteinaceous compartments, it was shown that amphiphilic fusion constructs consisting of repeats of hydrophilic and hydrophobic elastin-like protein (ELPs) derived peptides fused to mEGFP yielded compartments of several hundred nanometers upon expression in *E.coli* [169]. Interestingly, the Baker Lab has accomplished to *de novo* design megadalton scale icosahedral capsid-like structures that auto-assembly in cells and were designed to encapsulate their own RNA-genome [170, 171, 172].

3.5 Aims of this dissertation

This impressive set of genetically-encodable tools has revolutionized the way how biological systems are monitored and perturbed to study how they function as a whole. Interestingly, the most widely used genetic tools are based on fluorescence, which is however limited by the shallow penetration depth of visible light into tissues of intact organisms. Therefore, this dissertation work had the goal to develop genetics tools for imaging and actuation that are based on other physical principles such as magnetic fields and near-infrared radiation that can penetrate biological tissue more readily and would allow for non-invasive imaging and actuation in *in vivo* models.

In that respect, magnetic fields are particularly interesting because their penetrating capabilities into tissue are basically unlimited. Although literature contains several reports on how, for instance, genetic systems based on ferritin can function as an MR imaging reporter and more interestingly, as a 'magnetogenetic' actuators to switch on and off neurons *in vivo* [119, 120, 121, 122], their performance is limited, their working mechanisms are highly debated and independent reproductions are missing [173, 125].

Motivated to create superior genetic tools for imaging and cell manipulation using magnetic fields, for which their working mechanism can be explained based on classical physics, it was set out to evaluate the bacterial nano-compartment-forming iron-storing protein encapsulin of *M.xanthus* in the context of its ability to yield an iron storage in mammalian cells that can empower magnetic resonance imaging and cell manipulation in *in vivo* models.

Since compartmentalization is a fundamental principle in biology, the work furthermore set out to expand on the concept of genetically-controlled generation of orthogonal cellular compartments in the context of (1) it as a fundamental capability for broad use within synthetic biology, (2) as a reporter for other imaging modalities also those on the

other side of scales such as electron microscopy (EM) and (3) translational research.

Moreover, another aim was to develop gene reporters to empower the non-invasive imaging modality optoacoustics (OA), that is based on the enzymatic turnover of readily available cellular substrates into absorbing small molecule chromophores featuring near-infrared absorption. In particular, the biosynthetic pathway leading to the the violet pigment Violacein found in *Chromobacterium violaceum* was supposed to be translated to *E.coli* and optoacoustic performance as well as the applicability in bacterial tumor imaging also in the context of theranostic approaches was supposed to be evaluated.

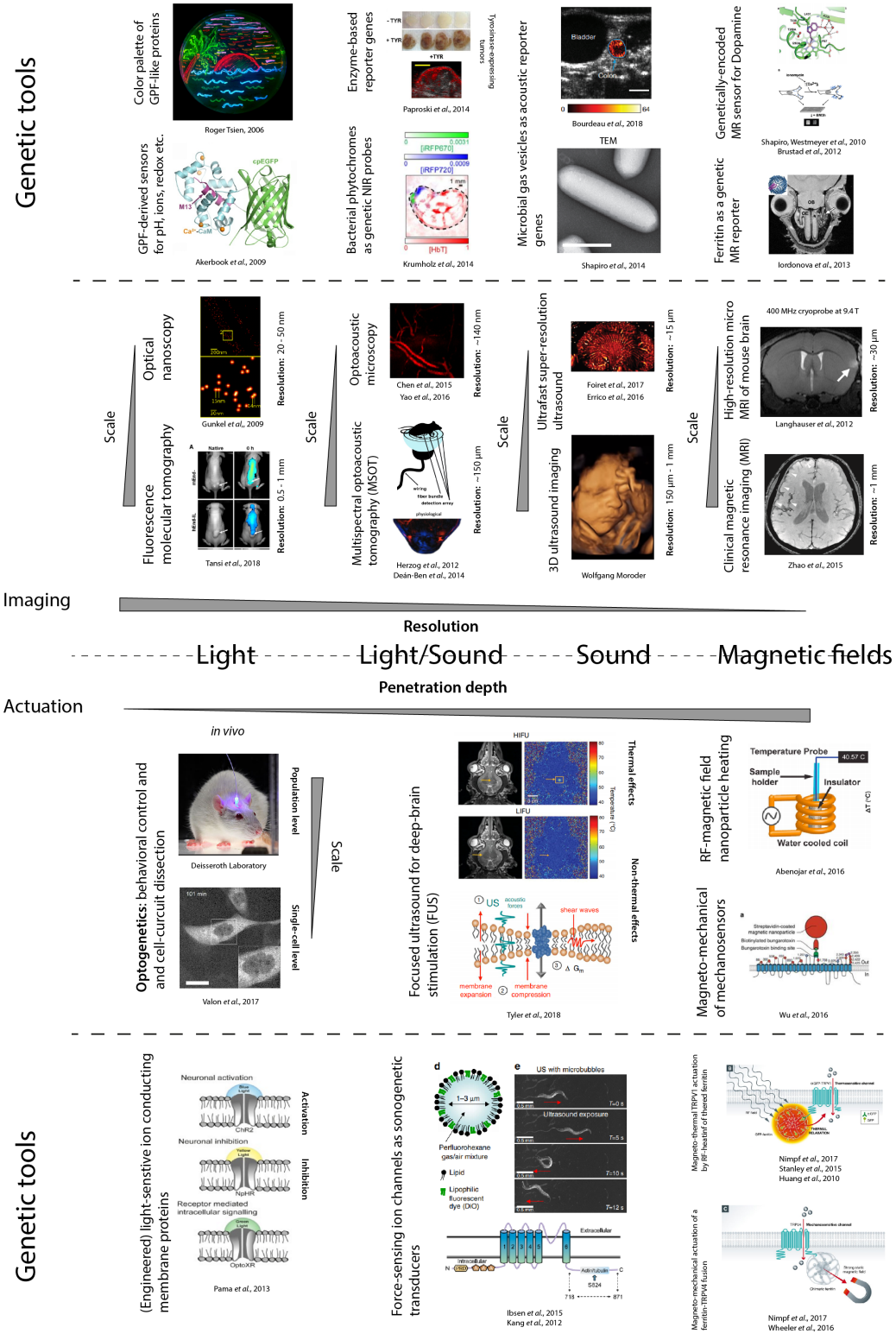

Figure 3.1: An overview of existing genetically-encodable tools for molecular imaging and manipulation based on different physical principles.

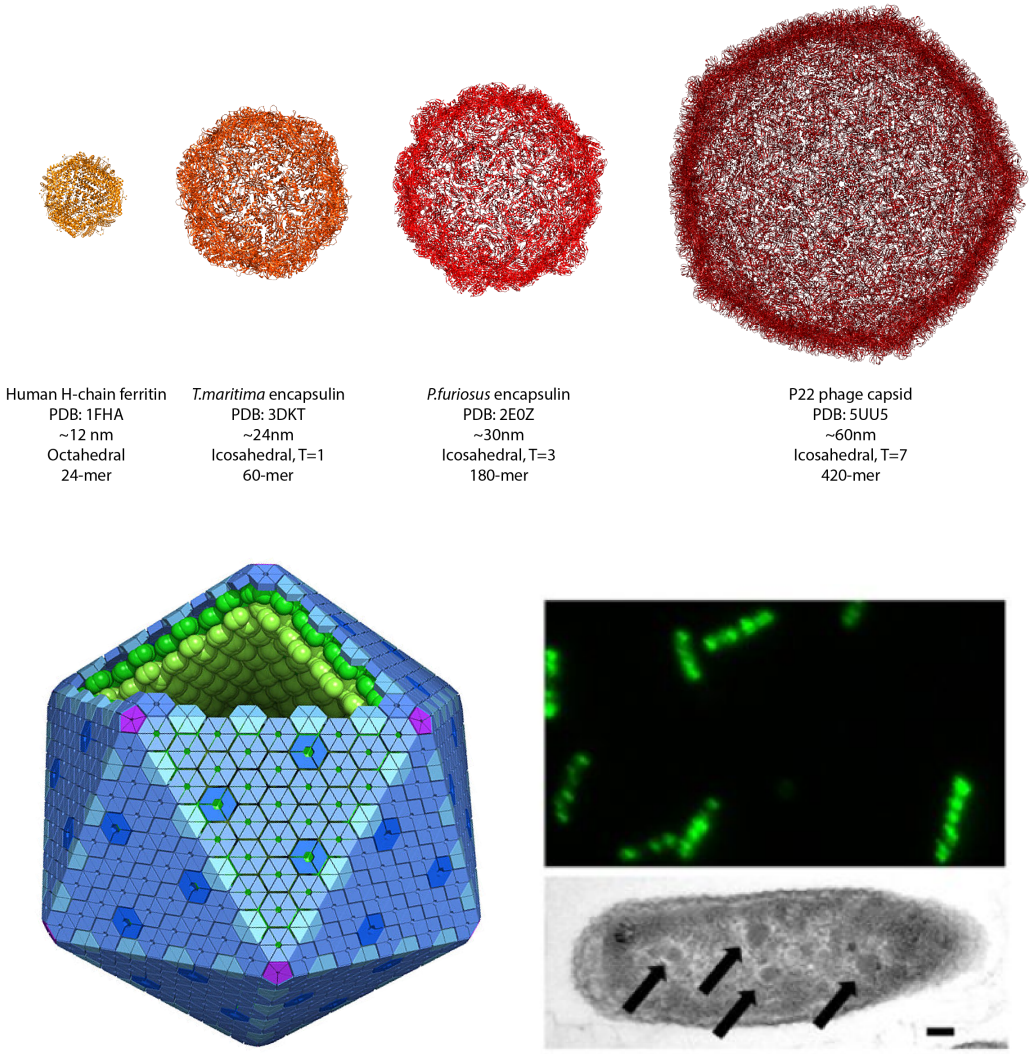

Figure 3.2: An overview of proteinaceous nano and micro-compartments found in prokaryotes.

4 First author publications

The following chapter contains the peer-reviewed first-author publications that summarize the work conducted during my PhD and make this thesis eligible as a cumulative dissertation. Before the actual publication, a brief introduction summarizing the respective work is given, and my individual contributions are specifically named.

4.1 Bacterial encapsulins as orthogonal compartments for mammalian cell engineering

The publication entitled '*Bacterial encapsulins as orthogonal compartments for mammalian cell engineering*' [1] represents the core of this dissertation. It contains an extensive collection of experiments and characterization that comprehensively demonstrate that heterologous expression of bacterial nano-compartments called 'encapsulins' allows the generation of genetically-programmable compartments with multiple applications in molecular imaging and actuation as well as in synthetic biology of mammalian cells in general.

Motivated by the general interest of generating hyper-magnetic cells, I came across an article about these large iron-storing proteinaceous nano-compartments that bacteria use during oxidative stress conditions [138]. I reasoned that these compartments would also assemble, load cargo proteins and bio-mineralize iron in mammalian cells. To this end, I generated all the expression constructs mentioned in the paper enabling mammalian expression of the encapsulin system of *Myxococcus xanthus* with its endogenous cargo proteins and as well as large sets of engineered cargo proteins.

Specifically, I designed all DNA constructs used in the study including all engineered cargo proteins. Furthermore, I designed and conducted all molecular-biology related experiments shown in the paper including all gel analyses, Western-Blots, fluorescence (and bright-field) microscopy images, toxicity assays, stable cell line generation and magnetic sorting. Furthermore, I generated the cells used in MR studies and assisted in sample preparation and MR measurements.

nature COMMUNICATIONS

ARTICLE

DOI: 10.1038/s41467-018-04227-3 OPEN

Bacterial encapsulins as orthogonal compartments for mammalian cell engineering

Felix Sigmund[1,2,3], Christoph Massner[1,2,3], Philipp Erdmann[4], Anja Stelzl[1,2], Hannes Rolbieski[1,2], Mitul Desai[5], Sarah Bricault[5], Tobias P. Wörner[6], Joost Snijder[6,7], Arie Geerlof[8], Helmut Fuchs[9], Martin Hrabě de Angelis[9], Albert J.R. Heck[6], Alan Jasanoff[5,10,11], Vasilis Ntziachristos[1,12], Jürgen Plitzko[4] & Gil G. Westmeyer[1,2,3]

We genetically controlled compartmentalization in eukaryotic cells by heterologous expression of bacterial encapsulin shell and cargo proteins to engineer enclosed enzymatic reactions and size-constrained metal biomineralization. The shell protein (*EncA*) from *Myxococcus xanthus* auto-assembles into nanocompartments inside mammalian cells to which sets of native (*EncB,C,D*) and engineered cargo proteins self-target enabling localized bimolecular fluorescence and enzyme complementation. Encapsulation of the enzyme tyrosinase leads to the confinement of toxic melanin production for robust detection via multispectral optoacoustic tomography (MSOT). Co-expression of ferritin-like native cargo (*EncB,C*) results in efficient iron sequestration producing substantial contrast by magnetic resonance imaging (MRI) and allowing for magnetic cell sorting. The monodisperse, spherical, and iron-loading nanoshells are also excellent genetically encoded reporters for electron microscopy (EM). In general, eukaryotically expressed encapsulins enable cellular engineering of spatially confined multicomponent processes with versatile applications in multiscale molecular imaging, as well as intriguing implications for metabolic engineering and cellular therapy.

[1] Institute of Biological and Medical Imaging, Helmholtz Zentrum München, Ingolstädter Landstraße 1, Neuherberg 85764, Germany. [2] Institute of Developmental Genetics, Helmholtz Zentrum München, Ingolstädter Landstraße 1, Neuherberg 85764, Germany. [3] Department of Nuclear Medicine, Technical University of Munich, Ismaninger Straße 22, Munich 81675, Germany. [4] Department of Structural Biology, Max Planck Institute of Biochemistry, Am Klopferspitz 18, Martinsried 82152, Germany. [5] Department of Biological Engineering, Massachusetts Institute of Technology, 77 Massachusetts Avenue, Cambridge 02139 Massachusetts, USA. [6] Biomolecular Mass Spectrometry and Proteomics Group, Bijvoet Center for Biomolecular Research and Utrecht Institute for Pharmaceutical Sciences, Utrecht University, Padualaan 8, Utrecht 3584CH, The Netherlands. [7] Snijder Bioscience, Spijkerstraat 114-4, Arnhem 6828 DN, The Netherlands. [8] Institute of Structural Biology, Helmholtz Zentrum München, Ingolstädter Landstraße 1, Neuherberg 85764, Germany. [9] Institute of Experimental Genetics, Helmholtz Zentrum München, Ingolstädter Landstraße 1, Neuherberg 85764, Germany. [10] Department of Brain & Cognitive Sciences, Massachusetts Institute of Technology, 77 Massachusetts Avenue, Cambridge 02139 Massachusetts, USA. [11] Department of Nuclear Science & Engineering, Massachusetts Institute of Technology, 77 Massachusetts Avenue, Cambridge 02139 Massachusetts, USA. [12] Chair for Biological Imaging, Technical University of Munich, Ismaninger Straße 22, Munich 81675, Germany. Correspondence and requests for materials should be addressed to G.G.W. (email: gil.westmeyer@tum.de)

Compartmentalization, the spatial separation of processes into closed subspaces, is an important principle that has evolved on several biological scales: multi-enzyme complexes that channel substrates, nanocompartments built entirely from proteins, as well as membrane-enclosed organelles, cells, and organs. Compartments make it possible to generate and maintain specific local conditions that can facilitate interactions and reactions in confined environments[1], such that they can isolate toxic reaction products, protect labile intermediate products from degradation, or separate anabolic from catabolic processes[2]. Whereas eukaryotes possess many membrane-enclosed organelles, membranous compartments are not known in bacteria with a notable exception of magnetosomes in magnetotactic bacteria, in which specific reaction conditions are maintained which enable magnetic biomineralization[3,4]. However, nanocompartment shells built entirely from protein complexes can serve functions in prokaryotes that are analogous to eukaryotic organelles[5].

Intense work has been invested in engineering compartments in prokaryotic systems and yeast to realize features such as substrate channeling for biotechnological production processes[1,6,7]. In contrast, no orthogonal compartments with self-targeting cargo molecules exist to date for use in mammalian cells. Such a system could, for instance, enable cellular engineering of reaction chambers that would endow genetically modified mammalian cells with new metabolic pathways that may include labile intermediate products or spatially confined toxic compounds. Engineered orthogonal compartments in eukaryotic cells may also enable size-constrained synthesis of biomaterials via, e.g., metal biomineralization processes occurring under specific localized environmental conditions.

With regards to protein complexes as building blocks for addressable nanocompartments, viruses and virus-like particles have been expressed in bacterial hosts to encase fluorescent proteins[8–12], enzymes[13–16], and even multi-enzymatic processes[17,18]. Similarly, bacterial microcompartments (BMC) such as Eut microcompartments and carboxysomes have been genetically engineered to load foreign cargo proteins such as fluorescent proteins[19–21]. In mammalian systems, vault proteins (vaults) have been explored, which are ribonucleoprotein complexes enclosed by ~60 nm large envelope structures[22] into which foreign cargo proteins such as fluorescent proteins or enzymes can be packaged[23–25]. However, vaults have openings on both ends and are endogenously expressed by many eukaryotic cells[26]. With respect to protein shell structures that can incorporate iron, the iron storage protein ferritin has been overexpressed to generate MRI contrast under certain conditions although its core size is only ~6 nm containing only ~2000 iron atoms on average per core, which can result in only low magnetization[27–29]. Viral capsids such as the ones from cowpea chlorotic mottle virus (CCMV) have also been equipped with iron-binding sites that lead to accumulation of iron. Expression, assembly, and iron loading in mammalian cells, however, have not yet been demonstrated[30].

In search of a versatile nanocompartment-cargo system for heterologous expression in eukaryotic cells, we were intrigued by the recently discovered class of prokaryotic proteinaceous shell proteins called encapsulins because they possess a set of attractive features: (1) A single shell protein—without the need for proteolytic processing—is sufficient to form comparably large shell-like architectures (~18 nm or ~32 nm) auto-assembled from 60, or 180 identical subunits with a triangulation number (T) of one ($T = 1$) or three ($T = 3$), respectively[31]. (2) The assembled shells are pH resistant and temperature stable[32]. (3) A versatile set of native cargo molecules including enzymes exist that are packaged into shell structures via specific encapsulation signals defined by a short terminal peptide sequence[32]. (4) The pore size of ~5 Å allows channeling small molecular substrates through the shell[33]. (5) *Myxococcus xanthus* (*M. xanthus*) encapsulin was also shown to posses cargo proteins B and C, both containing rubrerythrin/ferritin-like domains as well as highly conserved iron-binding ExxH motifs[31] enabling import and sequestration of iron inside the nanoshell. Ferritin-like cargo proteins adopt an "open ferritin structure" and possess ferroxidase activity[31,33]. A model based on structural data from *Thermotoga maritima* encapsulins (with $T = 1$) assumes that the ferritin-like protein docks into the shell where it obtains ferrous iron through the pores which it then oxidizes for deposition of up to an estimated 30,000 iron atoms per shell in the case of *M. xanthus*[31,33,34]. This amount is an order of magnitude more than can be contained inside a ferritin core expressed in eukaryotic cells. The function of the cargo protein D, on the other hand, has so far not been understood. (6) The termini of the shell protein extend to the inner and outer surface, respectively, such that surface functionalizations are conveniently possible. The outer surface can, for instance, be functionalized to install specific targeting moieties[35–37]. Encapsulin variants were also purified when secreted from HEK293 cells to present glycosylated epitopes for an innovative vaccination approach[38]. Recently, the inner surface of the shell from *T. maritima* was also modified with silver-binding peptides to cause local silver precipitation in *Escherichia coli*, but the ferritin-like cargo was deleted to achieve this feature[39]. (7) Non-native cargo proteins including enzymes can be addressed to the inside of the nanocompartment via a short encapsulation signal[11,40].

This excellent set of studies showed the feasibility and utility of biotechnological production of encapsulins as biomolecular scaffolds and targetable vehicles and probes.

We here introduce engineered encapsulins modified from *M. xanthus* in the context of genetic programming of orthogonal and addressable cellular compartments in mammalian cells. We demonstrate that eukaryotically expressed encapsulins not only auto-assemble at high density and without toxic effects but that self-targeting and encapsulation of cargo molecules still efficiently occur in mammalian cells. We furthermore show localized enzymatic reactions in the nanocompartment useful for optical and optoacoustic imaging, as well as confined iron accumulation within the nanocompartments that labels cells for detection by MRI. Importantly, we also show that encapsulins can serve as excellent gene reporters for electron microscopy due their spherical shape and their ability to load iron. These data demonstrate the value of encapsulins as genetic markers across modalities. In addition, the iron sequestration inside the nanoshells affords magnetic manipulation of cells genetically labeled with encapsulins.

Results

Encapsulin expression and self-assembly. Based on the favorable set of features introduced above, we chose to heterologously overexpress the encapsulin shell protein from *M. xanthus* in HEK293T cells. We tagged the nanoshell with an outward facing FLAG epitope (A^{FLAG}) and found it to express strongly without and with the native cargo molecules from *M. xanthus*, denoted encapsulins B, C, and D[31].

Co-expression of Myc-tagged B, C, or D alone, or a combination of all three non-tagged proteins (via co-transfection or a P2A construct, Fig. 1b), co-immunoprecipitated with A^{FLAG} as visualized on silver-stained SDS-PAGE (Fig. 1c, middle panel). A corresponding western blot against the FLAG (Fig. 1c, upper panel) or Myc-epitope (Fig. 1c, lower panel) confirmed the identities of the protein bands (A^{FLAG}: 32.9 kDa, ^{Myc}B: 18.5 kDa, ^{Myc}C: 15.4 kDa, ^{Myc}D: 12.5 kDa).

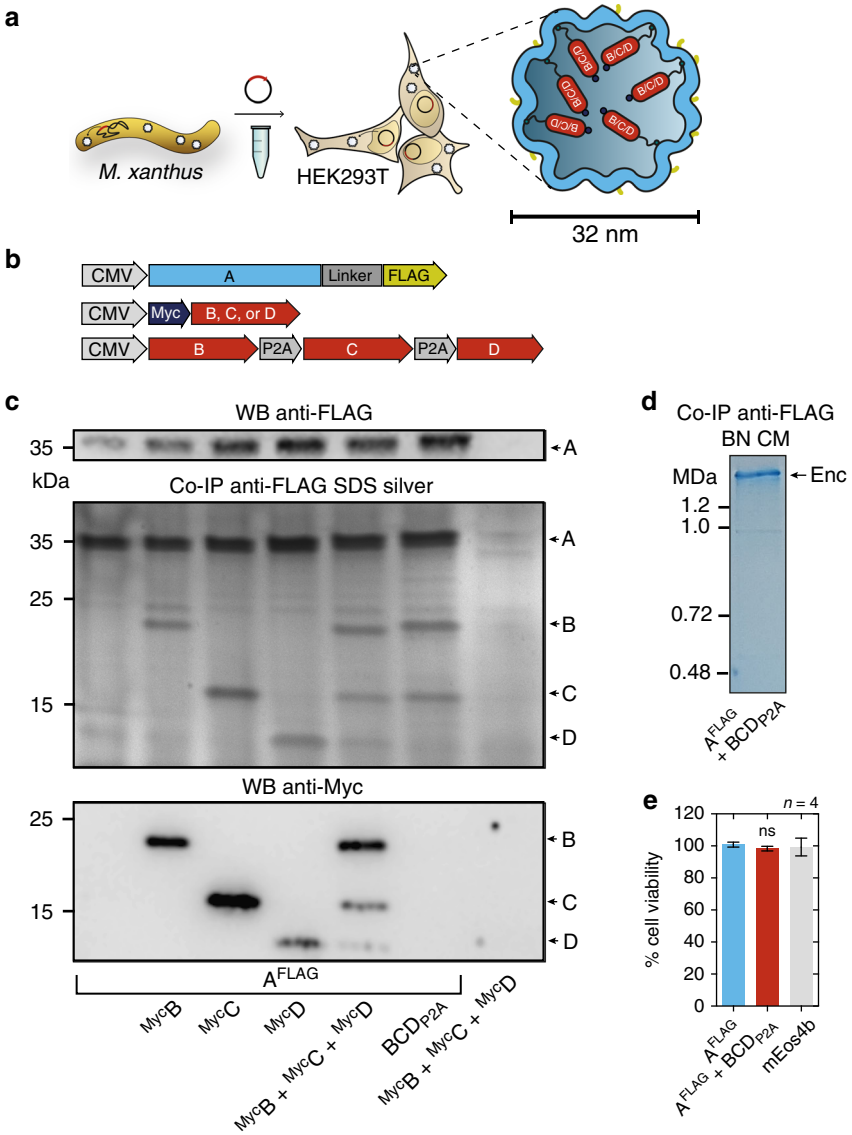

Fig. 1 Assembly of encapsulins and targeting of cargo in HEK293T cells. **a** Schematic of the heterologous expression of surface-modified encapsulin variants loaded with endogenous cargo proteins. **b** Genetic constructs encoding the shell protein A (light blue) with a FLAG-tag as C-terminal surface modification as well as individual Myc-tagged cargo proteins (red) B, C, and D that can also be combined in a multi-gene expression construct (BCD_{P2A}). **c** Co-immunoprecipitation of A^{FLAG} and silver-stained SDS-PAGE from cells co-expressing just B, C, or D, or a combination of these three proteins expressed either via a mixture of individual DNA constructs ($^{Myc}B + {}^{Myc}C + {}^{Myc}D$), or by a multi-gene expression construct (BCD_{P2A}). The top panel shows a western blot (WB) against the exterior FLAG-tag in A^{FLAG}. The bottom panel shows the corresponding WB against the Myc epitope. **d** Coomassie-stained Blue Native PAGE (BN CM) of purified material from HEK293T expressing A^{FLAG} and BCD_{P2A} yielding a band above 1.2 MDa. **e** Cell viability after 48 h of overexpression of encapsulins (A^{FLAG}) with or without cargo (BCD_{P2A}) assessed by an LDH release assay. A construct expressing the fluorescent protein mEos4b served as a control. The bars represent the mean ± SEM ($p = 0.1965$, Kruskal–Wallis, $n = 4$; no significant (ns) differences at $\alpha = 0.05$ were found in Dunn's multiple comparisons test between mEos4b and A^{FLAG} expressed without or with BCD_{P2A})

Furthermore, a corresponding Blue Native PAGE (BN-PAGE) of immunoprecipitated FLAG-tagged material from cells expressing A^{FLAG} together with BCD_{P2A} revealed a band with an apparent molecular weight of above 1.2 MDa indicating self-assembly of encapsulin protein complexes and self-targeting of all native cargo proteins (Fig. 1d).

The strong expression of A^{FLAG} without or with loaded cargo did not result in a reduction of cell viability when compared to cells overexpressing a fluorescent protein as assessed by a viability assay based on lactate dehydrogenase (LDH) release (Fig. 1e).

We also generated a construct for a StrepTagII-labeled variant of the shell that co-expresses the ferritin-like Myc-tagged C as cargo protein via a scarless P2A site[41] ($^{Myc}C\text{-}_{IntP2A}\text{-}A^{STII}$, Fig. 2a). Material from HEK293T cells, conveniently purified via Strep-Tactin affinity chromatography, showed assembled nanospheres of 32.4 ± 1.7 nm as the major component in single particle cryo-electron microscopy (cryo-EM) (Fig. 2b, Supplementary Fig. 1a, b), corresponding to the single band >1.2 MDa in size on BN-PAGE (Fig. 2c, right panel). Again, no effect on cell viability was detected for this construct tested by a luciferase-based viability assay compared to A^{FLAG} with and without cargo (BCD_{P2A}), as well as controls without expression of encapsulins (EYFP and untransfected HEK293T) (Fig. 2d). Furthermore, N-terminal addition of the human BM40 (osteonectin SPARC) secretory signal peptide (SP) to the StrepTagII-modified encapsulin shell protein resulted in entry into the secretory pathway and robust

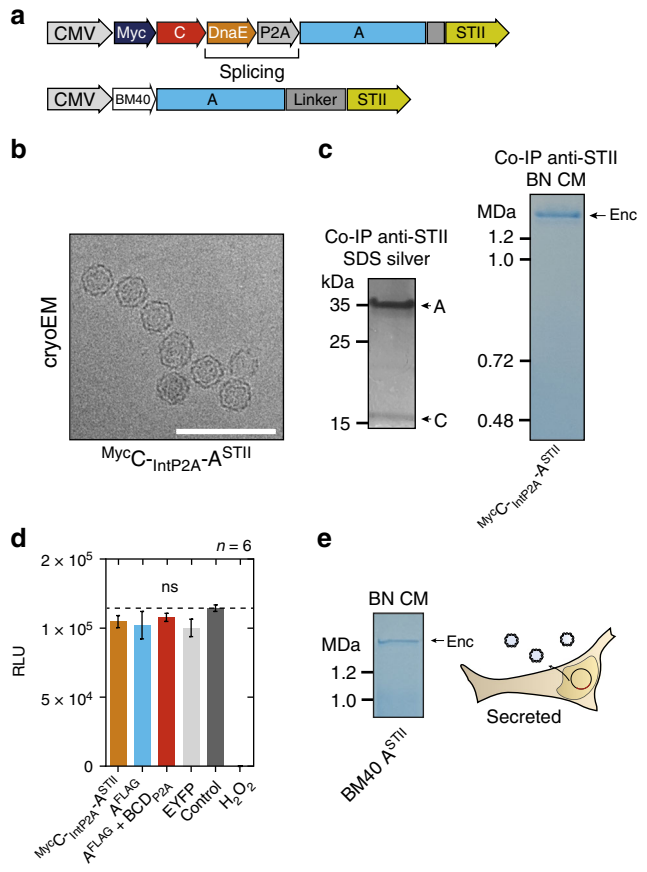

Fig. 2 Combined encapsulin:cargo construct and secreted encapsulin variant. **a** Scheme of a P2A bicistronic expression construct encoding StrepTagII-tagged (^{STII}) nanocompartments containing Myc-tagged C as cargo protein (^{Myc}C-$_{IntP2A}$-A^{STII}) as well as a variant with an N-terminal BM40 secretion peptide and StrepTagII (^{STII}). **b** Cryo-electron microscopy image of material from HEK293T cells expressing ^{Myc}C-$_{IntP2A}$-A^{STII} purified via Strep-tag II/Strep-Tactin XT affinity chromatography showed the assembled nanospheres of ~32 nm diameter. Scale bar is 100 nm. **c** The corresponding BN-PAGE analysis of the identical material revealed a single band larger than 1.2 MDa. The accompanying silver-stained SDS-PAGE showed the coprecipitation of the cargo ^{Myc}C with the StrepTagII-modified nanoshell. **d** Luciferase-based cell viability assay after 48 h of overexpression of ^{Myc}C-$_{IntP2A}$-A^{STII} and A^{FLAG} with or without cargo BCD$_{P2A}$. Cells overexpressing the fluorescent protein EYFP as well as untransfected HEK293T cells served as negative controls. To induce toxicity as positive control, untransfected HEK293T cells were treated with 1 mM H_2O_2 24 h prior to the assay. The bars represent the mean ± SEM ($p = 0.442$ excluding the positive control, Kruskal–Wallis, $n = 6$; no significant (ns) differences at $\alpha = 0.05$ were found in Dunn's multiple comparisons test between any of the encapsulin:cargo conditions and either EYFP or Control). **e** BN CM loaded with cell culture supernatant of HEK293T cells expressing A^{STII} with an N-terminal BM40 secretion signal showed a single band >1.2 MDa

secretion of StrepTagII-modified encapsulins from HEK293T cells as shown by Coomassie-stained BN-PAGE of material present in the cell culture supernatant (Fig. 2e).

In vivo expression of encapsulins. To achieve in vivo expression of encapsulins, we generated a coexpression construct that encoded both the nanoshell A^{FLAG} and the ferritin-like protein B from a single plasmid that was small enough to be packaged into an Adeno-associated virus (AAV) (Supplementary Fig. 1c). After transduction of murine brains via intracranial injections of this viral vector co-expressing A^{FLAG} and B^{M7} by a P2A peptide, we observed robust neuronal expression of the shell protein (Supplementary Fig. 1f, i). Silver-stained BN-PAGE and SDS-PAGE of immunoprecipitated (anti-FLAG) proteins extracted from murine brain showed that the nanocompartments assembled in vivo and that the cargo B^{M7} was associated with the shell (Supplementary Fig. 1g, j). Similar in vivo results could be obtained by co-expressing the nanoshell and ferritin-like B cargo via an IRES site (Supplementary Fig. 1h).

Encapsulation of engineered cargo. We next tested whether non-natural cargo molecules could be efficiently targeted into the nanocompartments. We thus C-terminally appended a minimal encapsulation signal, which we found to only necessitate eight amino acids (EncSig), to the photoactivatable fluorescent protein mEos4b[42], coexpressed it with A^{FLAG} and found by co-immunoprecipitation and BN-PAGE analysis under an UV imager that the cargo readily associated with the encapsulin shell (Fig. 3b).

Selective degradation of non-encapsulated cargo proteins. Importantly, we could also selectively enrich cargo proteins to the encapsulin lumen by fusing an FKBP12-derived destabilizing domain (DD) that labels the cargo for rapid degradation unless it is shielded from proteasomal machinery[43]. We show that co-expressing A^{FLAG} and DD-mEos4b-EncSig in HEK293T yielded significantly higher mean fluorescence values than DD-mEos4b-EncSig alone, indicating that cargos inside the encapsulin are protected from proteolytic degradation (Fig. 3c, d). Confocal microscopy revealed that coexpression of DD-mEos4b-EncSig with A^{FLAG} shows green fluorescence throughout the cytosol but not in the nucleus, whereas the absence of the encapsulin shell ablated the fluorescence signal. In a positive control in which DD-mEos4b-EncSig was stabilized by adding a small molecule instead of encapsulating it, fluorescence was observed throughout the cell including the nucleus (Fig. 3e).

We then purified encapsulins co-expressed with and without DD-mEos4b-EncSig as cargo to determine their native mass and found that in the absence of cargo, also smaller nanospheres assembled consistent with the known configuration as 60-mers with $T = 1$ symmetry (Supplementary Fig. 2). We estimated that on average ~60 fluorescent proteins per nanoshell were enclosed as confirmed by gel densitometry (Supplementary Fig. 3a, b). We furthermore found that the FLAG-tagged encapsulin shell is phosphorylated (Supplementary Fig. 3c-e).

Simultaneous encapsulation of sets of engineered cargo. We next wanted to assess whether multiple engineered cargo molecules could be encapsulated together. We thus fused the two halves of split PAmCherry1 (PA-s1, PA-s2) to either B or C (B-PA-s2: 27.0 kDa, C-PA-s1: 33.1 kDa) and tested for bimolecular fluorescence complementation (BiFC) within the nanocompartment[44] (Fig. 4a, b). Either of these components could be co-immunoprecipitated with A^{FLAG} as shown by silver-stained SDS-PAGE (Fig. 4b, Supplementary Fig. 4a). The photoactivation of the complemented split PAmCherry1 inside the encapsulins could also be detected via fluorescence imaging of the corresponding BN-PAGE (Fig. 4b, right panel, Supplementary Fig. 4a). Co-expression of both split halves together with A^{FLAG} lead to a strong increase of photoactivatable fluorescent signal throughout the cytosol of HEK293T cells as quantified by confocal microscopy compared to cells that did not express A^{FLAG} (Fig. 4c).

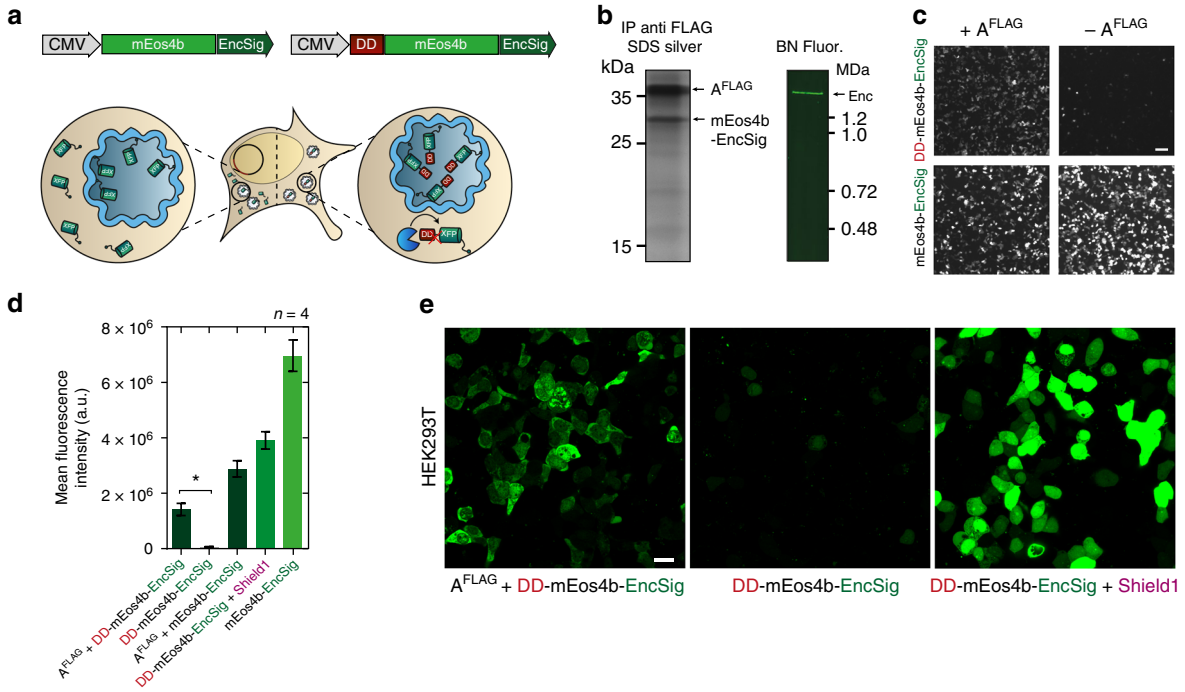

Fig. 3 Selective degradation of non-encapsulated cargo. **a** Schematic of genetic construct showing a minimal C-terminal encapsulation signal (EncSig) fused to the photoactivatable fluorescent protein mEos4b (mEos4b-EncSig) to associate it to the inner surface of the nanocompartment. When mEos4b-EncSig is N-terminally fused to an FKBP12-derived destabilizing domain (DD), it is degraded by the proteasome unless it is sequestered into the encapsulin shell. This strategy thus selectively enriches cargo inside the lumen of the nanocompartment. **b** Cargo loading of mEos4b-EncSig into the nanocompartment composed of A^{FLAG} was demonstrated by co-immunoprecipitation (Co-IP) against the FLAG epitope followed by silver-stained SDS-PAGE (left panel). Corresponding analysis of whole cell lysate by BN-PAGE on a UV imager shows fluorescence of the native encapsulin band indicating the presence of the mEos4b-EncSig cargo. **c** Representative 2 × 2 table of epifluorescence microscopy images from HEK293T cells co-expressing DD-mEos4b-EncSig with or without A^{FLAG} (upper row) compared to coexpression of the cargo without destabilizing domain (mEos4b-EncSig, lower row). Scale bar represents 50 µm. **d** Corresponding quantification of the fluorescence intensities as exemplified in **c**. Co-expression of A^{FLAG} significantly protects degradation of DD-mEos4b-EncSig ($p = 0.0286$, Mann–Whitney test, $n = 4$ biological replicates, error bars represent mean ± SEM). DD-mEos4b-EncSig can also be stabilized by adding the small molecule Shield1 (0.5 mM, magenta label) to the cell culture medium. **e** Confocal microscopy images of HEK293T expressing DD-mEos4b-EncSig with or without A^{FLAG}. As a reference DD-mEos4b-EncSig was stabilized via the addition of 0.5 mM Shield1. Please note that the contrast of all images was linearly adjusted to the same extent optimizing for the condition shown on the left, which resulted in partial oversaturation of the condition shown on the right. Scale bar represents 20 µm

Compartmentalized enzymatic reactions. To showcase the use of the eukaryotically expressed encapsulins as bioengineered reaction chambers with pores that can constrain passage of reactants and reaction products, we targeted several enzymes to the nanocapsules. In the presence of A^{FLAG}, the split luciferase[45] parts LgBit and SmBit fused to C and B (C-LgBit: 32.7 kDa, B-SmBit: 19.6 kDa) were complemented to functional enzymes as demonstrated by bioluminescence detection from BN-PAGE (Fig. 4d, left) and from total lysate (Fig. 4d, bar graph on the right). Importantly, only very low luminescence signals were detected when the encapsulin shell was not present indicating that using split protein approaches can also ensure confined enzyme activity inside the capsules, in addition to the strategy for selective enrichment of cargo inside the nanocompartment as shown in Fig. 3.

Bioengineered melanosomes as gene reporters for MSOT. We subsequently sought to utilize selective passage of small substrates through the nanoshell to load the compartments with tyrosinase as cargo which is the sole enzyme generating the photoabsorbing polymer melanin from the amino acid tyrosine. Because of these attractive features, tyrosinase has been used as a gene reporter for optoacoustic tomography[46,47], an imaging modality that maps the distribution of photoabsorbing molecules in tissue by locating the ultrasonic waves that they emit in response to local heating upon laser absorption[48,49]. However, melanin production is toxic to cells if not confined in melanosomes, which are membranous compartments of specialized cells[50,51]. We thus chose a soluble tyrosinase from *Bacillus megaterium*[52] that we thought could still be functional as a fusion protein to the native cargo D (^{Myc}D-BmTyr: 47.7 kDa) serving as targeting moiety (Fig. 5a). Indeed we could observe generation of melanin on the BN-PAGE band corresponding to the assembled nanocompartment (Fig. 5b). In cells expressing the encapsulin-targeted tyrosinase and the shell A^{STII}, we observed robust melanin formation by bright-field microscopy without the strong toxicity apparent in the morphology of control cells expressing just the tyrosinase (Fig. 5c, white arrows). Encapsulation of the tyrosinase also led to a significant increase in cell viability as assessed by a luciferase-based viability assay (Fig. 5d). Cells expressing melanin-producing encapsulins were dark in color (Fig. 5e, inset) and thus generated intense photoacoustic signal even when referenced against strongly absorbing synthetic ink with an optical density of 0.2 (Fig. 5e).

Similarly, we showed that the engineered peroxidase APEX2[53] can polymerize Diaminobenzidine (DAB) when targeted to the nanocompartment (APEX2-EncSig; 31.0 kDa) as indicated by the generation of photoabsorbing DAB polymers associated with the BN-PAGE band corresponding to the assembled nanosphere (Supplementary Fig. 4b).

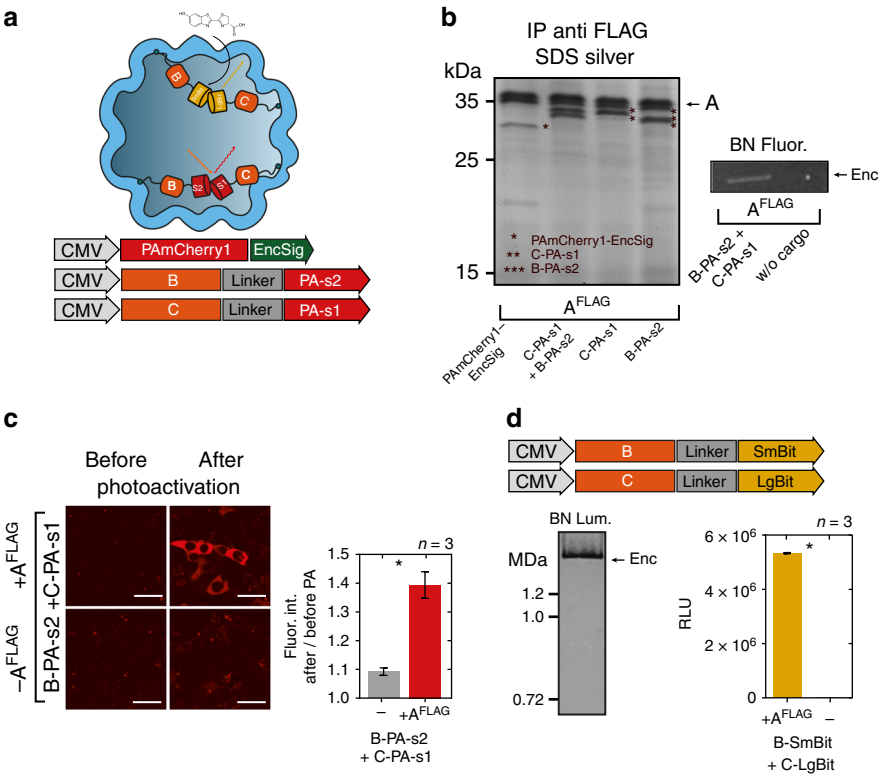

Fig. 4 Multi-component processes and enzymatic reactions can be targeted to encapsulins in mammalian cells. **a** Overview schematic of sets of cargo molecules for bimolecular fluorescence and enzyme complementation inside the nanocompartment. Targeting of foreign cargo proteins can be achieved either via a minimal C-terminal encapsulation signal (EncSig) or via C-terminal fusions to the native cargo proteins B, C, or D. **b** Silver-stained SDS-PAGE from a co-immunoprecipitation (Co-IP) of A^{FLAG} co-expressed with photoactivatable mCherry1 with EncSig (PAmCherry1-EncSig) or with either one of the halves of split PAmCherry1 fused to C or B, or a combination of both (C-PA-s1 + B-PA-s2). Fluorescence originating from complemented split PAmCherry1 inside the encapsulins was detected on BN-PAGE loaded with whole cell lysates of cells expressing A^{FLAG} and C-PA-s1 + B-PA-s2 after 2 min of photoactivation (PA) on an UV imager. **c** Live cell confocal microscopy images (scale bar represents 20 µm) of HEK293T cells expressing B-PAs1 and C-PAs2 with or without the shell-protein A^{FLAG} before and after 60 s of photoactivation (PA) with 405 nm (upper panel) demonstrating efficient bimolecular fluorescence complementation inside encapsulin compartments. Fluorescence of photoactivated split PAmCherry1 was excited using a 561 nm laser. Fluorescence signals of the sample without and with A^{FLAG} were quantified by calculating the ratio of the mean signal after PA divided by the signal before PA. The bars in the lower panel represent the mean fluorescence intensity ratios averaged over independent transfection experiments ± SEM ($p = 0.0123$, unpaired t-test, $n = 3$). **d** Luminescence signal from BN-PAGE incubated with luciferase substrate and loaded with whole cell lysates of HEK293T co-expressing split luciferase fragments fused to either B or C (B-SmBit, C-LgBit) and A^{FLAG} (left panel). The luminescent band corresponds to the complemented split luciferase inside the assembled nanocompartment. The bar graph (right panel) shows the corresponding total luminescence signals from the cell lysates expressing B-SmBit and C-LgBit with or without A^{FLAG}, (mean ± SEM across three independent transfection experiments, in each experiment three technical replicates were averaged, $p < 0.0001$, unpaired t-test, $n = 3$)

Since the electrophoretic mobility of protein complexes on BN-PAGE also depends on their hydrodynamic size and shape[54], cargo-loading could be confirmed by observing an identical migration behavior of loaded as compared to unloaded capsules (Supplementary Fig. 4c).

Moreover, we targeted the putative cystathionine γ-lyase (SmCSE) to the nanospheres via an EncSig (smCSE-EncSig: 43.9 kDa) as shown by Co-IP with A^{FLAG} (Supplementary Fig. 4d). In the presence of L-cysteine, this enzyme was reported to catalyze a conversion of cadmium acetate in aqueous solution into cadmium sulfide (CdS) nanocrystals such that they would generate a photoluminescence signal under UV illumination characteristic for crystal formation at quantum confined sizes[55]. Indeed, we could detect a photoluminescence signal from the BN-PAGE band corresponding to encapsulin loaded with SmCSE-EncSig after on-gel incubation with cadmium acetate and L-cysteine indicating that the smCSE-EncSig cargo was enzymatically active when bound into the shell (Supplementary Fig. 4d).

Size-constrained iron biomineralization. Another reason to choose encapsulins from *M. xanthus* was that it was previously reported to deposit iron via the ferritin-like cargo B and C into relatively large compartments (~32 nm, $T = 3$)[31]. We thus investigated whether this functionality could also be realized in eukaryotic cells to enable spatially confined iron deposition sequestered away from the complex signaling network controlling mammalian iron homeostasis. We thus generated a stable cell line co-expressing the nanoshell (A^{FLAG}) with all native cargo proteins (B,C,D) via a dual-promoter construct (Fig. 6a). In this cell line, we observed long-term and robust expression of all components shown by co-immunoprecipitation with A^{FLAG} and by immunocytochemistry against the external FLAG-epitope (Fig. 6b, left panel, Supplementary Fig. 5a). Transient co-expression of the ferrous iron transporter $MmZip14^{FLAG}$ (Zip14) in the stable cell line resulted in a robust dose-dependent iron loading (with ferrous ammonium sulfate (FAS) at concentrations between 0.25–1.25 mM) already after 48 h of supplementation as detected on BN-PAGE via

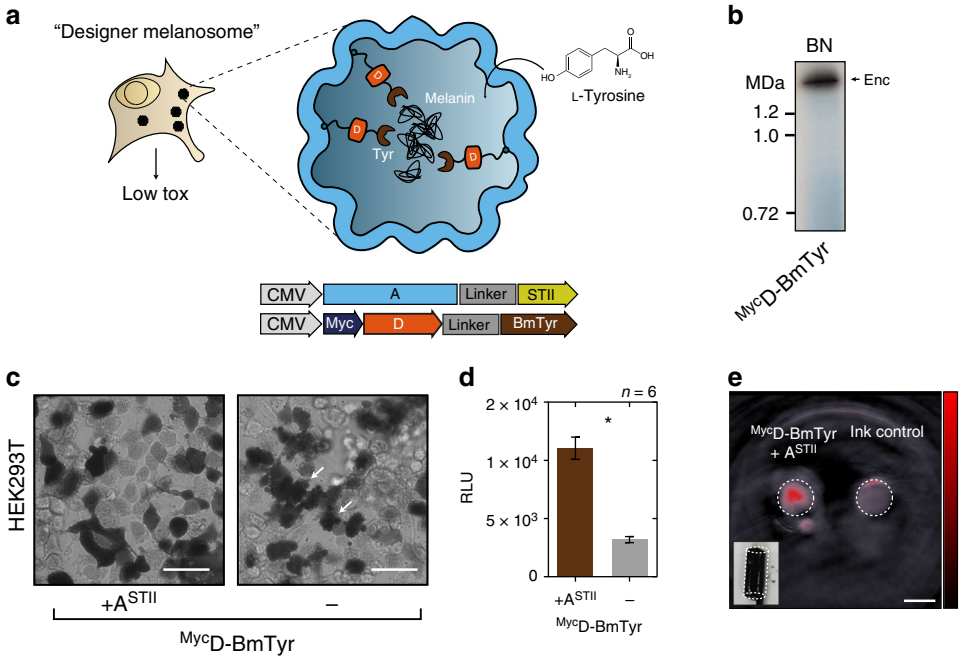

Fig. 5 Bioengineering of a melanosome by targeting melanin-generating tyrosinase to the encapsulin compartment. **a** Schematic of the detoxifying effects of compartmentalized melanin production by encapsulated tyrosinase from *Bacillus megaterium* targeted to the nanocompartment via fusion to the native cargo D. The substrate L-tyrosine enters the compartment via the pores in the nanoshell. **b** BN-PAGE showing on-gel production of melanin via tyrosinase expressed in HEK293T cells fused to Myc-tagged encapsulin-cargo D (^{Myc}D-BmTyr) to encapsulate it in the assembled nanoshell. Dark colorization of the band was observed after incubation with 2 mM L-tyrosine and 100 µM $CuCl_2$ in PBS (pH 7.4) for 1 h at 37 °C. **c** Bright-field images of HEK293T cells expressing ^{Myc}D-BmTyr with and without StrepTagII-modified shell (A^{STII}) after 48 h of expression. Twenty four hours post transfection, cells were supplemented with 1 mM L-tyrosine and 10 µM $CuCl_2$. Cell protrusions (white arrows) were apparent indicating toxic effects of overexpression of non-encapsulated tyrosinase. Scale bar: 20 µm. **d** Corresponding luciferase-based viability assay of HEK293T cells treated as in **c** overexpressing ^{Myc}D-BmTyr with or without A^{STII} after 48 h. (The bars represent the mean ± SEM, $n = 6$, $p < 0.0001$, unpaired *t*-test.) **e** Images of two tubular phantoms (transversal slice) obtained by multispectral optoacoustic tomography (MSOT). The phantoms were filled with ~10^7 cells in 1.5% low melting agar expressing ^{Myc}D-BmTyr with A^{STII} (supplementation as in **c** and **d**) or containing highly concentrated ink (OD = 0.2) as control showing the intense contrast obtained between 690 nm and 900 nm from the melanin-producing encapsulins. The coefficients obtained from linear unmixing of the optoacoustic spectra with a melanin reference spectrum are displayed on the red colormap overlaid on the image obtained at 720 nm. The lower left inset shows a color photograph of the tubular phantom containing the cells. Scale bar: 3 mm

DAB-enhanced Prussian Blue staining (DAB PB) (Fig. 6b, right panel).

Efficient iron loading could also be achieved by transient expression of A^{FLAG} + BCD_{P2A} together with Zip14. Under these conditions, iron supplementation with ~0–3 mM FAS for 48 h led to a substantial dose-dependent iron loading of the nanocompartment that saturated at ~1 mM FAS as shown by Coomassie and DAB-enhanced Prussian Blue BN PAGE (Fig. 6c, upper panel, Supplementary Fig. 5b). Interestingly, when we tested the cargo molecules individually for their ability to load iron into the nanosphere, we found that co-expression of only B or C generated equally intense DAB PB bands as compared to BCD_{P2A}, indicating that either B or C is sufficient for iron deposition inside the nanocompartment.

In contrast, co-expression of D with A^{FLAG} or any of the cargo molecules without the presence of A^{FLAG} did not lead to discernable DAB PB signals (Fig. 6c, lower panel, Supplementary Fig. 5c). In a standard cell viability assay, we found no impairment of the cells when Zip14 was co-expressed together with A^{FLAG} and BCD_{P2A} or just B. However, ~7% of cells showed reduced viability when the cargos BCD_{P2A} were expressed without the nanocompartment ($p = 0.0238$, Mann Whitney test, $n = 3$) or when only the fluorescent protein mEos4b-EncSig was expressed (Supplementary Fig. 5d) indicating that in the absence of the nancompartment the imported iron was not sufficiently sequestered by the endogenous iron homeostasis machinery.

We furthermore tested variants of A with N-terminal fusions with peptide sequences from *Magnetospirillum magneticum* Mms (6 and 7) proteins reported to aid in templating iron mineralization[56] but found no additional benefit of these modified inner surfaces over A^{FLAG} using our current readout (Supplementary Fig. 5e). In addition, we analyzed several variants of the cargo proteins B and C, fused C-terminally to peptides from Mms proteins (superscripts M6, M7, please see Supplementary Fig. 5f). These data confirmed that either B or C are sufficient to load the nanocompartment with iron and showed that no obvious additional iron loading resulted from the presence of the Mms peptides.

Encapsulins enable detection via MRI and magnetic sorting. Next, we were interested in whether the strong iron accumulation inside eukaryotically expressed encapsulin shells would yield significant contrast by MRI. We thus expressed A^{FLAG} alone or together with either all native cargos BCD_{P2A} or just ^{Myc}B, or ^{Myc}D and Zip14 and subjected cell pellets to relaxometry measurements by MRI. The nanocompartment A^{FLAG} co-expressed with all native cargo proteins (BCD) lead to a significant increase in R_2^*-relaxation rates as compared to just A^{FLAG}. The same effect was observed by co-expressing just the ferritin-like B (Fig. 7a, $p = 0.0047$, Kruskal–Wallis with significant differences at $\alpha = 0.05$ from Dunn's multiple comparisons test vs. A^{FLAG},

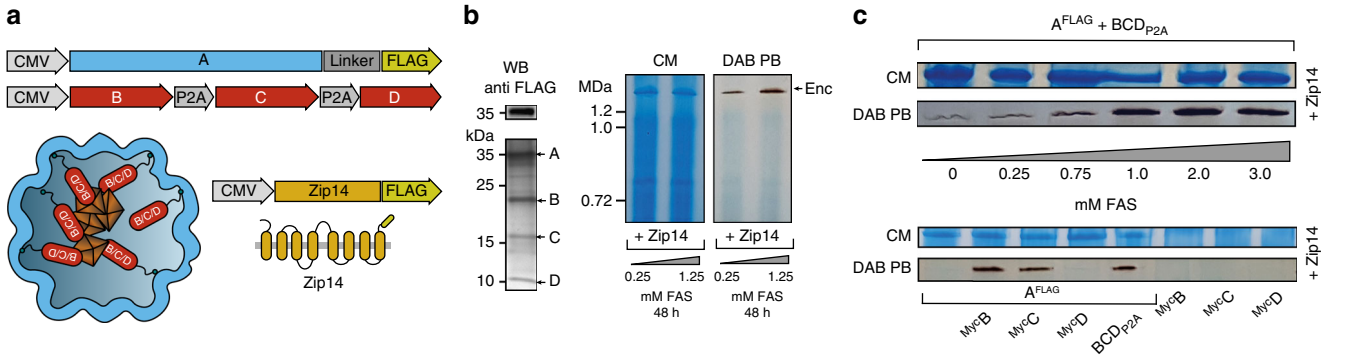

Fig. 6 Efficient iron loading of eukaryotically expressed encapsulin nanospheres **a** Schematic of a dual-promoter construct used for generation of a stable cell line expressing A^{FLAG} and all native cargos B, C, and D. Also depicted is a construct encoding the iron-transporter $MmZip14^{FLAG}$ (Zip14) used to transport additional amounts of iron into the cell. **b** Co-immunoprecipitation (Co-IP) against the FLAG epitope from a whole cell lysate of a stable HEK293T clone expressing A^{FLAG} together with B, C, and D analyzed by silver-stained SDS PAGE and the corresponding WB against the FLAG epitope (left panel). The pair of Blue Native (BN) gels visualizes proteins from whole cell lysates via Coomassie staining (CM) (left panel) and iron content via treatment with DAB enhanced Prussian Blue (DAB PB) (right panel) from the same stable cell line. Robust iron loading of the assembled nanocompartments was achieved by transient co-expression of $MmZip14^{FLAG}$-$_{IRES}$-ZsGreen1 in which case 0.25 mM ferrous ammonium sulfate (FAS) for 48 h was sufficient to see strong iron loading. **c** BN gel stained with CM or DAB PB loaded with whole cell lysates of HEK293T cells transiently expressing $A^{FLAG} + BCD_{P2A}$ and $Zip14^{FLAG}$ supplemented with different concentrations of FAS (0–3 mM) for 48 h (upper panel). The strong bands, which correspond to the assembled nanoshell, indicate high expression levels of encapsulins and efficient, dose-dependent iron loading. The lower panel shows a CM and DAB PB-stained BN gel from whole cell lysates of HEK293T cells expressing $Zip14^{FLAG}$ and different combinations of native cargo molecules: ^{Myc}B, ^{Myc}C, and ^{Myc}D alone, or all three (BCD_{P2A}) with or without A^{FLAG}. The robust DAB PB stains show that the ferritin-like cargo proteins B or C are sufficient for iron loading into encapsulins. FAS was supplemented at 2.5 mM for 48 h

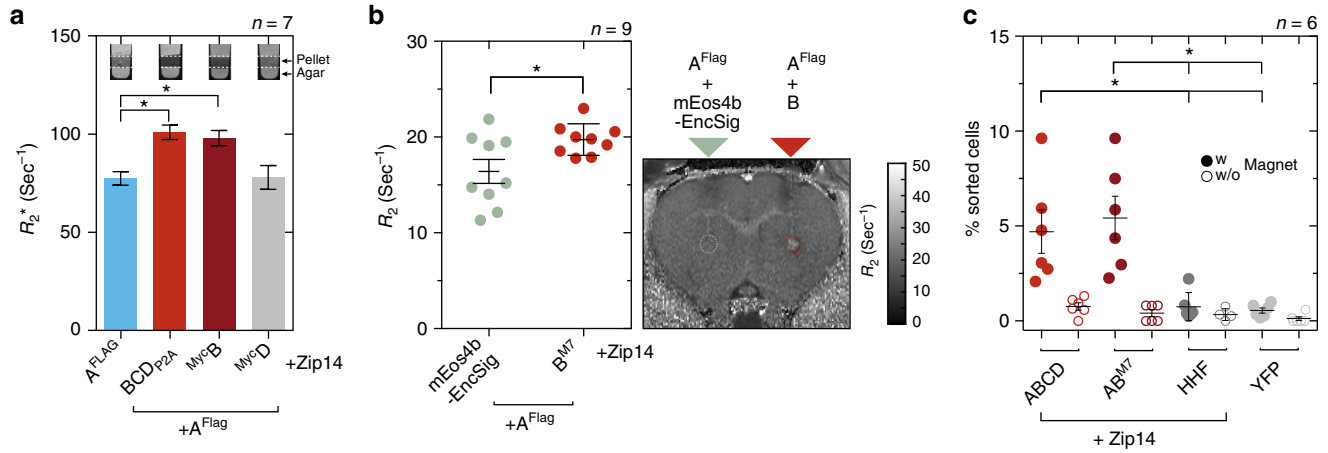

Fig. 7 Iron-filled encapsulins enable detection by MRI and magnetic cell separation. **a** Relaxometry measurements by MRI conducted on cell pellets (~10^7 cells) from HEK293T cells transiently expressing $A^{FLAG} + BCD_{P2A}$, ^{Myc}B, or ^{Myc}D, or A^{FLAG} alone (1 mM FAS for 24 h and expression of $Zip14^{FLAG}$). Expression of A^{FLAG} with BCD_{P2A} or with ^{Myc}B showed a significantly enhanced R_2^*-relaxation rate as compared with A^{FLAG} alone or loaded with ^{Myc}D; ferritin-like cargo B was sufficient to generate an increase in R_2^* in the presence of the A^{FLAG} nanocompartment ($p = 0.0047$, Kruskal–Wallis, $n = 7$ from four independent experiments, stars indicate significance at $\alpha = 0.05$ from Dunn's multiple comparisons test vs. A^{FLAG}; the bars represent the mean ± SEM). The insets show MRI slices (13.5 ms echo time) through test tubes in which cells were pelleted on a layer of agar. **b** In vivo MRI detection of HEK293T cells transiently co-expressing A^{FLAG} together with ferritin-like B^{M7} that were xenografted into rat brains. As compared to cells co-expressing A^{FLAG} together with the fluorescent protein mEos4b-EncSig as control cargo, we observed significantly increased transverse relaxation rates ($p = 0.0078$, Wilcoxon matched-pairs signed rank test, $n = 9$) measured at the injection site for $A^{FLAG} + B^{M7}$ expressing cells 24 h post injection. The horizontal lines represent the mean ± SEM. The image on the right shows a coronal R_2 map through a rat brain with the regions of interest (ROIs) defined over the injection sites by dashed circles. **c** HEK293T cells were co-expressing A^{FLAG} and BCD_{P2A}, A^{FLAG} and B^{M7}, or human H-chain ferritin (HHF) as a control together with Zip14 and were treated with 2.5 mM FAS for 48 h. Additional control cells were expressing only EYFP. Independent cell suspensions were subsequently sorted on commercial magnetic separation columns inside and outside the magnetic field to control for unspecific retention in the mesh of the column. The fraction of cells separated in the magnetic field for both encapsulin:cargo conditions was significantly higher than for any of the control conditions HHF + Zip14 or YFP ($p = 0.0007$, Kruskal–Wallis, $n = 6$ from three independent experiments, stars indicate significance at $\alpha = 0.05$ from Dunn's multiple comparisons test across all conditions with magnetic field; the horizontal lines represent the mean ± SEM)

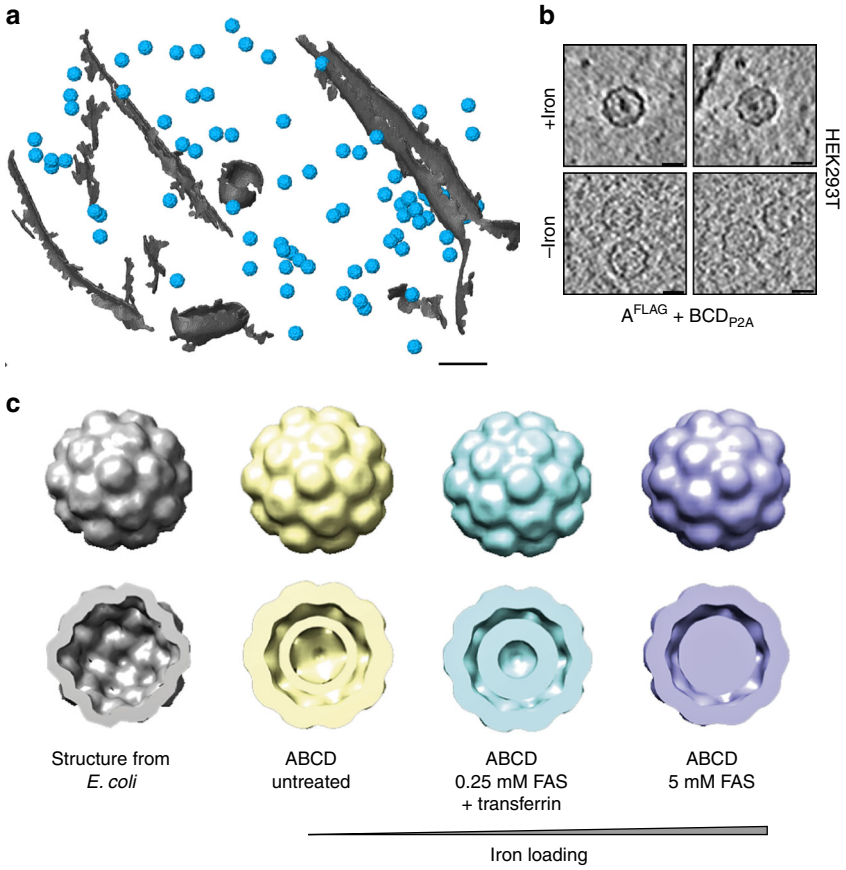

Fig. 8 Encapsulins as genetically encoded markers for cryo-electron tomography (Cryo-ET). **a** Cryo-ET data from HEK293T cells stably expressing encapsulins together with native ferritin-like cargo proteins (using the dual promoter construct A^{FLAG};BCD^{P2A} shown in Fig. 6a). 3D rendering showing encapsulins in blue and membranes in gray colors. Scale bar:100 nm. **b** Example slices from tomograms show encapsulins with and without electron-dense cores from iron-accumulation (treatment with 5 mM FAS for 48 h prior to vitrification). Scale bars:20 nm. **c** In situ structures (displayed as 2× binned) derived from cryoelectron tomography of nanocompartments assembled in HEK293T cells without (beige), with 0.25 mM FAS and 1 mg/ml human transferrin (cyan) and 5 mM FAS (purple) as compared with the published structure shown in gray (pdb 4PT2; EMDataBank EMD-5917) that was obtained from *M. xanthus EncA* expressed in *E. coli*[31]. The cutaway views of the encapsulins show electron densities indicating the presence of cargo proteins (beige) and additional iron deposition (cyan and purple) as compared to published data from the *EncA* shell[31] that were obtained in the absence of cargo proteins

$n = 7$). This indicated again that co-expression of B was sufficient to generate efficient iron deposition inside the nanoshell.

We subsequently sought to test whether cells genetically labeled with encapsulins could be detected by MRI in vivo. As an initial assessment, we thus xenografted cells co-expressing A^{FLAG} together with B^{M7} into rat brains and obtained R_2-relaxation maps that showed elevated relaxation rates ($p = 0.0078$, Wilcoxon matched-pairs signed rank test, $n = 9$) at the injection site as compared to xenografted cells in which the fluorescent protein mEos4b-EncSig was used as a control cargo (Fig. 7b).

In addition to MRI contrast, the iron biomineralization inside the encapsulins also allowed us to magnetically sort cells co-expressing the shell A^{FLAG} with BCD_{P2A} or with B^{M7} at significantly higher percentages than when human H-chain ferritin (HHF) was expressed or just yellow fluorescent protein (EYFP) ($p = 0.0007$, Kruskal–Wallis, with significant differences at $\alpha = 0.05$ from Dunn's multiple comparisons test, $n = 6$; Fig. 7c).

Encapsulins as markers for electron microscopy. Given that the iron loading of the encapsulins was very efficient and observable at the population level, we next assessed how well individual nanocompartments could be detected by electron microscopy in cells such that they could be used as genetically encoded markers. We thus grew HEK293T cells stably expressing the shell protein A^{FLAG} and BCD_{P2A} using a dual promoter vector on a transmission electron microscopy (TEM) grid, vitrified them by plunge-freezing and produced lamellae by cryo-focused ion beam (cryo-FIB) milling for in situ cellular cryo-electron tomography (cryo-ET). The heterologously expressed encapsulins were readily detected as clearly discernible nanospheres (Fig. 8a, Supplementary Fig. 6a, b) that exhibited electron-dense cores when we supplemented the growth media with ferrous iron (Fig. 8b) and were distributed as monodisperse spheres throughout the cytosol (Supplementary Fig. 6c, d). The electron density maps showed a high similarity to the structure published from encapsulin shells from *M. xanthus* expressed in *E. coli* (pdb 4PT2; EMDataBank EMD-591728, Fig. 8c). The clipped views from the encapsulins (blue) furthermore show electron densities associated with docked cargo proteins and most likely biomineralized iron as compared with the inner surface of the shell from *E. coli* (gray) that was mapped in the absence of any cargo (Fig. 8c, lower row). These data demonstrate that the spherical shape and high, non-toxic expression levels make encapsulin very attractive as fully genetically expressed markers for EM.

Discussion

In summary, we genetically controlled multifunctional orthogonal compartments in mammalian cells via expressing N- or

C-terminally modified encapsulins, which we found to auto-assemble into abundant nanocompartments which readily encapsulated sets of natural and engineered cargo proteins and enabled size-constrained metal biomineralization.

The efficiency of self-targeting and auto-packaging of the various cargo proteins in mammalian cells was remarkable given that the number of possible protein interactions is even a few-fold higher than in the original prokaryotic host organism[57,58]. We found that about 60 cargo proteins of a canonical fluorescent protein can be bound to the inner encapsulin surface via the minimal encapsulation signal. Higher loading factors could be achieved by providing cargo proteins with multidentate adapters such that the entire encapsulin volume could be filled. We furthermore observed that without co-expression of endogenous or engineered cargo, the abundance of the 60-mer encapsulin shell with $T = 1$ symmetry was increased, which is in line with a previous observation made from *M. xanthus* encapsulin expressed in *E. coli*[31] and suggests that encapsulation of cargo leads to the preferred assembly of the 180-mer in $T = 3$ symmetry.

Also, iron storage inside the capsule via the ferritin-like enzymes B or C targeted to the encapsulins was very efficient, indicating that there was sufficient access to ferrous iron. Whereas encapsulins heterologously expressed in *E. coli* were shown to load iron[59], this could so far not been shown in mammalian cells. We also found that just co-expression of B (or C) with A is sufficient for robust iron storage such that a single-piece reporter construct of just ~2.1 kb in size can be used.

In the context of optimizing T_2 contrast in MRI, it would certainly be valuable to explore modifications of the outer surface that may control the agglomeration state and thus could modulate the apparent relaxivity of encapsulin ensembles[60]. In this context, it would also be desirable to explore capsid architectures with more storage capacity such as ones with $T = 7$ quasisymmetry known from bacteriophage HK97[31,61]. Furthermore, modifications of the inner surface of the shell may be engineered and/or additional cargo could be designed that could facilitate the nucleation process to support higher iron packing densities or alter environmental parameters (e.g., pH and redox potential) to potentially even generate superparamagnetic iron-oxides which possess a substantially larger magnetization[62]. Iterative optimization schemes such as directed evolution could also be employed based on rescue assays from excess iron or magnetic microfluidic sorting and could also be complemented by parallel screens in prokaryotes if enough iron-influx can be achieved there.

Their dense monodisperse distribution, spherical shape, and sufficient size, also render encapsulins excellent genetically expressed EM markers in mammalian cells (Supplementary Movie 1) that are much more readily detectable than ferritins, which have been visualized by EM in *E. coli* and yeast[63,64]. In addition, the iron-based contrast in encapsulins has the advantage over semi-genetic methods such as metallothionein (MT), miniSOG, erHRP, or APEX/APEX2 that no fixation and delivery of artificial substrates and precipitation of electron-dense material is necessary which may alter cellular structures[53,65–68]. Instead, if iron-based EM contrast is desired, cells expressing the iron-accumulating encapsulins can just be grown in regular growth media containing sufficient iron for transferrin-mediated uptake before direct plunge freezing and cryo-EM.

For future applications as EM gene reporters in, e.g., connectomics research, it would be desirable to generate further encapsulin variants with surface-presented targeting moieties to control their subcellular localization. In this regard, it is of note that virtue of the self-assembling mechanism, the size of A is only 0.9 kb and that of B just 0.5 kb such that a combined construct is small enough to be carried by viruses optimized for trans-synaptic tracing[69]. It should furthermore be feasible to perform selective detection of encapsulins loaded with split photoactivatable fluorescent proteins via photoactivated localization microscopy (PALM) and combine this with cryo-ET as was demonstrated for photoactivatable GFP (cryo-PALM)[70].

Besides allowing the influx of metals for size-constrained biomineralization for the type of applications discussed above, the pore size of ~5 Å inside the encapsulin shell also affords selective passage of small substrates, whereas reaction products may be trapped inside the nanoshell. We have exploited this feature by encapsulating tyrosinase for confined enzymatic production of the toxic polymer melanin and utilized the engineered "nanomelanosomes" as genetically encoded reporters for optoacoustic imaging.

In future applications, encapsulins could thus be used as versatile reaction chambers for, e.g., metabolic engineering of orthogonal reactions in eukaryotic cells. The toolbox for genetically controlled compartmentalization in mammalian cells which we introduce here could, for instance, enable multi-step enzymatic production involving labile or toxic intermediates but yielding end-products that may have beneficial intracellular effects or serve as molecular signals upon "quantal" release from the nanocompartment. The approach could for instance also endow genetically modified mammalian cells used for cell therapies with metabolic pathways that may augment their therapeutic efficacy. Complementarily, endogenously produced toxic products could be contained and detoxified in engineered compartments for causal studies or potentially for cell or gene therapies.

In addition to the encapsulins presented here, heterologous expression of compartments with different sizes and shapes seem possible, which could offer different sets of endogenous and engineered cargo molecules with different subcellular targeting. These alternative systems would ideally also be orthogonal to each other such that multiplexing (maybe even nesting) of several engineered compartments and multicomponent processes could be achieved.

More generally, genetically controlled compartmentalization of multi-component processes in eukaryotic cells—as demonstrated for encapsulins here—is a fundamental biotechnological capability that has profound implications for mammalian cell engineering and emerging cell therapies.

Methods

Genetic constructs. Mammalian codon-optimized MxEncA (UniProt: MXAN_3556) MxEncB, MxEncC, and MxEncD (UniProt: MXAN_3557, MXAN_4464, MXAN_2410) were custom synthesized by Integrated DNA Technologies and cloned into pcDNA 3.1 (+) Zeocin (Invitrogen) using restriction cloning or Gibson assembly. The MxEncA surface tags (FLAG or StrepTagII) were C-terminally appended using Q5® Site-Directed Mutagenesis (New England Biolabs). N-terminal Myc epitopes were added accordingly to the cargo proteins. Multigene expression of B, C, and D was achieved by generating a single reading frame containing all three genes separated by P2A peptides yielding BCD_{P2A}. A "scarless" bicistronic construct encoding ^{Myc}C and A^{STII} was custom synthesized by inserting a *Ssp* DnaE mini-intein variant engineered for hyper-N-terminal autocleavage followed by a P2A peptide in between the genes as previously described[41]. For generating stable clones expressing MxEncABCD, $MxEncA^{FLAG}$ was cloned into the Cytomegalovirus promoter (CMV) driven expression cassette of pBudCE4.1 (Invitrogen) and BCD_{P2A} was cloned into the elongation factor 1 alpha promoter (EF1a) driven expression cassette of the vector via restriction cloning. To generate AAV enabling multigene expression of $MxEncA^{FLAG}$ and MxB-Mms7ct, two strategies were employed: $MxEncA^{FLAG}$ was cloned upstream of an ECMV internal ribosome entry site (IRES) whereas MxB-Mms7ct was inserted downstream. The second approach employs MxB-Mms7ct followed by a P2A peptide and $MxEncA^{FLAG}$. The two cassettes were subcloned into pAAV-CamKIIa (https://www.addgene.org/26969/) with BamHI and EcoRI. AAVs were custom prepared by the UNC Vector Core of the University of North Carolina at Chapel Hill. To test the bicistronic expression constructs used for the AAVs in HEK293T cells, the cassettes were also sub-cloned into the pcDNA 3.1 (+) Zeocin with EcoRI and NotI. To target PAmCherry1 and mEos4b as cargo to the encapsulin nanocompartments, the fluorescent proteins were C-terminally fused to 2 × GGGGS linkers followed by the minimal encapsulation signal LTVGSLRR

(EncSig). To generate the destabilized version of mEos4b, the L106P mutant of FKBP12 (DD-N)[43] was N-terminally appended to mEos4b-EncSig using Gibson-Assembly yielding DD-mEos4b-EncSig. For complementation of split PAmCherry1 inside the encapsulin nanoshell, amino acids 1–159 of PAmCherry1 were fused to MxEncC via a 2 × GGGGS linker and amino acids 160–236 of PAmCherry1 were directly fused to the C-terminus of MxEncB. For complementation of a split luciferase, the split part LgBit (NanoBiT system, Promega) was fused C-terminally to MxEncC via a 2 × GGGGS linker. SmBit was directly fused to the C-terminus of MxEncB. SmCSE[55] (UniProt: Smal_0489) and APEX2[53] were fused to 2 × GGGGS linker followed by the minimal encapsulation signal. Mammalian codon-optimized *Bacillus megaterium* tyrosinase (BmTyr) was C-terminally appended to ^{Myc}D separated by 2 × GGGGS linker in custom gene synthesis. C-terminally FLAG-tagged *Mus musculus* Zip14 was inserted into pcDNA 3.1 (+) or pIRES2-ZsGreen1 via restriction cloning. To yield secreted encapsulins, MxEncA^{STII} was N-terminally fused to a human BM40 secretion peptide. In order to generate encapsulin derivatives featuring C-terminal acidic peptides of magnetotactic bacteria Mms proteins that are implicated in mediation of magnetite formation either the C-terminal peptide of Mms6 (YAYMKSRDIESAQSDEEVELRDALA) or Mms7 (YVWARRRHGTPDLSDDALLAAAGEE) of *Magnetospirillum magneticum* were fused either to the inward-facing N-terminus of MxEncA^{FLAG} or to the C-terminus of either the MxEncB or C using Q5® Site-Directed Mutagenesis. For a complete list of the genetic constructs featuring their composition refer to Supplementary Table 1.

Cell culture. Low passage number HEK293T (ECACC: 12022001, obtained via Sigma-Aldrich) and CHO (ECACC: 85050302, obtained via Sigma-Aldrich) cells were cultured in advanced DMEM with 10 % FBS and penicillin–streptomycin at 100 µg/ml at 37 °C and 5% CO_2. Cells were transfected with X-tremeGENE HP (Roche) according to the protocol of the manufacturer. DNA amounts (ratio shell to cargos) were kept constant in all transient experiments to yield reproducible DNA-Lipoplex formation. To generate a stable HEK293T cell line expressing MxEncABCD, cells were transfected with pBudCE4.1 MxEncABCD and stable transfectants were selected with 300 µg/ml Zeocin (InvivoGen).

Protein expression and lysis. Cells were harvested between 24 and 48 h post transfection. Cells were lysed with M-PER Mammalian Protein Extraction Reagent (Pierce Biotechnology) containing a mammalian protease inhibitor cocktail (SIGMA P8340, Sigma-Aldrich) according to the protocol of the manufacturer in all experiments using FLAG-tagged encapsulins. For lysis of cells expressing StrepTagII-modified encapsulins, cells were resuspended in Buffer W (150 mM NaCl, 100 mM Tris-Cl, pH 8.0) and exposed to four freeze–thaw cycles in LN_2. After spinning down cell debris at 10,000 × *g* for 15 min, cell lysates were kept at 4 °C for downstream analyses. Protein concentrations of lysates were determined by measuring OD at 280 nm.

Co-immunoprecipitation of encapsulins. Cell lysates were incubated with Anti-FLAG® M2 Magnetic Beads or Anti-FLAG® M2 affinity gel (SIGMA M8823 and A2220, Sigma-Aldrich) according to the protocol of the manufacturer. After binding, the magnetic beads were washed four times on a magnetic separator rack (DYNAL separator, Invitrogen) with M-PER buffer. Bound FLAG-tagged encapsulins were eluted using M-PER buffer containing 100 µg/ml FLAG-peptide (SIGMA F3290, Sigma-Aldrich). In the case of encapsulins with an external StrepTagII, MagStrep "type3" XT beads or Strep-Tactin®XT resin (IBA Lifesciences) was used according to the protocol of the manufacturer. Proteins were eluted using Buffer BXT (150 mM NaCl, 100 mM Tris-Cl, pH 8.0, 50 mM Biotin). To analyze the eluted proteins, samples were mixed with SDS-PAGE sample buffer and incubated at 95 °C for 5 min. Samples were loaded onto pre-cast 12% Bio-Rad Mini-PROTEAN® TGX™ (Bio-Rad Laboratories) gels and run for 45 min at 200 V. Accordingly, gels were either directly silver-stained using SilverQuest™ Silver Staining Kit (Novex) according to the protocol of the manufacturer or immunoblotted onto PVDF membranes. After blotting, membranes were blocked in 5% non-fat milk in TBS for 1 h at room temperature. Subsequently, membranes were incubated in TBS containing 5% non-fat milk and 1 µg/ml Monoclonal ANTI-FLAG® M2 antibody (SIGMA F1804, Sigma-Aldrich) or 1 µg/ml Anti-Myc Tag Antibody clone 9E10 (05–419, EMD Millipore) for 2 h at room temperature. After five washing cycles with TBS, membranes were incubated with anti-mouse IgG HRP-conjugate (SIGMA A5278, Sigma-Aldrich) for 1 h at room temperature in 5% non-fat milk in TBS. Protein bands were detected using Amersham ECL Prime Western Blotting Detection Reagent (GE Healthcare Bio-Sciences AB) on a Fusion FX7/SL advance imaging system (Peqlab Biotechnologie GmbH). For dephosphorylation of protein material from the Co-IP, 10 units of calf intestinal phosphatase (New England Biolabs) were added to protein solutions in 1× CutSmart Buffer (New England Biolabs) and incubated for 1 h at 37 °C. For densitometric determination of SDS-PAGE bands, band intensity integrals were measured using ImageJ (NIH).

Blue Native gel electrophoresis and on-gel analyses. For detection of native encapsulin nanocompartments, the NativePAGE™ Novex® Bis-Tris Gel System (Life Technologies) was used. Either eluted material from the Co-IP/purification or whole cell lysates of cells expressing encapsulins in NativePAGE™ Novex® sample buffer were loaded onto pre-cast NativePAGE™ Novex® 3–12% Bis-Tris gels. NativeMark™ Unstained Protein Standard (Life Technologies) covering a size range between 20 and 1200 kDa was used as a marker. The total protein amount of whole cell lysates loaded per well was adjusted to ~1–3 µg. Blue native (BN) gels were run for 90–180 min at 150 V according to the protocol of the manufacturer. Gels loaded with samples from Co-IP/purification were silver-stained using SilverQuest™ Silver Staining Kit (Novex) or Coomassie-stained using Bio-Safe™ Coomassie Stain (Bio-Rad Laboratories). For protein detection, gels loaded with whole cell lysate samples were Coomassie-stained accordingly. For detection of iron-containing proteins, gels loaded with samples containing iron loaded encapsulins were Prussian Blue (PB) stained. Briefly, gels were incubated in 2% potassium hexacyanoferrate(II) in 10% HCl for 45 min. For 3,3′-diaminobenzidine-enhancement (DAB PB), gels were washed three times with ddH_2O and incubated in 0.1 M phosphate buffer (pH 7.4) containing 0.025% DAB and 0.005% H_2O_2 until dark-brown bands appeared. To stop DAB polymerization, gels were washed three times with ddH_2O. For detection of fluorescent signals from native encapsulin bands (fluorescent cargos: mEos4b, PAmCherry1, split PAmCherry1 or mineralized CdS), unstained BN gels were imaged on a Fusion FX7/SL advance imaging system (Peqlab Biotechnologie GmbH) using the UV fluorescence mode. For on-gel detection of luminescence signal generated by encapsulated split NanoLuciferase, unstained BN gels were soaked in 1 ml of Nano-Glo® Luciferase substrate (Nano-Glo® Luciferase Assay, Promega) and imaged on a Fusion FX7/SL advance imaging system (Peqlab Biotechnologie GmbH) in chemiluminescence mode. For whole cell lysate luminescence detection, cell lysates were mixed with the substrate at a 1:1 ratio and luminescence readings were taken on a Centro LB 960 (Berthold Technologies) at 0.1 s acquisition time. For detection of APEX2 peroxidase activity inside encapsulins, unstained BN gels were incubated in 0.1 M phosphate buffer (pH 7.4) containing 0.025% DAB and 0.005% H_2O_2 for 15 min until black bands appeared on the gel. For microscopic detection of DAB polymerization in cells expressing APEX2-loaded encapsulins, cells were fixed in 4% PFA in PBS for 15 min. Subsequently, cells were incubated in 0.1 M phosphate buffer (pH 7.4) containing 0.025% DAB and 0.005% H_2O_2 for 5 min. The reaction was stopped by washing three times with PBS. For the on-gel detection of melanin generation associated with encapsulins, gels loaded with whole cell lysates of HEK293T cells expressing encapsulins loaded with tyrosinase were incubated in PBS containing 2 mM L-tyrosinase and 100 µM $CuCl_2$ for 1 h at 37 °C until a black encapsulin band became visible.

Size exclusion chromatography. Size exclusion chromatography (SEC) of purified A^{FLAG} with or without DD-mEos4b-EncSig was performed on an Äkta Purifier (GE Healthcare) equipped with an analytical size exclusion column (Superose 6 10/300 GL, GE Healthcare) at 4 °C. For refractive index (RI) detection, a Viscotek TDA 305 triple array detector (Malvern Instruments) downstream of the column was used. In total, 100 µl samples were run at a flow rate of 0.4 ml/min in 50 mM Tris-HCl, 150 mM NaCl, 1 mM EDTA, pH 7.4, at a concentration of 0.3 mg/ml.

Dynamic light scattering. Dynamic light scattering experiments were performed on a DynaPro NanoStar instrument and analyzed with DYNAMICS 7.1.9 software (Wyatt Technology). Measurements were performed at 22 °C using standard rectangular cuvettes containing 60 µl of protein sample in the concentration range between 0.15 and 0.5 mg/ml. For each measurement, 100 acquisitions with an acquisition time of 5 s were recorded.

Native mass spectrometry. Purified sample material from HEK293T cells expressing A^{FLAG}, with and without co-expression of the photoactivatable fluorescent protein DD-mEos4b-EncSig, was buffer exchanged to 150 mM aqueous ammonium acetate, pH 7.5 using Micro Bio-Spin Columns with Bio-Gel P6 (Biorad, USA) following the manufacturer's protocol for buffer exchange. Samples were analyzed at a concentration of 0.1–0.45 g/l, corresponding to an estimated monomer concentration ranging from 3 to 14 µM. Gold-coated nanoelectrospray needles were made in-house from borosilicate capillaries (Kwik-Fil, World Precision Instruments, Sarasota, FL) on a P97 puller (Sutter Instruments, Novato, CA) and being coated by using an Edwards Scancoat six pirani 501 sputter coater (Edwards Laboratories, Milpitas, USA). Measurements were carried out in positive ion mode on a modified Q-ToF 2 (Waters, UK) instrument[71,72], operated at elevated pressure in the source region (~10 mbar), using Xenon as collision gas at $2*10^{-2}$ mbar in the collision cell. Capillary and sample cone voltage was set to 1400 V and 150 V, respectively. The voltage before the collision cell was either set to 100 V or 250–300 V, optimizing for desolvation of the intact complex or the subsequent ejection of subunits, respectively. Spectra were calibrated using an aqueous solution of cesium iodide (25 mg/ml) and exported from MassLynx. All further data analysis was performed with in-house developed python scripts (Python 3.6). When applicable, charges were assigned to charge state resolved peak series by extracting the top position for consecutive charge states and minimizing the standard deviation (SD) of the average mass by trying different charge states. Centroids for empty and cargo filled encapsulins ($T = 3$) were calculated using all data points above 40 % of the base peaks intensity in the appropriate region (*m/z* 30,000–40,000 for empty and *m/z* 35,000–45,000 for cargo filled encapsulins). The average was taken over three technical replicates and the error represents the

standard deviation (SD). To estimate the mass from the m/z position, we fitted 77 empirical determined masses and their corresponding m/z positions to the equation $\mathrm{Mass[kDa]} = A^{*}m/z^{B}$. These 77 proteins consist of encapsulin $T = 1$, which mass was determined in this study as well as 76 other assemblies, which were already measured and reported in previous publications[73,74]. The resulting formula $\mathrm{Mass[kDa]} = 1.63{*}10^{-6}{*}m/z^{2.14}$ was used to calculate the mass from the average m/z positions of empty and cargo filled encapsulins ($T = 3$). Since mass and m/z positions do not follow a linear relation, we averaged the upper and lower error from the m/z dimension projected in the mass domain. Cargo load was estimated based on the difference between the predicted masses of empty and cargo loaded encapsulins ($T = 3$). The error of the mass difference was calculated using the equation $\sigma\Delta\mathrm{Mass} = (\sigma\mathrm{Mass1}^2 + \sigma\mathrm{Mass2}^2)^{1/2}$. The difference in mass was then divided by 41.4 kDa, the mass of the DD-mEos4b-EncSig monomer protein. The A^{FLAG} monomer mass was calculated as the weighted average for the different proteoforms, using the summed intensities over the charge states for each species.

Complementation of split PAmCherry1 inside encapsulins. Cells transfected with C-PAs1 and B-PAs2 with or without A^{FLAG} were seeded onto 8-well Poly-L-lysine-coated microscopy chips (Ibidi). Thirty-six hours post transfection, live cell confocal microscopy was conducted on a Leica SP5 system (Leica Microsystems). For photoactivation of split PAmCherry1, samples were illuminated with a 405 nm laser for 60 s at 40% laser power. The signal of complemented split PAmCherry1 was excited using the 561 nm laser. To quantify the complementation of split PAmCherry 1 with or without the encapsulin shell, the ratio of the total mean fluorescence after photoactivation divided by the signal before was calculated. ImageJ was used to quantify mean fluorescence values from randomly chosen areas on the well.

Multispectral optoacoustic tomography. Optoacoustic images of cells co-expressing A^{STII} and ^{Myc}D-BmTyr were acquired on an inVision 256-TF system (iThera Medical GmbH). Briefly, ~10^7 HEK293T cells co-expressing the genes treated with 10 µM $CuCl_2$ and 1 mM L-tyrosine 24 h prior to the measurement were detached using trypsin, washed with PBS, embedded into 1 % low melting agar yielding a tubular phantom of ~ 300 µl volume. The cell phantom and an ink phantom (OD = 0.2) were placed in a custom-built sample holder and optoacoustic images were acquired for the range of wavelengths between 690 and 900 nm. Signals were reconstructed using ViewMSOT software suite (iThera Medical GmbH) and linearly unmixed using a reference spectrum for melanin.

Magnetic sorting. Cells were washed twice with PBS, detached with Accutase® (Sigma-Aldrich) and resuspended in DPBS supplemented with 10% fetal bovine serum (Gibco) prior to sorting. For magnetic sorting, columns filled with ferromagnetic spheres (MS columns, Miltenyi Biotec) were placed in an external magnetic field (OctoMACS separator, Miltenyi Biotec) and equilibrated with 1 ml DPBS containing 10% FBS. The column was loaded with cells and washed with 0.5 ml DPBS; the flow-through was collected as one fraction. After removing the column from the magnetic separator, cells were eluted with 1 ml DPBS. The total number of cells before sorting as well as the cell numbers in flow-through and eluate were determined with a Countess II FL Automated Cell Counter (Life Technologies).

Magnetic resonance imaging of cells. MR images were acquired at a Bruker BioSpec 94/20USR, 9.4T system equipped with a RF RES 400 1H 112/072 Quad TR AD resonator. For $T_2{}^{*}$ measurements of cell pellets, $4{*}10^6$ HEK293T cells were seeded 24 h prior to transfection on poly-L-lysine-coated 10 cm cell culture dishes. Twenty four hours post transfection, ferrous ammonium sulfate (FAS) was added to the medium yielding a concentration of 1 mM. Twenty four hours post iron addition, cells were washed three times with DPBS and detached with Accutase® and centrifuged at 500 × g for 4 min. The pellets were resuspended in 800 µl DPBS and transferred to cryobank vials (Thermo Scientific Nunc) containing 50 µl of solidified 1% agarose at the bottom. Cells were then spun down at 2000 × g for 2 min and immediately used for MRI. $T_2{}^{*}$ measurements were conducted in a custom-made holder filled with DPBS to avoid susceptibility artifacts. $T_2{}^{*}$ values were calculated based on a multiple gradient echo (MGE) sequence with a TR of 800 ms, 12 echoes with an echo spacing of 4.5 ms (3.5–58.5 ms), a flip angle of 50°, field of view of 65 × 65 mm and a matrix size of 256 × 256. Relaxation rates were calculated with the *Image Sequence Analysis Tool* from Bruker BioSpin MRI GmbH.

In vivo expression of encapsulins in murine brains. Mice were positioned in a stereotaxic frame, anesthetized with isoflurane, and implanted bilaterally with MRI compatible guide cannulae (Plastics One) that were stably fixated with dental cement. Injection cannulae (Plastics One) were connected via polyethylene tubing (PE-50), filled with silicone oil, connected to a PhD 2000 syringe pump (Harvard Apparatus) and backfilled with solutions containing AAV viral particles. Injection cannulae were inserted into the guide cannulae and lowered into the brain. A volume of 1 µl of viral particles was injected at 0.1 µl/min. Injection cannulae were subsequently retracted slowly and replaced with dummy cannulae (Plastics One) that screwed firmly into the guide cannula pedestals. All experiments on mice were conducted in accordance with the guidelines approved by the government of Upper Bavaria.

Immunohistochemistry. Three to six weeks after intracranial viral injection, mice were terminally anesthetized, perfused, and the brains were removed for cryosectioning. Brain slices were then blocked in SuperBlock (TBS) Blocking Buffer (Thermo Fisher Scientific) for 1 h at room temperature in a humidified chamber. Subsequently, brain slices were incubated in 5 µg/ml Monoclonal ANTI-FLAG® M2 antibody (SIGMA F1804, Sigma-Aldrich) in TBS for 2 h at room temperature. After 5 × 5 min washes with TBS, the brain slices were incubated in 1 µg/ml Goat anti-Mouse IgG (H + L) Cross-Adsorbed Secondary Antibody conjugated to Alexa Fluor 488 (A-11001, Invitrogen) in TBS for 1 h at room temperature in darkness. For nuclear counterstaining, DAPI was added at 300 nM for 5 min. Finally, the brains slices were washed five times with TBS. Brain slices were subsequently imaged on an EVOS FL Auto Cell Imaging System (Invitrogen) or a Leica SP 5 confocal microscope (Leica Microsystems).

In vivo MRI. HEK293T cells (~$4{*}10^6$) were seeded onto poly-L-lysine-coated 10 cm cell culture dishes. Twenty four hours after seeding, cells were transiently transfected at 70–80% confluency with DNA constructs encoding either $A^{FLAG} + B^{M7}$ or A^{FLAG} + mEos4b-EncSig, as well as for both conditions Zip14 at 5% of the total DNA amount using X-tremeGENE™ (Roche). Twenty four hours post transfection, the cell culture medium was replenished with fresh medium containing 1 mM FAS. Twenty four hours after incubation with FAS, cells were washed gently three times with PBS, detached from the culture dishes after 5 min of treatment with a 1:1 solution of Accutase® (Sigma) and Trypsin, centrifuged for 5 min at 1200 × g and resuspended in growth media. Cell suspensions were backfilled into two injection cannulae (28 Gauge, Plastics One, Roanoke, VA, USA) connected via plastic tubing to 25 µl Hamilton glass syringes clamped in a remote dual syringe pump (PHD 22/2,000; Harvard Apparatus, Holliston, MA, USA). Injection cannulae (the side of injection for $A^{FLAG} + B^{M7}$ or control were switched between experiments) were then lowered into bilateral guide cannulae (22 Gauge, Plastics One, Roanoke, VA) that were previously implanted in Sprague–Dawley rats[75]. Rats were then centered in the bore of a 7T 20 cm inner diameter, horizontal bore magnet (Bruker BioSpin MRI GmbH, Ettlingen, Germany) and gradient echo scans (FOV = 2.5 cm × 2.5 cm, matrix size = 256 × 256; seven slices with 1 mm slice thickness) were taken at a TR = 800 ms and different echo times (5, 10, 15, 20, 25 ms) to compute relaxation rate maps and perform ROI analysis (circular ROIs of 1 mm diameter placed on injection sites) using custom routines in Matlab (Mathworks, Natick, MA, USA). All procedures on rats were conducted in accordance with National Institutes of Health guidelines and with the approval of the MIT Committee on Animal Care.

Cell viability assays. Iron-related cytotoxicity was monitored via the Roche Cytotoxicity Detection Kit (LDH) (Roche Diagnostics) according to the protocol of the manufacturer. Briefly, $7.5{*}10^5$ HEK293T cells were seeded on poly-L-lysine-coated 24-well plates. Twenty four hours post seeding, cells were transfected with different combinations of genes using X-tremeGENE HP (Roche). The Zip14 DNA amount was kept constant in all samples expressing Zip14 (5% of total DNA). For expression of combinations of A^{FLAG} with cargo proteins, 60% of the total DNA amount was encoding A^{FLAG} and the remaining 35% were used for the respective cargo molecule. 24 h post transfection, FAS was added to the medium from a 100 mM stock solution yielding a final concentration of 2.5 mM. Twenty four hours post addition of FAS, cells were assayed for LDH release. In order to evaluate gene-related toxicity in the absence of iron, the assay was performed accordingly but without iron supplementation and cells were assayed 48 h post transfection. The Luciferase-based viability assay (RealTime-Glo™ MT Cell Viability Assay, Promega) was performed according to the protocol of the manufacturer in 96-well plate format as an endpoint measurement. Luminescence readings were taken on a Centro LB 960 (Berthold Technologies) at 0.5 s acquisition time.

Electron microscopy. Please refer to Supplementary Methods in the Supplementary Information for a detailed description of the electron microscopy techniques used.

Data availability. Data are available upon reasonable request to the corresponding author. The cryo-EM maps of non-iron loaded and iron loaded encapsulins in HEK293T cells have been deposited under EMDB-4392 and 4393 respectively.

Received: 4 December 2017 Accepted: 16 April 2018
Published online: 18 May 2018

References

1. DeLoache, W. C. & Dueber, J. E. Compartmentalizing metabolic pathways in organelles. *Nat. Biotechnol.* **31**, 320–321 (2013).

2. Küchler, A., Yoshimoto, M., Luginbühl, S., Mavelli, F. & Walde, P. Enzymatic reactions in confined environments. *Nat. Nanotechnol.* **11**, 409–420 (2016).
3. Murat, D., Quinlan, A., Vali, H. & Komeili, A. Comprehensive genetic dissection of the magnetosome gene island reveals the step-wise assembly of a prokaryotic organelle. *Proc. Natl Acad. Sci. USA* **107**, 5593–5598 (2010).
4. Lohße, A. et al. Functional analysis of the Magnetosome Island in *Magnetospirillum gryphiswaldense*: the mamAB operon is sufficient for magnetite biomineralization. *PLoS ONE* **6**, e25561 (2011).
5. Heinhorst, S. & Cannon, G. C. A new, leaner and meaner bacterial organelle. *Nat. Struct. Mol. Biol.* **15**, 897–898 (2008).
6. Huber, M. C. et al. Designer amphiphilic proteins as building blocks for the intracellular formation of organelle-like compartments. *Nat. Mater.* **14**, 125–132 (2015).
7. Avalos, J. L., Fink, G. R. & Stephanopoulos, G. Compartmentalization of metabolic pathways in yeast mitochondria improves the production of branched-chain alcohols. *Nat. Biotechnol.* **31**, 335–341 (2013).
8. O'Neil, A., Prevelige, P. E., Basu, G. & Douglas, T. Coconfinement of fluorescent proteins: spatially enforced communication of GFP and mCherry encapsulated within the P22 capsid. *Biomacromolecules* **13**, 3902–3907 (2012).
9. Zschoche, R. & Hilvert, D. Diffusion-limited cargo loading of an engineered protein container. *J. Am. Chem. Soc.* **137**, 16121–16132 (2015).
10. Seebeck, F. P., Woycechowsky, K. J., Zhuang, W., Rabe, J. P. & Hilvert, D. A simple tagging system for protein encapsulation. *J. Am. Chem. Soc.* **128**, 4516–4517 (2006).
11. Rurup, W. F., Snijder, J., Koay, M. S. T., Heck, A. J. R. & Cornelissen, J. J. L. M. Self-sorting of foreign proteins in a bacterial nanocompartment. *J. Am. Chem. Soc.* **136**, 3828–3832 (2014).
12. Minten, I. J., Hendriks, L. J. A., Nolte, R. J. M. & Cornelissen, J. J. L. M. Controlled encapsulation of multiple proteins in virus capsids. *J. Am. Chem. Soc.* **131**, 17771–17773 (2009).
13. Comellas-Aragonès, M. et al. A virus-based single-enzyme nanoreactor. *Nat. Nanotechnol.* **2**, 635–639 (2007).
14. Azuma, Y., Zschoche, R., Tinzl, M. & Hilvert, D. Quantitative packaging of active enzymes into a protein cage. *Angew. Chem. Int. Ed. Engl.* **55**, 1531–1534 (2016).
15. Frey, R., Hayashi, T. & Hilvert, D. Enzyme-mediated polymerization inside engineered protein cages. *Chem. Commun.* **52**, 10423–10426 (2016).
16. Patterson, D. P., Prevelige, P. E. & Douglas, T. Nanoreactors by programmed enzyme encapsulation inside the capsid of the bacteriophage P22. *ACS Nano* **6**, 5000–5009 (2012).
17. Patterson, D. P., Schwarz, B., Waters, R. S., Gedeon, T. & Douglas, T. Encapsulation of an enzyme cascade within the bacteriophage P22 virus-like particle. *ACS Chem. Biol.* **9**, 359–365 (2014).
18. Giessen, T. W. & Silver, P. A. A catalytic nanoreactor based on in vivo encapsulation of multiple enzymes in an engineered protein nanocompartment. *ChemBioChem* **17**, 1931–1935 (2016).
19. Choudhary, S., Quin, M. B., Sanders, M. A., Johnson, E. T. & Schmidt-Dannert, C. Engineered protein nano-compartments for targeted enzyme localization. *PLoS ONE* **7**, e33342 (2012).
20. Held, M. et al. Engineering formation of multiple recombinant Eut protein nanocompartments in *E. coli*. *Sci. Rep.* **6**, 24359 (2016).
21. Cai, F., Sutter, M., Bernstein, S. L., Kinney, J. N. & Kerfeld, C. A. Engineering bacterial microcompartment shells: chimeric shell proteins and chimeric carboxysome shells. *ACS Synth. Biol.* **4**, 444–453 (2015).
22. Kedersha, N. L., Heuser, J. E., Chugani, D. C. & Rome, L. H. Vaults. III. Vault ribonucleoprotein particles open into flower-likestructures with octagonal symmetry. *J. Cell Biol.* **112**, 225–235 (1991).
23. Kickhoefer, V. A. et al. Engineering of vault nanocapsules with enzymatic and fluorescent properties. *Proc. Natl Acad. Sci. USA* **102**, 4348–4352 (2005).
24. Slesina, M. et al. Movement of vault particles visualized by GFP-tagged major vault protein. *Cell Tissue Res.* **324**, 403–410 (2006).
25. Wang, M., Abad, D., Kickhoefer, V. A., Rome, L. H. & Mahendra, S. Vault nanoparticles packaged with enzymes as an efficient pollutant biodegradation technology. *ACS Nano* **9**, 10931–10940 (2015).
26. Tanaka, H. & Tsukihara, T. Structural studies of large nucleoprotein particles, vaults. *Proc. Jpn Acad. Ser. B Phys. Biol. Sci.* **88**, 416–433 (2012).
27. Gálvez, N. et al. Comparative structural and chemical studies of ferritin cores with gradual removal of their iron contents. *J. Am. Chem. Soc.* **130**, 8062–8068 (2008).
28. Papaefthymiou, G. C. The Mössbauer and magnetic properties of ferritin cores. *Biochim. Biophys. Acta* **1800**, 886–897 (2010).
29. Gossuin, Y., Gillis, P., Hocq, A., Vuong, Q. L. & Roch, A. Magnetic resonance relaxation properties of superparamagnetic particles. *Wiley Interdiscip. Rev. Nanomed. Nanobiotechnol.* **1**, 299–310 (2009).
30. Douglas, T. et al. Protein engineering of a viral cage for constrained nanomaterials synthesis. *Adv. Mater.* **14**, 415 (2002).
31. McHugh, C. A. et al. A virus capsid-like nanocompartment that stores iron and protects bacteria from oxidative stress. *EMBO J.* **33**, 1896–1911 (2014).
32. Cassidy-Amstutz, C. et al. Identification of a minimal peptide tag for in vivo and in vitro loading of encapsulin. *Biochemistry* **55**, 3461–3468 (2016).
33. He, D. et al. Structural characterization of encapsulated ferritin provides insight into iron storage in bacterial nanocompartments. *Elife* **5**, e18972 (2016).
34. Sutter, M. et al. Structural basis of enzyme encapsulation into a bacterial nanocompartment. *Nat. Struct. Mol. Biol.* **15**, 939–947 (2008).
35. Moon, H., Lee, J., Min, J. & Kang, S. Developing genetically engineered encapsulin protein cage nanoparticles as a targeted delivery nanoplatform. *Biomacromolecules* **15**, 3794–3801 (2014).
36. Moon, H. et al. Genetically engineering encapsulin protein cage nanoparticle as a SCC-7 cell targeting optical nanoprobe. *Biomater. Res.* **18**, 21 (2014).
37. Putri, R. M., Fredy, J. W., Cornelissen, J. J. L. M., Koay, M. S. T. & Katsonis, N. Labelling bacterial nanocages with photo-switchable fluorophores. *ChemPhysChem* **17**, 1815–1818 (2016).
38. Kanekiyo, M. et al. Rational design of an Epstein-Barr virus vaccine targeting the receptor-binding site. *Cell* **162**, 1090–1100 (2015).
39. Giessen, T. W. & Silver, P. A. Converting a natural protein compartment into a nanofactory for the size-constrained synthesis of antimicrobial silver nanoparticles. *ACS Synth. Biol.* **5**, 1497–1504 (2016).
40. Tamura, A. et al. Packaging guest proteins into the encapsulin nanocompartment from *Rhodococcus erythropolis* N771. *Biotechnol. Bioeng.* **112**, 13–20 (2015).
41. Zhang, B. et al. Coordinated protein co-expression in plants by harnessing the synergy between an intein and a viral 2A peptide. *Plant Biotechnol. J.* **15**, 718–728 (2017).
42. Paez-Segala, M. G. et al. Fixation-resistant photoactivatable fluorescent proteins for CLEM. *Nat. Methods* **12**, 215–218 (2015). 4 p following 218.
43. Maynard-Smith, L. A., Chen, L.-C., Banaszynski, L. A., Ooi, A. G. L. & Wandless, T. J. A directed approach for engineering conditional protein stability using biologically silent small molecules. *J. Biol. Chem.* **282**, 24866–24872 (2007).
44. Nickerson, A., Huang, T., Lin, L.-J. & Nan, X. Photoactivated localization microscopy with bimolecular fluorescence complementation (BiFC-PALM) for nanoscale imaging of protein-protein interactions in cells. *PLoS ONE* **9**, e100589 (2014).
45. Dixon, A. S. et al. NanoLuc complementation reporter optimized for accurate measurement of protein interactions in cells. *ACS Chem. Biol.* **11**, 400–408 (2016).
46. Stritzker, J. et al. Vaccinia virus-mediated melanin production allows MR and optoacoustic deep tissue imaging and laser-induced thermotherapy of cancer. *Proc. Natl Acad. Sci. USA* **110**, 3316–3320 (2013).
47. Jathoul, A. P. et al. Deep in vivo photoacoustic imaging of mammalian tissues using a tyrosinase-based genetic reporter. *Nat. Photonics* **9**, 239–246 (2015).
48. Ntziachristos, V. Going deeper than microscopy: the optical imaging frontier in biology. *Nat. Methods* **7**, 603–614 (2010).
49. Ntziachristos, V. & Razansky, D. Molecular imaging by means of multispectral optoacoustic tomography (MSOT). *Chem. Rev.* **110**, 2783–2794 (2010).
50. Raposo, G. & Marks, M. S. Melanosomes--dark organelles enlighten endosomal membrane transport. *Nat. Rev. Mol. Cell Biol.* **8**, 786–797 (2007).
51. Hasegawa, T. Tyrosinase-expressing neuronal cell line as in vitro model of Parkinson's disease. *Int. J. Mol. Sci.* **11**, 1082–1089 (2010).
52. Sendovski, M., Kanteev, M., Ben-Yosef, V. S., Adir, N. & Fishman, A. First structures of an active bacterial tyrosinase reveal copper plasticity. *J. Mol. Biol.* **405**, 227–237 (2011).
53. Lam, S. S. et al. Directed evolution of APEX2 for electron microscopy and proximity labeling. *Nat. Methods* **12**, 51–54 (2015).
54. Wittig, I., Braun, H.-P. & Schägger, H. Blue native PAGE. *Nat. Protoc.* **1**, 418–428 (2006).
55. Dunleavy, R., Lu, L., Kiely, C. J., McIntosh, S. & Berger, B. W. Single-enzyme biomineralization of cadmium sulfide nanocrystals with controlled optical properties. *Proc. Natl Acad. Sci. USA* **113**, 5275–5280 (2016).
56. Jones, S. R. et al. Genetic and biochemical investigations of the role of MamP in redox control of iron biomineralization in Magnetospirillum magneticum. *Proc. Natl Acad. Sci. USA* **112**, 3904–3909 (2015).
57. Kerner, M. J. et al. Proteome-wide analysis of chaperonin-dependent protein folding in *Escherichia coli*. *Cell* **122**, 209–220 (2005).
58. Wilhelm, M. et al. Mass-spectrometry-based draft of the human proteome. *Nature* **509**, 582–587 (2014).
59. Giessen, T. W. & Silver, P. A. Widespread distribution of encapsulin nanocompartments reveals functional diversity. *Nat. Microbiol.* **2**, 17029 (2017).
60. Matsumoto, Y. & Jasanoff, A. T2 relaxation induced by clusters of superparamagnetic nanoparticles: Monte Carlo simulations. *Magn. Reson. Imaging* **26**, 994–998 (2008).

61. Giessen, T. W. Encapsulins: microbial nanocompartments with applications in biomedicine, nanobiotechnology and materials science. *Curr. Opin. Chem. Biol.* **34**, 1–10 (2016).
62. Meister, M. Physical limits to magnetogenetics. *Elife* **5**, e17210 (2016).
63. Wang, Q., Mercogliano, C. P. & Löwe, J. A ferritin-based label for cellular electron cryotomography. *Structure* **19**, 147–154 (2011).
64. Matsumoto, Y., Chen, R., Anikeeva, P. & Jasanoff, A. Engineering intracellular biomineralization and biosensing by a magnetic protein. *Nat. Commun.* **6**, 8721 (2015).
65. Risco, C. et al. Specific, sensitive, high-resolution detection of protein molecules in eukaryotic cells using metal-tagging transmission electron microscopy. *Structure* **20**, 759–766 (2012).
66. Shu, X. et al. A genetically encoded tag for correlated light and electron microscopy of intact cells, tissues, and organisms. *PLoS Biol.* **9**, e1001041 (2011).
67. Joesch, M. et al. Reconstruction of genetically identified neurons imaged by serial-section electron microscopy. *Elife* **5**, e15015 (2016).
68. Martell, J. D. et al. Engineered ascorbate peroxidase as a genetically encoded reporter for electron microscopy. *Nat. Biotechnol.* **30**, 1143–1148 (2012).
69. Wickersham, I. R., Finke, S., Conzelmann, K.-K. & Callaway, E. M. Retrograde neuronal tracing with a deletion-mutant rabies virus. *Nat. Methods* **4**, 47–49 (2007).
70. Chang, Y.-W. et al. Correlated cryogenic photoactivated localization microscopy and cryo-electron tomography. *Nat. Methods* **11**, 737–739 (2014).
71. van den Heuvel, R. H. H. et al. Improving the performance of a quadrupole time-of-flight instrument for macromolecular mass spectrometry. *Anal. Chem.* **78**, 7473–7483 (2006).
72. Lorenzen, K., Versluis, C., van Duijn, E., van den Heuvel, R. H. H. & Heck, A. J. R. Optimizing macromolecular tandem mass spectrometry of large non-covalent complexes using heavy collision gases. *Int. J. Mass. Spectrom.* **268**, 198–206 (2007).
73. Snijder, J., Rose, R. J., Veesler, D., Johnson, J. E. & Heck, A. J. R. Studying 18 MDa virus assemblies with native mass spectrometry. *Angew. Chem. Int. Ed. Engl.* **52**, 4020–4023 (2013).
74. Veesler, D. et al. Architecture of a dsDNA viral capsid in complex with its maturation protease. *Structure* **22**, 230–237 (2014).
75. Desai, M., Slusarczyk, A. L., Chapin, A., Barch, M. & Jasanoff, A. Molecular imaging with engineered physiology. *Nat. Commun.* **7**, 13607 (2016).

Acknowledgements

We are grateful for support from the European Research Council under grant agreements ERC-StG: 311552 (F.S., A.S., H.R., G.G.W.). T.W., J.S. and A.J.R.H acknowledge support from the Netherlands Organization for Scientific Research (NWO) funding the large-scale proteomics facility Proteins@Work (project 184.032.201) embedded in the Netherlands Proteomics Centre. We acknowledge Susanne Pettinger for assistance with DLS measurements.

Author contributions

F.S. co-designed the study, generated all constructs, conducted all cell and biochemical experiments, analyzed data, generated figures and co-wrote the manuscript; C.M. made important contributions to the iron-loading experiments and performed in vitro MRI experiments; P.E. designed, conducted and analyzed cryo-EM experiments supervised by J.P.; A.S. supported cell experiments; H.R. supported animal experiments; M.D. and S.B. conducted in vivo MRI experiments supervised by A.J.; A.G. helped with HPLC purification and DLS analysis; T.P.W. and J.S. conducted and analyzed native mass spectrometry experiments supervised by A.J.R.H., H.F. and M.H. supervised in vitro MRI experiments; V.N. supervised MSOT experiments; G.G.W. conceptualized and co-designed the study, analyzed data and generated figures, supervised the project, and wrote the manuscript.

Additional information

Supplementary Information accompanies this paper at https://doi.org/10.1038/s41467-018-04227-3.

Competing interests: The authors declare no competing interests.

Reprints and permission information is available online at http://npg.nature.com/reprintsandpermissions/

Publisher's note: Springer Nature remains neutral with regard to jurisdictional claims in published maps and institutional affiliations.

4.2 Violacein as a genetically-controlled, enzymatically amplified and photobleaching-resistant chromophore for optoacoustic bacterial imaging

The second publication named '*Violacein as a genetically-controlled, enzymatically amplified and photobleaching-resistant chromophore for optoacoustic bacterial imaging*' describes a novel class of reporters genes for optoacoustic (OA) imaging [2]. The gene reporter is based on the enzymatic turnover of the amino acid L-tryptophane to the small highly absorbing molecule 'Violacein' by five proteins encoded by the Vio operon. Importantly, Violacein is highly bleaching resistant and has substantial absorption in near-infrared (NIR) range, which are vital characteristics for OA probes. In the study, we transfer the genes responsible for Violacein to *E.coli* and image these Violacein-producing bacteria *in vitro* for characterization purposes and *in vivo* in a mouse tumor model at high resolution at depths up to 1 mm. We demonstrate that Violacein possesses anti-tumoral activity and thus reason that genetically engineered bacteria producing Violacein could serve as theranostic agents in the future allowing for imaging tumors in deep tissue regions while treating them at the same time.

In the study, I am sharing the first authorship with my former colleague Yuanyuan Jiang, a bio-medical imaging specialist, who took over the engineering part in the study. Specifically, I co-designed the concept and performed all molecular biology work shown in the study including generation of the genetically modified bacteria, cultivation of the latter and sample preparation of all samples utilized in the study. Furthermore, I assisted in measuring the bacterial suspensions in the optoacoustic spectrometer setup.

SCIENTIFIC REPORTS

OPEN

Violacein as a genetically-controlled, enzymatically amplified and photobleaching-resistant chromophore for optoacoustic bacterial imaging

Received: 04 December 2014
Accepted: 14 May 2015
Published: 19 June 2015

Yuanyuan Jiang[1,2,*], Felix Sigmund[1,2,*], Josefine Reber[1], Xosé Luís Deán-Ben[1], Sarah Glasl[1], Moritz Kneipp[1,3], Héctor Estrada[1], Daniel Razansky[1,3], Vasilis Ntziachristos[1,3] & Gil G. Westmeyer[1,2,4]

There is growing interest in genetically expressed reporters for *in vivo* studies of bacterial colonization in the context of infectious disease research, studies of the bacterial microbiome or cancer imaging and treatment. To empower non-invasive high-resolution bacterial tracking with deep tissue penetration, we herein use the genetically controlled biosynthesis of the deep-purple pigment Violacein as a photobleaching-resistant chromophore label for *in vivo* optoacoustic (photoacoustic) imaging in the near-infrared range. We demonstrate that Violacein-producing bacteria can be imaged with high contrast-to-noise in strongly vascularized xenografted murine tumors and further observe that Violacein shows anti-tumoral activity. Our experiments thus identify Violacein as a robust bacterial label for non-invasive optoacoustic imaging with high potential for basic research and future theranostic applications in bacterial tumor targeting.

Optoacoustic imaging comes with a strong potential for non-invasive cell-fate tracking, by enabling high-resolution cell visualization inside living tissues much deeper than what is possible with optical microscopy[1]. To enable optoacoustic cell detection with high sensitivity, labeling agents with a high molar absorbance (extinction) coefficient, low quantum yield and minimum photobleaching are desired[2]. For *in vivo* studies, genetic encoding of reporter chromophores may be superior to labeling approaches using synthetic dyes as it avoids signal loss due to serial dilutions of the contrast agent during cellular divisions.

Imaging bacterial populations in entire living host organisms is of increasing interest for infectious disease research[3], studies of the microbiome[4], as well as for theranostic applications in cancer research based on bacterial tumor targeting[5,6]. The latter approach relies on the preferential clonal expansion of bioengineered bacteria in the nutrient-rich, anaerobic and immunocompromised tumor microenvironment. Bacterial localization and tumor colonization can be determined by detecting reporter gene expression in targeted bacteria. So far, the luciferin-luciferase system[7,8] ferritin[9], magnetotactic bacteria[10], or thymidine kinase[11] have been employed as gene reporters for *in vivo* detection of bacterial colonization via bioluminescence, MRI, and PET imaging respectively. As for optoacoustic readout, point measurements of circulating bacteria tagged with nanoparticle-conjugated antibodies have been performed

[1]Institute for Biological and Medical Imaging (IBMI), Helmholtz Zentrum München, Neuherberg, Germany. [2]Institute of Developmental Genetics (IDG), Helmholtz Zentrum München, Neuherberg, Germany. [3]Chair for Biological Imaging, Technische Universität München (TUM), Munich, Germany. [4]Department of Nuclear Medicine, Technische Universität München (TUM), Munich, Germany. *These authors contributed equally to this work. Correspondence and requests for materials should be addressed to G.G.W. (email: gil.westmeyer@tum.de)

within blood vessels[12]. However, robust detection of genetically labeled bacteria *in vivo* via optoacoustic imaging has so far not been accomplished. One reason for this may be that common fluorescent proteins or chromoproteins often exhibit poor photostability making it challenging to obtain robust signals in optoacoustic imaging applications[13]. In contrast, enzymatically generated biosynthetic pigments such as melanin have the advantage of signal amplification because each genetically expressed enzyme can turn over many substrates per unit time. Although melanin produced in tyrosinase-overexpressing eukaryotic cells can be imaged by optoacoustics[14,15], this approach has not yet been successfully transferred to bacterial optoacoustic imaging. In addition to melanin, other biosynthetic pigments such as riboflavin, canthaxanthin, carotenoids or Violacein (Vio) have been expressed in bacterial hosts for simple color differentiation by visual inspection[16,17]. The deep violet chromophore Violacein is of particular interest for detection in tissue as it has an absorbance spectrum peaking around 590 nm with substantial absorbance above 650 nm. Vio is enzymatically generated from the sole precursor tryptophan by five enzymes (VioA-E) that have originally been cloned from *Chromobacterium violaceum*[18]. While there may be a putative protective function of the violet pigment against visible radiation, Vio has also been reported to exert anti-protozoal and anti-tumoral activity against several tumor types[19–22].

In search for a potent bacterial label that affords high-resolution, three dimensional bacterial imaging in tissues, we characterized the photophysical and biochemical properties of Vio with respect to optoacoustic detection and interrogated its performance as a bacterial label for optoacoustic imaging compared to melanin or fluorescent proteins. We further performed *in vivo* studies to characterize the capacity to detect Vio-labeled bacteria by multispectral optoacoustic tomography (MSOT) in tumor-bearing mice.

Results

We grew cultures of *E. coli* expressing the Violacein operon encoding the essential set of five enzymes (VioA-E) in the biosynthetic pathway for the production of Vio. As a reference chromophore we expressed the common fluorescent protein mCherry because of its comparable absorbance spectra and its prior use in optoacoustic imaging[23]. To compare the optoacoustic spectra of Vio and mCherry, we loaded cell culture flow chips with bacterial solutions of equal density (Fig. 1A) and placed them into a custom-built optoacoustic spectrometer connected to a tunable visible laser[24]. Vio-expressing bacteria exhibited a peak optoacoustic signal at ~590 nm with substantial signal still measurable above 650 nm (Fig. 1B), while mCherry expressing bacteria showed a slightly narrower optoacoustic spectrum peaking at 590 nm (absorbance peaks corresponded to optoacoustic signal maxima).

We subsequently measured the kinetics of Vio pigment formation in comparison to cells overexpressing tyrosinase, the rate-limiting enzymatic step for melanin synthesis. We thus serially sampled from culture flasks of *E. coli* expressing the respective chromophore and plotted the absorbance at 590 nm. Whereas the absorbance of mCherry plateaued around 16 hours after inoculation, Vio expressing cells reached a 1.6 fold higher value in absorbance with a continuing upward trend (Fig. 1C). In comparison, no substantial absorbance increase could be measured from the tyrosinase overexpressing cells grown in a shaking incubator; considerable melanin production could only be observed when bacteria were grown on agar plates supplemented with copper and L-tyrosine for a minimum of 48 hours (data not shown).

We were next interested in assessing the resistance of the chromophores against photobleaching, a critical requirement for obtaining robust signals in optoacoustic imaging. We first measured photobleaching with the optoacoustic spectrometer at 590 nm (Fig. 1D). Whereas mCherry expressing bacteria photobleached with a time constant of ~2150 pulses (95% confidence interval: 1940 to 2401), Vio-producing bacteria did not show significant bleaching after 25 thousand pulses *i.e.* over a duration of ~8 minutes.

The strong differences in bleaching rates have important consequences for the detectability of the different chromophores in optoacoustic microscopy, which achieves high spatial resolution but requires relatively high laser fluence[25].

We filled ~4 mm diameter circular wells in an agar phantom with ~20 μL of the same bacterial solutions used to obtain the optoacoustic spectrum shown in Fig. 1B. The bacteria-containing agar phantom was then placed in an optoacoustic microscopy setup. Figure 2 displays images obtained from the upper right quadrant of the circular wells showing robust optoacoustic contrast from the Vio producing cells in repeated images as quantified by signal averaging over the indicated ROIs (Fig. 2B). In contrast, the signal from mCherry bleached very rapidly under the focused illumination of the microscopy system such that the signal averaged over the ROI indicated in the image (Fig. 2A) only marginally exceeded that of non-expressing control cells (Fig. 2B). This is remarkable since the identical sample of mCherry measured in the optoacoustic spectrometer on the same day yielded a signal that was 30% of that of Vio (Fig. 1B). To further quantify photobleaching of Vio-containing bacteria, we repeated a line scan through the top well over one minute (magnification in Fig. 2A) to deposit additional ~60 thousand pulses, resulting in a reduction of the signal to approximately 35% of that from the same region in the first image. When focusing the laser on a single 20 μm spot of the sample (~15 μJ average per-pulse energy), bleaching of Vio occured with a time constant of about 670 pulses (95% confidence interval: 664 to 675) while bleaching of mCherry happened so rapidly that the optoacoustic signal (averaged over the first 10 pulses) was only ~1.5 times higher than that of non-expressing control bacteria and only 1% of that expected from measurements of the identical sample on the optoacoustic spectrometer (Fig. 1B). In an independent experiment, we also compared the photobleaching rate of melanin-producing bacteria

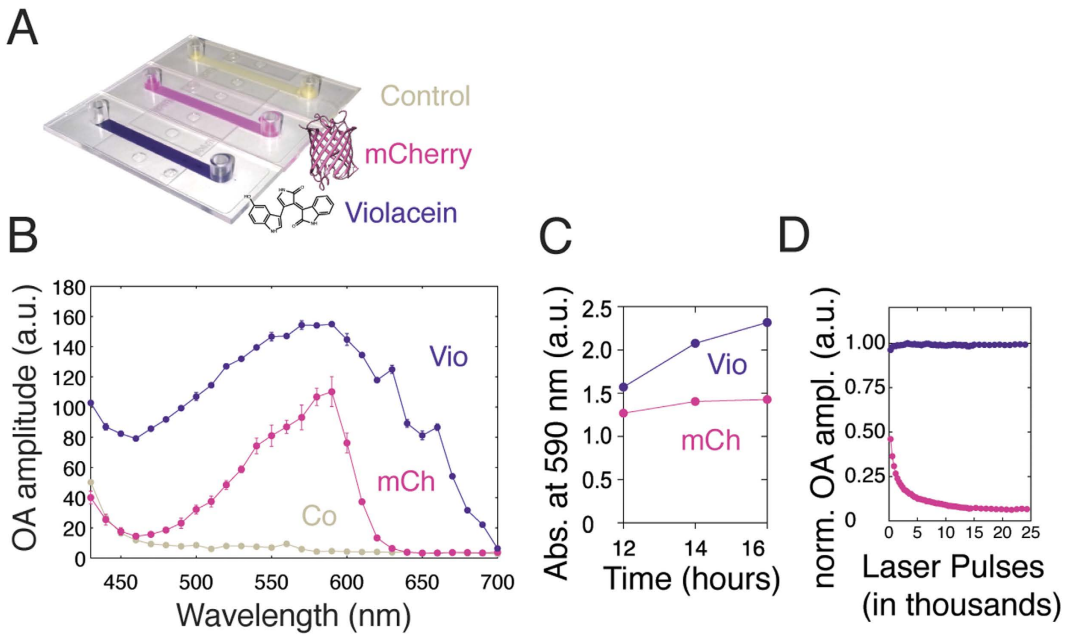

Figure 1. Comparison of photophysical parameters of Violacein-producing (Vio) and mCherry-expressing (mCh) bacteria. (**A**) Photograph of flow chips filled with bacterial suspensions producing the pigment Violacein (chemical structure shown), mCherry (protein structure shown) or control bacteria. (**B**) Optoacoustic spectra for both chromophore-containing bacterial strains and control bacteria (Co). (**C**) Time profile of chromophore production as measured by the absorbance increase at 590 nm. (**D**) Kinetics of photobleaching upon laser illumination at 590 nm.

scraped off from confluent agar plates after 48 hours of growth (no substantial melanin production was observed in cultures grown in a shaking incubator). The resulting time constant for bleaching of the melanin-containing bacteria (imaging data not shown) was about 217 pulses (95% confidence interval: 215 to 219 pulses) and was slightly shorter than that for an equally small volume of Vio (264 pulses; 95% confidence interval: 261 to 268).

After characterizing the optoacoustic properties of Vio-expressing bacteria *in vitro*, we subsequently studied how well they can be detected in tumor-bearing mice by volumetric multispectral optoacoustic tomography (MSOT). We thus injected Vio-expressing (or non-expressing) bacterial suspensions into tumors grown from 4T1 mammary carcinoma cells xenografted a week prior to the imaging experiment.

We subsequently acquired multispectral optoacoustic images from the tumors with a portable three-dimensional optoacoustic imaging system connected to a tunable laser in the visible range[26]. Figure 3 shows the rendered 3D views of three tumors injected with Vio-containing bacteria and three tumors injected with control bacteria together with 2D projections taken through the center of each tumor juxtaposed with the corresponding cryomicrotome slice (insets). Vio-expressing bacteria could be clearly localized within the tumor tissue from the imaging data acquired at 650 nm (white-blue color scale), a wavelength at which Vio still generates substantial optoacoustic signal while the absorbance from blood is strongly reduced. Anatomical contrast is provided by displaying the data acquired at 490 nm on a color scale ranging from white to red. The variable distribution of Vio across animals, probably due to different injection mechanics into the differently shaped subcutaneous tumors, is detected with good agreement between the optoacoustic imaging and photographs taken from *ex vivo* axial cryomicrotome sections. In the first tumor, the distribution of Vio was widespread reaching superficial layers as also detected by a commercial optoacoustic imaging system with 100 μm in plane resolution using a near-infrared laser at 680 nm (Supplementary Fig. 1A). In the second tumor, Vio was located deeper in the tissue (~2.5 mm from the surface) as visualized by the cutaway 3D view and the 2D slice reconstructed from the optoacoustic data and the corresponding histological section. In the third tumor, a slightly smaller amount of Vio or control bacteria was injected at multiple positions within the tumor. Vio-expressing and control bacteria could also be detected in the tumor by immunohistochemistry (supplementary Fig. 1B). These imaging data demonstrate that the strong absorption of Vio-producing bacteria close to the near-infrared window labels tumors with good depth-resolution and high contrast-to-noise ratio (268 ± 59, mean $\pm$standard deviation) as compared with tumors filled with non-expressing controls (21 ± 6).

With respect to possible future theranostic applications of Vio-expressing bacteria in bacterial tumor targeting, we also tested the anti-tumoral activity of purified Vio in a cell viability assay (MTT) on 4T1

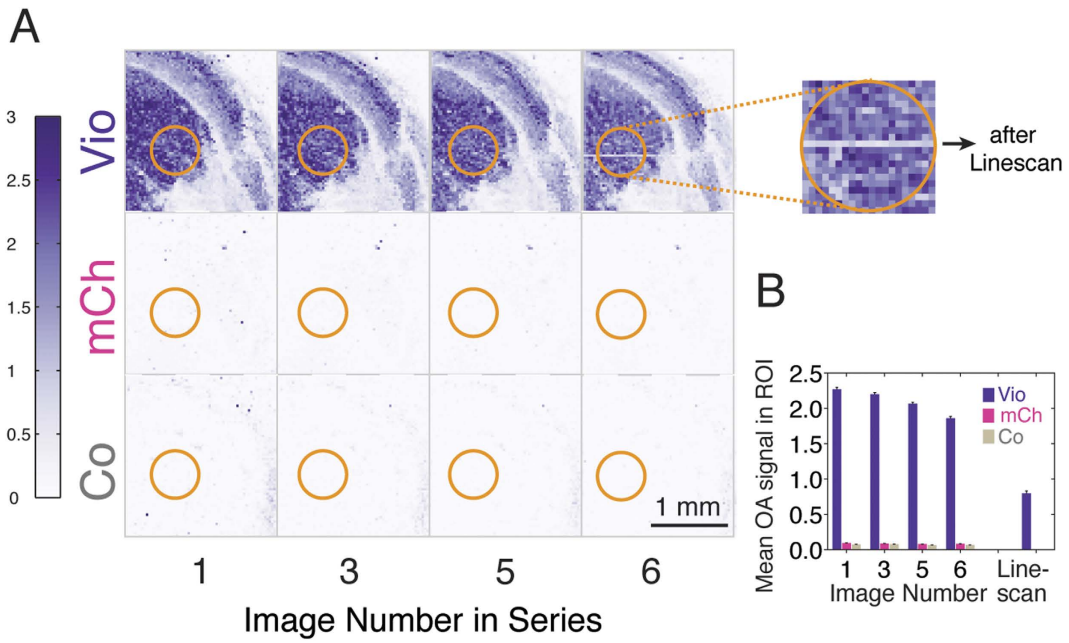

Figure 2. Optoacoustic microscopy images of bacterial suspensions. (**A**) Bacterial suspensions producing Violacein (Vio) or mCherry (mCh) and non-expressing controls (Co) were filled in circular wells of an agar phantom (~4 mm diameter, only upper right quadrant is shown) and sequentially imaged to assess image contrast and photobleaching. Repeated linescans were acquired through the well containing bacteria expressing Vio (magnification). (**B**) Optoacoustic signals for the three bacterial suspensions were averaged over the circular ROIs indicated in the figure (orange) at each time point. To assess the photobleaching after the line scan, all pixel intensities in the trajectory of the laser were averaged.

tumor cells in culture (Fig. 4A). Significant reductions in tumor cell viability were observed at five nanomolar concentrations (one-way ANOVA with $p < 0.0001$; multiple comparisons against vehicle control with $p < 0.05$, Bonferroni corrected) with stronger effects measured after incubation with hundreds of nanomolar of Vio. We have furthermore assessed the effect of Vio released from bacteria via antibiotic treatment and found a significant effect (paired t-test, $p < 0.0001$) on 4T1 cell viability as compared to control bacteria (Fig. 4B).

This line of experiments thus jointly identifies Violacein as a photobleaching-resistant, high contrast-to-noise, genetically controlled and enzymatically amplified chromophore-label for non-invasive optoacoustic localization of bacteria in tumors of living mice with potential for future theranostic applications.

Discussion

There is growing interest in longitudinal *in vivo* imaging of bacterial colonization as a method for determining the routes and bacterial burden of infections[27–29], studying the microbiota[4] and visualizing tumors via bacterial tumor targeting[8]. A general requirement for these imaging concepts is that the labeling agent is not diluted upon cellular divisions, which can occur at a fast rate in bacterial populations. This constitutes a strong advantage of genetically encoded contrast agents over synthetic labels as the genetic information is copied over to the progeny.

So far, mostly bioluminescent imaging has been used for bacterial tracking resulting in limited spatial resolution[7]. To enable three-dimensional imaging at much higher resolution via optoacoustics, we here focused on an enzymatically generated, photobleaching-resistant pigment and found it to be a potent bacterial label for optoacoustics. We were able to robustly detect ~6×10^9 cfu bacteria in tumors, a number that is in the range of what was determined in tumor-tracking experiments after about one week of intratumoral bacterial growth post intravenous injection[6,30].

With respect to alternative genetic labels for optoacoustic bacterial imaging, Vio has several advantages over common labeling strategies based on fluorescent proteins. First, the non-fluorescent pigment Vio is more efficient in converting the absorbed energy into thermoelastic expansion than fluorescent proteins that re-emit a portion of the absorbed photons. Second, even if chromoproteins optimized for low fluorescence are used[13], each genetically expressed protein only harbors one chromophore, whereas many Vio pigments can be synthetized from the abundant substrate tryptophan by each instance of the enzymatic chain. This enzymatic amplification increases the sensitivity of bacterial detection, especially if only low protein expression levels can be achieved. Third, Vio is much more photobleaching-resistant than the common fluorescent protein mCherry. This advantage of the biosynthetic pigment likely carries

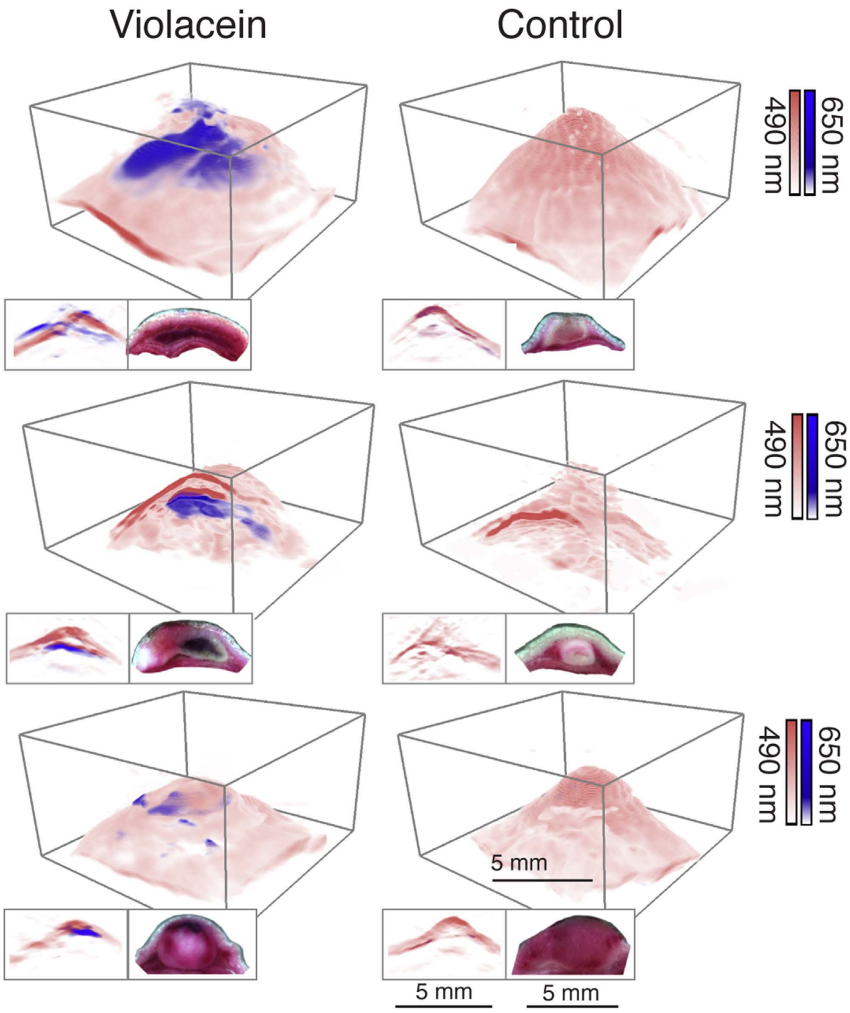

Figure 3. ***In vivo*** **optoacoustic imaging of bacterially labeled 4T1 tumors in mice.** Rendering of multispectral 3D optoacoustic data obtained from 4T1 tumors grafted in mice containing Violacein-expressing bacteria (first column) or non-expressing controls (second column). The white-to-blue and white-to-red color maps indicate the signal amplitudes of data acquired at 650 nm and 490 nm respectively. The insets underneath each 3D view show optoacoustic axial cross sections through the center of the volume (left) juxtaposed with color images of cryomicrotome sections through the *ex vivo* tumors (right).

over to chromoproteins with optimized photobleaching resistance as they were shown to exhibit a sharp signal decay when illuminated with three orders of magnitude lower fluence than was used here on the microscopic optoacoustic system[13]. In this regard it is interesting to investigate the maximum photostability that can be achieved with chromophores built from cyclized amino acids (as in *e.g.* proteins derived from Green Fluorescent Protein (GFP)) compared with chromophores bound to the protein backbone (such as biliverdin and infrared fluorescent protein (iRFP)[31]) or (bio)synthetic dyes.

With respect to the goal of non-invasive tracking of bacterial colonization, it is furthermore desired that the cellular contrast agent is generated with fast kinetics to match the rapid bacterial growth. Based on the data presented here, bacteria expressing the Violacein operon showed fast production of Vio that did not show the early saturation of the optoacoustic signal measured from the mCherry-expressing bacteria; this could be explained by the shorter life time of the fluorescent protein as compared with that of the pigment Vio. It is furthermore of interest that the multi-enzymatic biosynthesis of Vio outperformed melanin production from tyrosinase overexpressing cells. In our hands, those cells produced melanin only with supplementation of excess tyrosine and the cofactor copper and only when grown on agar plates for a minimum of 48 hours. Growth could however not be achieved in shaking cultures for even after 24 hours of incubation. This points to an advantage of Vio as a genetic bacterial label as all steps of its synthesis are enzymatically catalyzed and do not rely on spontaneous cyclization necessary for the maturation of many chromoproteins or polymerization reactions as in the case of melanin formation.

In summary, we have shown that Vio is an excellent biosynthetic contrast agent for optoacoustic bacterial detection *in vivo* that very favorably compares with a common fluorescent protein (mCherry) or the

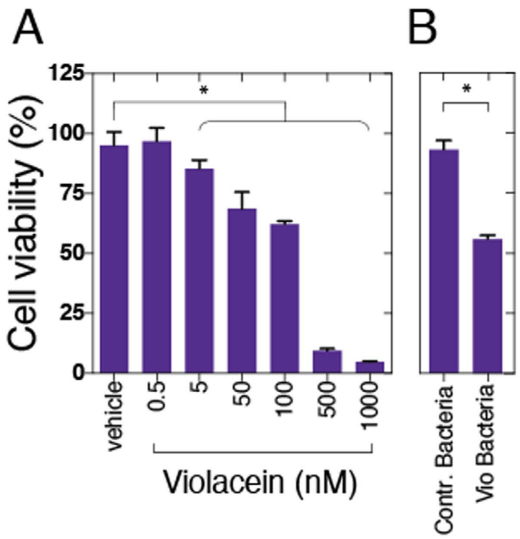

Figure 4. Effects of Violacein on cell viability of cultured 4T1 tumor cells. 4T1 cells were grown in 96 well plates, treated with nanomolar concentrations of pure Violacein (**A**) or Violacein released from bacteria (**B**) to compare cell viability against vehicle-treated cells (MTT assay).

biosynthetic pigment melanin. Vio generates a strong optoacoustic signal close to the near-infrared range and exhibits high photobleaching resistance. The bacterial production of Vio is enzymatically amplified, fast and robust. Vio-expressing bacteria can be differentiated well by multispectral optoacoustic imaging from strongly vascularized xenografted tumors in living mice. Vio's distinct optoacoustic spectrum may also afford multiplexing applications for bacterial detection together with optimized chromoproteins or biosynthetic pigments such as melanin (if bacterial production of the latter can be optimized). The robust enzymatic amplification and fast pigment formation of the Violacein system also qualify it as an effective output of weaker promoters or genetic circuits that may be introduced to turn the bacterium into a whole-cell sensor for environmental parameters or analytes of interest[32]. In the context of bacterial tumor tracking, it may be of particular interest to couple Vio production to sensing of *e.g.* vascular growth factors or hypoxic conditions. With respect to an extension of this concept for future theranostic applications, it is also intriguing to study the anti-cancer activity of Violacein-expressing bacteria *in vivo* and investigate whether the release of Violacein could be coupled to genetic sensor circuits and/or placed under pharmacogenetic control[33]. Non-invasive control over Vio's anti-tumoral activity may also be effectively achieved via antibiotic drugs or cell-permeabilization by laser illumination or highly focused ultrasound.

Methods

Genetic reporter constructs and bacterial growth. pVIO1-2 was created by Sánchez *et al.*[18], by isolating the vio locus (VioA-E) from genomic DNA of *Chromobacterium violaceum* (ATCC12472) as an 8.9 kb MluI-XhoI fragment and subcloning it into lac promoter driven LITMUS 38 with MluI and SalI. MelA from *Rhizobium etli* was amplified from pTrc MelA (kindly provided by Dr. Guillermo Gosset Lagarda) and subcloned into pmCherry with AgeI and NotI. pVIO1-2 (kindly provided by Dr. José A. Salas), pmCherry (kind gift from Dr. Arie Geerlof, Helmholtz Zentrum München), pMelA and pUC19 (control bacteria) were transformed into TOP10 Chemically Competent *E. coli* (Invitrogen Carlsbad, CA, USA) according to the protocol of the manufacturer. Single colonies were picked and inoculated into 250 mL LB-medium containing 100 μg/mL ampicillin. Cultures were grown for 18 h at 37 °C and 250 rpm. Violacein-producing bacteria showed no statistically significant difference to control bacteria (Wilcoxon matched-Pairs Signed-Ranks Test) with respect to cell viability (BacTiter-Glo™luciferase assay) or cell wet weight. Plasmid retention was tested *in vitro* and showed that the bacteria retain the plasmid without selection pressure for at least 7 days without any significant loss of violacein production.

To yield bacterial suspensions, cultures were spun down at 4000 rpm for 15 min at 4 °C and resuspended in 25% (weight PBS/wet weight bacteria) in PBS. As no substantial melanin formation was observed from MelA expressing bacteria in liquid culture, MelA expressing bacteria were grown on LB agar plates supplemented with 2 mM L-tyrosine and 400 μM $CuSO_4$ for 48 h. For photobleaching experiments, MelA expressing bacteria were scraped off the plates and resuspended in 50% (weight PBS/wet weight bacteria) PBS.

Assessing chromophore maturation times. Single colonies of *E. coli* TOP10 cells transformed with pVIO1–2 or pmCherry were picked and inoculated into 250 mL LB medium containing 100 μg/mL

ampicillin. At 12, 14 and 16 h of growth time, 50 mL of the bacterial cultures were spun down at 4000 rpm for 15 min at 4 °C and resuspended in 25% (weight PBS/wet weight bacteria) in PBS. For absorbance measurements, bacterial suspensions were diluted 1:5 in PBS and absorbance was measured at 590 nm on a SpectraMax M5 (Molecular Devices, Sunnyvale, USA).

Measurement of optoacoustic spectra. Cell culture flow chips (μ-Slide I 0.2 Luer, hydrophobic, uncoated, sterile, IBIDI, Martinsried, Germany) were connected to plastic tubing and placed upside down into a sample holder fixed to the frame of a custom-built optoacoustic spectrometer. The flow channel's thin transparent foil was placed in the acoustic focus of the ultrasound detector (V382-SU, 3.5 MHz Immersion Transducer, Olympus, Hamburg, Germany) mounted on the device's plexiglas roof. The device was then placed resting on an optical table within a water basin to ensure acoustic coupling between the sample and the ultrasound detector. The output of a tunable visible laser (SpitLight DPSS 250, Innolas, Krailling, Germany) was guided onto the flow channel of the cell culture chip via mirrors. *E. coli* suspensions with weight-adjusted densities were sequentially injected into the flow channel of the cell culture chip via the tubing and optoacoustic signals were recorded (NI USB-5133, National Instruments, Austin, Texas, USA connected to a standard computer) as a function of laser wavelength. The flow channel was washed in between measurements with 10 channel volumes of PBS such that no optoacoustic signal remained. PBS was then pushed out of the channel by injecting air to ensure that no dilution or inhomogeneity of subsequent samples occurred. A laser power meter (FieldMaxII-TOP, Coherent Inc. Santa Clara, USA) was used to measure the laser power as a function of wavelength to normalize the optoacoustic signal amplitude for each wavelength applying custom routines implemented in MATLAB (Mathworks, Natick, USA). Absorbance measurements were taken on a plate reader (SpextraMax M5, Molecular Devices, Sunnyvale, USA). Spectra are shown as mean values with error bars representing the standard error of the mean. Photobleaching for these illumination conditions was assessed by repeated measurements at 590 nm for Vio. Curves were plotted and fitted with a monophasic exponential decay function or linear regression using GraphPad Prism 6 (GraphPad, La Jolla, USA). Figures were prepared in Adobe Illustrator. The mCherry structure shown as inset in Fig. 1 A was generated from PDB entry 2H5Q using UCSF Chimera.

Optoacoustic *in vitro* microscopy. Bacterial suspensions (20 μL of the same suspension from which optoacoustic spectra were obtained) were filled into an agar phantom (1.3% agarose in PBS) containing three circular wells of ~4 mm diameter and positioned under the motorized stage-mounted coaxial optoacoustic head of an optoacoustic microscope adapted from Estrada *et al.*[24]. The optical excitation was provided by a pump laser Nd:YAG Q-switched laser (model IS8II-E, Edge- Wave GmbH, Wuerselen, Germany) feeding a dye laser (Credo, Sirah Lasertechnik GmbH, Grevenbroich, Germany) loaded with Pyrromethene 597 dye (maximum wavelength conversion efficiency at 585 nm) tuned to 594 nm. By means of a Gradient-Index (GRIN) lens assembly, the system generated a diffraction-limited 20 μm diameter (FWHM) optical focus at the acoustic focus of the 30 MHz polyvinylidene difluoride (PVdF) ultrasound detector (Precision Acoustics, Dorchester, United Kingdom). The average per-pulse energy was maintained at ~15 μJ. Thus high fluence in excess of 2 J/cm^2 were generated at the sample surface. Sequential point measurements were taken over time at the center of the respective sample well (over 15 seconds at 5 kHz laser repetition rate) to measure signal decay due to photobleaching under focused illumination conditions commonly used in optoacoustic microscopy systems. Signal curves were fitted to a monophasic exponential decay function with GraphPad Prism. Subsequently, five spatially resolved optoacoustic measurements were taken repeatedly with both the optical beam and ultrasonic detector quickly scanned across the sample using step-size of 30 μm to assess signal amplitude and photobleaching. Image volumes were reconstructed using custom-written routines[24] implemented in MATLAB and displayed as 2D maximum amplitude projections. Mean optoacoustic signal amplitude were averaged from disk-shaped ROIs with a diameter of 600 μm (error bars represent the standard error of the mean). To further assess the kinetics of photobleaching of Vio, horizontal line scans were taken through the well containing Vio with a pulse repetition frequency of 1 kHz over 1 min in total, before an additional image of all sample wells was acquired.

***In vivo* imaging by means of volumetric multispectral optoacoustic tomography (MSOT).** 8-10 week-old nude mice (matched pairs of Foxn1 - CD1 (f) and Balb/c (m); Harlan Laboratories, Germany) were inoculated with 4T1 cells (1×10^6 cells in 30 μL of PBS) into the subcutis of the neck. After 7 days of tumor growth, animals were deeply anesthetized, placed on a heat-blanket and a total 20 μL of Vio-expressing *E. coli* or control bacteria (~0.5×10^9 cfu/μL, 0.3×10^9 cfu/μL for the pair of datasets displayed on the bottom of Fig. 3) were intratumorally injected at multiple locations within each tumor. Animals were subsequently positioned in supine orientation on a portable volumetric optoacoustic imaging system[25] with acoustic matching provided by optically transparent agar. The system was coupled to a tunable visible laser (SpitLight DPSS 250, Innolas, Krailling, Germany), which provided short-duration (<10 ns) laser pulses with optical wavelengths tuned between 450 to 650 nm in 10 nm increments. Optoacoustic image volumes were acquired and rendered in real time using model-based three-dimensional reconstruction algorithm, essentially retrieving the volumetric distribution of optical absorption at each wavelength with almost isotropic resolution of 200 micrometers[34]. Contrast-to-noise

ratios (CNRs) were computed by placing a cubical ROI (0.027 mm^3) into the tumor, the skin close to the edge of the FOV and background outside of the tissue and taking the absolute difference of signals acquired at 650 nm from tumor and skin divided by the standard deviation of the background noise. The imaging data shown in supplementary Fig. 1 was acquired on an inVision 256-TF system (iThera Medical, Munich, Germany) at 680 nm and 710 nm. All animal experiments were approved by the government of Upper Bavaria and were carried out in accordance with the approved guidelines.

***Ex vivo* sectioning on cyromicrotome.** After completion of imaging, the mice were euthanized with a lethal dose of ketamine/xylazine and frozen to −20 °C. The upper torso including the tumor was embedded in O.C.T (TissueTeck). The embedded tissue was cryosliced along the axial planes every 50 micrometers in a modified Leica cryotome combined with a CCD camera to capture RGB color images from the surface on the bulked remaining sample. For bacterial detection, tissue sections were equilibrated to room temperature and rehydrated in PBS for 10 min and blocked in 3% BSA PBS for 30 minutes at room temperature. Subsequently, tissue sections were incubated with Escherichia coli BioParticles® Opsonizing Reagent (Molecular Probes) diluted 1:100 in PBS for 30 minutes at room temperature. After incubation, slices were washed three times with PBS. Subsequently, slices were incubated with 4 μg/mL goat-anti-rabbit DyLight594 (Abcam ab96897) antibody conjugate for 30 minutes at room temperatures and then washed three times with PBS. Microscopy of the tissue sections was performed on an Olympus IX81 confocal microscope.

Cell viability assay. The 4T1 cell line, a mouse mammary tumor cell line (CRL-2539; American Type Cell Culture Collection, Manassas VA), was grown in 5% CO_2 at 37 °C in RPMI-1640 medium (Sigma-Aldrich) containing 10% fetal bovine serum and antibiotics (penicillin and streptomycin). Routine culture treatment was conducted twice a week. Cells were harvested and seeded in 96-well plates at 2.5×10^3 cell per well in a final volume of 100 μL. After overnight incubation for cell adhesion, the medium was removed, and the cells were incubated at 37 °C with 100 μL of medium containing Vio (0.5 nM–1.0 μM; Vio from *Janthinobacterium lividum*, Sigma-Aldrich), 10% dimethyl sulfoxide (DMSO) as a negative control, 0.1% DMSO as vehicle control of Vio and RPMI medium only to define 100% viable cells. After 24 h of incubation, the medium containing the tested compound was removed and fresh medium was added. Cell viability was determined by a colorimetric cell viability assay (Cell Proliferation Kit 1 (MTT), Roche) used according to the manufacturer's instructions. The absorbance measurement was performed on a microplate reader (Infinite® 200 PRO, Tecan) and was determined at 595 nm, whereby, 651 nm was used as a reference wavelength. To quantify cell viability, the ratio of the absorbance of the samples to the absorbance of the non-treated control samples (=100%) was calculated (the bargraph shows the mean, error bars have the length of one standard deviation). To determine anti-tumoral activity of Vio released from bacteria, Vio-producing and control bacteria were grown for 18 h at 37 °C, which yielded cultures containing around 5 × 10^9 cfu/mL and approximately 10 μM of Vio as determined photospectrometrically after aceton extraction (using an extinction coefficient of 32900 M^{-1} cm^{-1}@ 555 nm). Bacteria were spun down, the supernatant was discarded and the bacteria were resuspended in an equal volume of PBS. In order lyse the bacteria, kanamycin solution was added to yield a final concentration of 50 μg/mL. After, bacteria were incubated for 2 d at RT to achieve complete lysis. Subsequently, bacterial lysates were diluted 1:10 in cell culture medium to yield a concentration of released Vio of approximately 1 μM and used for the MTT assay.

References

1. Ntziachristos, V. Going deeper than microscopy: the optical imaging frontier in biology. *Nat. Methods* **7,** 603–614 (2010).
2. Yao, J. & Wang, L. V. Sensitivity of photoacoustic microscopy. *Photoacoustics* **2,** 87–101 (2014).
3. Melican, K. & Richter-Dahlfors, A. Real-time live imaging to study bacterial infections *in vivo*. *Curr. Opin. Microbiol.* **12,** 31–36 (2009).
4. Rawls, J. F., Mahowald, M. A., Goodman, A. L., Trent, C. M. & Gordon, J. I. *In vivo* imaging and genetic analysis link bacterial motility and symbiosis in the zebrafish gut. *Proc. Natl. Acad. Sci. USA* **104,** 7622–7627 (2007).
5. Cronin, M. *et al.* High Resolution *In Vivo* Bioluminescent Imaging for the Study of Bacterial Tumour Targeting. *Plos One* **7,** e30940–11 (2012).
6. Min, J.-J., Nguyen, V. H., Kim, H.-J., Hong, Y. & Choy, H. E. Quantitative bioluminescence imaging of tumor-targeting bacteria in living animals. *Nat Protoc* **3,** 629–636 (2008).
7. Francis, K. P. *et al.* Monitoring bioluminescent Staphylococcus aureus infections in living mice using a novel luxABCDE construct. *Infect. Immun.* **68,** 3594–3600 (2000).
8. Cronin, M. *et al.* High resolution *in vivo* bioluminescent imaging for the study of bacterial tumour targeting. *Plos One* **7,** e30940 (2012).
9. Hill, P. J. *et al.* Magnetic resonance imaging of tumors colonized with bacterial ferritin-expressing Escherichia coli. *Plos One* **6,** e25409 (2011).
10. Benoit, M. R. *et al.* Visualizing implanted tumors in mice with magnetic resonance imaging using magnetotactic bacteria. *Clin. Cancer Res.* **15,** 5170–5177 (2009).
11. Soghomonyan, S. A. *et al.* Positron emission tomography (PET) imaging of tumor-localized Salmonella expressing HSV1-TK. *Cancer Gene Ther.* **12,** 101–108 (2005).
12. Nedosekin, D. A. *et al.* Photoacoustic and photothermal detection of circulating tumor cells, bacteria and nanoparticles in cerebrospinal fluid *in vivo* and *ex vivo*. *Journal of* **6,** 523–533 (2013).
13. *In vitro* characterization of genetically expressed absorbing proteins using photoacoustic spectroscopy. *Biomed Opt Express* **4,** 2477 (2013).

14. Stritzker, J. *et al.* Vaccinia virus-mediated melanin production allows MR and optoacoustic deep tissue imaging and laser-induced thermotherapy of cancer. *Proceedings of the National Academy of Sciences* **110,** 3316–3320 (2013).
15. Paproski, R. J., Forbrich, A. E., Wachowicz, K., Hitt, M. M. & Zemp, R. J. Tyrosinase as a dual reporter gene for both photoacoustic and magnetic resonance imaging. *Biomed Opt Express* **2,** 771–780 (2011).
16. Malik, K., Tokkas, J. & Goyal, S. Microbial pigments: a review. *Int J Microbial Resour Technol* **1,** 361–365 (2012).
17. Balibar, C. J. & Walsh, C. T. *In vitro* biosynthesis of violacein from L-tryptophan by the enzymes VioA-E from Chromobacterium violaceum. *Biochemistry* **45,** 15444–15457 (2006).
18. Sánchez, C., Braña, A. F., Méndez, C. & Salas, J. A. Reevaluation of the violacein biosynthetic pathway and its relationship to indolocarbazole biosynthesis. *Chembiochem* **7,** 1231–1240 (2006).
19. Kodach, L. L. *et al.* Violacein synergistically increases 5-fluorouracil cytotoxicity, induces apoptosis and inhibits Akt-mediated signal transduction in human colorectal cancer cells. *Carcinogenesis* **27,** 508–516 (2006).
20. Melo, P. S., Justo, G. Z., de Azevedo, M. B. M., Durán, N. & Haun, M. Violacein and its beta-cyclodextrin complexes induce apoptosis and differentiation in HL60 cells. *Toxicology* **186,** 217–225 (2003).
21. Melo, P. S., Maria, S. S., Vidal, B. C., Haun, M. & Duran, N. Violacein cytotoxicity and induction of apoptosis in V79 cells. *In Vitro Cell. Dev. Biol. Anim.* **36,** 539–543 (2000).
22. Ferreira, C. V. *et al.* Molecular mechanism of violacein-mediated human leukemia cell death. *Blood* **104,** 1459–1464 (2004).
23. Razansky, D. *et al.* Multispectral opto-acoustic tomography of deep-seated fluorescent proteins *in vivo*. *Nature Photon* **3,** 412–417 (2009).
24. Stiel, A. C. *et al.* High-contrast imaging of reversibly switchable fluorescent proteins via temporally unmixed multispectral optoacoustic tomography. *Optics letters* **40,** 367–370 (2015).
25. Estrada, H., Turner, J., Kneipp, M. & Razansky, D. Real-time optoacoustic brain microscopy with hybrid optical and acoustic resolution. *Laser Phys. Lett.* **11,** 045601 (2014).
26. Deán-Ben, X. L. & Razansky, D. Portable spherical array probe for volumetric real-time optoacoustic imaging at centimeter-scale depths. *Opt Express* **21,** 28062–28071 (2013).
27. Cho, J. S. *et al.* Noninvasive *in vivo* imaging to evaluate immune responses and antimicrobial therapy against Staphylococcus aureus and USA300 MRSA skin infections. *J Invest Dermatol* **131,** 907–915 (2011).
28. Gonzalez, R. J., Weening, E. H., Frothingham, R., Sempowski, G. D. & Miller, V. L. Bioluminescence imaging to track bacterial dissemination of Yersinia pestis using different routes of infection in mice. *BMC Microbiol.* **12,** 147 (2012).
29. Leanti La Rosa, S. *et al. In vivo* assessment of growth and virulence gene expression during commensal and pathogenic lifestyles of luxABCDE-tagged Enterococcus faecalis strains in murine gastrointestinal and intravenous infection models. *Appl. Environ. Microbiol.* **79,** 3986–3997 (2013).
30. Yu, Y. A. *et al.* Visualization of tumors and metastases in live animals with bacteria and vaccinia virus encoding light-emitting proteins. *Nat. Biotechnol.* **22,** 313–320 (2004).
31. Filonov, G. S. *et al.* Bright and stable near-infrared fluorescent protein for *in vivo* imaging. *Nat. Biotechnol.* **29,** 757–761 (2011).
32. Belkin, S. Microbial whole-cell sensing systems of environmental pollutants. *Curr. Opin. Microbiol.* **6,** 206–212 (2003).
33. Forbes, N. S. Engineering the perfect (bacterial) cancer therapy. *Nat. Rev. Cancer* **10,** 785–794 (2010).
34. Deán-Ben, X. L., Buehler, A., Ntziachristos, V. & Razansky, D. Accurate model-based reconstruction algorithm for three-dimensional optoacoustic tomography. *IEEE Trans Med Imaging* **31,** 1922–1928 (2012).

Acknowledgement

G.G.W. thanks Antonella Lauri for her careful reading of the manuscript. We thank Dominik Soliman, Mathias Schwarz and Murad Omar for help with *in vivo* imaging, Panagiotis Symvoulidis for help with data visualization, Sukanya Arcot Kannabiran for help with the cell viability assay, Ronny Milde and Admar Verschoor for providing the protocol and the opsonizing reagent for bacterial detection as well as Uwe Klemm and Florian Jurgeleit for animal care taking and cryomicrotome imaging. G.G.W. acknowledges support from Technische Universität München, the Helmholtz Association of German Research Centers, Helmholtz Alliance ICEMED and the European Research Council under grant agreement ERC-2012-StG- 311552.

Author Contributions

Y.J. performed the optoacoustic and photophysical measurements and analyzed *in vivo* data, F.S. designed and performed the molecular biology experiments, J.R. supervised the *in vivo* experiments, conducted the cell viability experiments and tumor xenotransplantation performed by S.G., X.L.D. performed and analyzed *in vivo* data, M.K., H.E., D.R. generated the optoacoustic microscopy images, V. N. conceived and designed the *in vivo* experiments, G.G.W. conceived and designed the experiments, conducted the optoacoustic measurements, analyzed the data and wrote the manuscript.

Additional Information

Supplementary information accompanies this paper at http://www.nature.com/srep

Competing financial interests: The authors declare no competing financial interests.

How to cite this article: Jiang, Y. *et al.* Violacein as a genetically-controlled, enzymatically amplified and photobleaching-resistant chromophore for optoacoustic bacterial imaging. *Sci. Rep.* **5**, 11048; doi: 10.1038/srep11048 (2015).

5 Discussion

5.1 Encapsulins as bio-orthogonal programmable compartments in mammalian systems

In this dissertation, it was comprehensively shown that encapsulins of the *Myxococcus xanthus* can be expressed in mammalian cells as well as in rodent models where they auto-assemble into 32 nm diameter semi-permeable nano-compartments that can load its endogenous cargo proteins as well as engineered cargo proteins. Furthermore, we show a proof-of-principle that even multi-component processes can be programmed to occur inside the encapsulin lumen by targeting a split luciferase inside to the compartment. Thus, we demonstrate that we can mimic the fundamental biological principle of compartmentalization that occurs in mammalian systems in membrane-enclosed organelles by employing a low-complexity genetic system that only requires few proteinaceous components and by delivering the respective genetic information, we install a bio-orthogonal nano-organelle into mammalian cells.

5.1.1 Structural features and derived capabilities

5.1.1.1 Protein termini of the encapsulin shell monomer

Besides targeting of foreign proteins inside the encapsulin lumen, it was shown that the monomer MxEncA that auto-assembles into the hollow shell, can also be modified on both its termini. We show that the inward facing N-terminus can be modified with peptides up to 25 amino acids (as in the case of appended Mms peptides) without compromising its ability to self-assemble. This might be relevant to attach other accessory proteins or peptides required for a desired encapsulated process. For instance, it is conceivable to install one part of a coiled-coil pair to create another orthogonal way for cargo-targeting inside mammalian cells. Furthermore, other peptides that can act as proton sponges or other metal-binding motifs might be inserted for different applications.

Similarly, it was shown that the outward facing C-terminus of the shell could be modified with affinity tags up to 29 amino acids in length as in the case of the Twin-StrepTag affinity epitope. This is a major capability that allows for attaching other targeting moieties that can be exploited for intracellular targeting, e.g. to cellular membranes via a C-terminal farnesylation signal or to other sub-cellular compartments such as the peroxisome via a terminal peroxisomal targeting sequence (PTS). Similarly, the C-terminus can be modified to attach targeting peptides for extracellular targeting of encapsulins in the context of therapeutic applications, which has already been shown by attaching

a tumor-targeting peptide [148], or cell-to-cell communication settings. With regards to other structural regions of the encapsulin shell monomer, the external loops regions might also be modified with short peptides for targeting and might work in parallel with a C-terminally appended peptide to increase the specificity of cellular targeting.

5.1.1.2 Putative pore region

The encapsulin of *M.xanthus* has a putative pore region at its five-fold axis, where entry of iron ions most likely takes place [138]. For the encapsulin of *T.maritima*, it was shown that the pore region is rather small and has a diameter between 3 and 4 Å, which can be limiting when the entry of larger substrates than molecular irons is desired [136]. Thus, protein engineering schemes to either enlarge or shrink the pore regions to selectively filter for desired incoming substrates or prevent the exit of products might be applied.

5.1.1.3 Icosahedral symmetry and derived size

The encapsulin of *M.xanthus* consists of 180 identical subunits and has an icosahedral T=3 symmetry yielding an external diameter of around $\sim$ 32 nm with an internal diameter of $\sim$ 28 nm. The resulting volume can accommodate hundreds of endogenous cargo proteins as well as around 30,000 iron atoms at the same time on average [138]. Considering non-endogenous cargo molecules, we have shown that the *M.xanthus* encapsulin system can load up to around $\sim$ 60 molecules of an engineered fluorescent cargo protein fused to a degron (DD-mEos4b-EncSig). If larger encapsulins with the same capabilities are desired, genome mining for encapsulins of icosahedral symmetry with larger triangulation numbers might be applied.

It has been shown that the encapsulin of *M.xanthus* shell monomer has a HK97-like fold albeit there is only a minimal sequence homology. HK97, a bacteriophage of T=7 icosahedral symmetry at a 48 nm diameter, comprises a delta-domain hypothesized to be a scaffolding domain that is present in all phage capsids with triangulation numbers larger than T=7 [174]. Thus, it might be possible to create a chimeric protein consisting of MxEncA and the HK97 gp5 delta-domain, which could yield larger *M.xanthus* encapsulins of T=7 icosahedral symmetry.

Larger capsids might be particularly desired when considering the bio-mineralization of larger amounts of iron, necessary in magnetogenetic approaches, where an encapsulin would be tethered to a force-sensitive ion channel. Also, larger volumes might be desired when multi-enzyme cascades are supposed to be targeted to the encapsulin lumen, and many components are required.

5.1.1.4 Cargo protein targeting into the encapsulin lumen

It was previously demonstrated that interior the *M.xanthus* encapsulin shell is decorated with its three cargo proteins EncB, C and D that all share a short conserved

C-terminal extension, likely to be the targeting moiety docking inside a hydrophobic pocket on the encapsulin shell. Structural data of the *T.maritma* encapsulin system predicts a good fit of the C-terminal extension of its ferritin-like cargo and a hydrophobic pocket on the inside of the shell [136].

We and others have shown that this short C-terminal signal (EncSig) can be appended to other guest proteins, which are robustly targeted to the encapsulin lumen. The targeting of foreign proteins via the EncSig worked for all proteins tested in our study and can thus be considered generalizable. This is an important feature when considering to create customized cellular nano-reactors that require the presence of multiple enzymes inside the encapsulin lumen.

Interestingly, the C-terminal targeting peptides sequences of cargo proteins from encapsulin systems of different species show strong conservation and thus targeting of cargo might not be fully orthogonal [136, 137]. This possibility might be highly relevant in cases where two different encapsulin system are supposed to be installed in mammalian cells, where each of the encapsulin shells should strictly host a defined set of proteins. Since the C-terminal targeting peptides are quite conserved, certain promiscuity might occur.

In order to overcome this potential limitation and to find orthogonal pairs of shells and encapsulation signals, a directed co-evolution scheme might be applied to the pocket forming region of the shell and the encapsulation signal. In this setting, the cargo protein could be fluorescent protein N-terminally modified with a degron that will cause its rapid proteasomal degradation, if cargo auto-targeting into the corresponding shell does not occur, as demonstrated in the main publication Sigmund *et al.*, 2018 [1]. If carried out in *E.coli*, the selection for mutagenized fitting shell-encapsulation signal pairs could be implemented as a simple fluorescence read-out on agar plates. Another approach for fully orthogonal cargo-targeting into the encapsulin lumen could be based on the formation of covalent iso-peptid bonds of shell and cargo via SpyTag-SpyCatcher chemistry [175]. This principle has already been applied to the MS2 phage capsid, where different cargo proteins were targeted into the capsid lumen via the SpyTag-SpyCatcher system [176]. Recently, another iso-peptide bond forming pair of proteins domains orthogonal to the SpyTag-SpyCatcher system designated SnoopTag-SnoopCatcher system has been reported [177] and expands the toolbox for generation of fully orthogonal encapsulin-cargo systems. Another approach for creating fully orthogonal cargo-encapsulin shell pairs could be based on the recently introduced orthogonal coiled-coil (CC) helix pairs [178, 179, 180]. In this case, one half of the CC pair could be fused to N-terminus of the encapsulin shell-forming protein, whereas the other half would replace the encapsulation signal on the C-terminus of the cargo protein. This approach offers a lot of flexibility since many *de novo* designed CC pairs are currently available including variants that form homodimers or heterodimers.

5.1.1.5 Geometrical assembly of cargo proteins inside encapsulins

As stated above, the cargo proteins are docked into a hydrophobic pocket via its C-terminal extension. Moreover, there are reports showing that the ferritin-like cargo proteins of *R.rumbrum* form a decamer of five-fold symmetry that based on a molecular model can fit into the five-fold axis of the *T.maritima* encapsulin shell, placing it directly below the putative pore region [139]. According to this model, it is likely that the decameric ring would represent a 'gate-keeper' sitting directly below the pore immediately oxidizing entering ferrous iron. Other reports are surfacing claiming that this five-fold superstructure, that is already formed without a scaffolding function of the encapsulin shell, is a conserved motif for ferritin-like encapsulin cargo proteins, that might be conserved also in encapsulin systems with triangulation numbers above one.

If the model can be confirmed, this detail might be relevant when trying to create a customized enzymatic nano-reactor based on a certain set of enzymes. Then it would advisable to choose enzymes that fulfill the desired function that already endogenously adopt a five-fold quaternary structure. Also, when the fivefold symmetry adopting enzyme would be catalyzing the first step in the enzymatic cascade, it would be logical to place the assembly directly at the pore region, which could result in a desired substrate channeling effect [181]. Conversely, the finding would be valuable, when trying to install encapsulin-derived ferroxidases into bottom up-designed mega-dalton protein containers with tailor-made properties, which have been pioneered in the Baker laboratory [170, 171].

5.1.2 Encapsulins as gene reporters in molecular imaging

Since we comprehensibly established that bacterial encapsulins expression, assembly and cargo-loading of endogenous iron-mineralizing cargo proteins as well engineered cargo is feasible in mammalian cells without toxic side effects, we further explored their applicability as gene reporters for the imaging modalities covered in the following chapters.

5.1.2.1 Eukaryotically expressed encapsulins as MR reporters

McHughs et al., proved that the *M.xanthus* encapsulin system is actually a bacterial mega iron store under oxidative stress conditions that can mineralize up to 30,000 iron atoms, which is about ten times more than mammalian ferritin can store. We translated this knowledge to mammalian cells and showed that encapsulin iron loading is also feasible in mammalian cells when extra iron is supplemented, and iron uptake is boosted via the divalent metal ion uptake mediator Zip14 [182]. When we conducted relaxometry of cell pellets expressing *M.xanthus* with or without the iron-mineralizing cargo proteins, we found significantly elevated R_2* values for the cells expressing the whole set of encapsulin proteins including the iron-mineralizing proteins, indicating the bio-mineralized iron in encapsulins has magnetic properties enhancing MR contrast. In this respect, it

might be interesting to compare the performance of the *M.xanthus* encapsulin system to existing genetic MR reporters based on ferritin [52, 54, 58]. Furthermore, molecular relaxation rates of purified and iron-loaded encapsulins should be determined.

In the present main study, effective iron-loading of the *M.xanthus* encapsulin necessitated supplementation of extra ferrous iron in the cell culture medium. This indicates that iron-loading in this encapsulin system only occurs at high external ferrous iron concentrations or when exposed to oxidative stress conditions, which is in line with McHughs *et al.*, 2014 [138]. Therefore, it is likely that the *M.xanthus* encapsulin does not represent an effective iron sink, that would yield automatic up-regulation of iron uptake in mammalian cells, which would be a requirement for a fully-genetic effective *in vivo* gene reporter for MRI. Thus, it would be advisable to screen for other encapsulin systems that might have a higher affinity towards iron and more effective oxidation. It was hypothesized that several firmicutal bacteria that were shown to not possess canonical ferritin genes have encapsulins as their sole iron storage compartment [137]. Thus, it would be interesting to test their iron-loading and mineralizing performance in the context of mammalian cells and what influence they might have on existing components of the mammalian iron homeostasis. If such encapsulins would prove to be more effective in iron-mineralization and would represent an actual iron sink, it would be particularly interesting to test such system in rodent models for its performance in *in vivo* MR studies.

Little is known about the exact iron species that McHughs *et al.*, found in the *M.xanthus* encapsulin system, but the authors speculate that the iron mineral phase is poorly crystalline and consists of small granules. Thus, it is conceivable that the iron is stored as poorly magnetic ferrihydrite as in mammalian ferritins. Thus, detailed iron mineral phase characterization of bulk material should be carried out in the future with common methods such as high-resolution transmission electron microscopy (HRTEM), X-ray based methods, vibrating sample magnetometry (VSM), superconducting quantum interference device (SQUID) measurements, Raman microscopy or Mössbauer spectroscopy.

In order to generate more magnetic iron minerals inside the encapsulin lumen such as magnetite or maghemite that would result in much better MR contrast, we appended peptides derived from magnetotactic bacteria proteins (Mms6 and 7), that are implicated in aiding redox control and magnetite templating during magnetosome formation [183, 184, 185], to the N-terminus of *M.xanthus* encapsulin shell and to the N and C-terminus of the cargo proteins MxEncB and C. Using BN-PAGE, we evaluated effects on iron loading and found that none of the modified encapsulins proteins had beneficial effects on iron-loading based on our analysis but notably none of them impaired the iron-mineralizing function. Since we have not yet conducted an in-depth analysis of the resulting mineral phases, it would be advisable to do an in-depth characterization to evaluate if the addition of such Mms protein-derived peptides will yield an improved MR contrast as it has been shown for Mms6 when appended to the C-terminus of

murine ferritin [186]. Chapter **5.1.6.1** will cover potential strategies for generating hyper-magnetic encapsulins in greater detail.

5.1.2.2 Other strategies for generating MR contrast using encapsulins

As described above, bio-mineralized iron inside the encapsulin lumen can generate MR contrast. However, the bio-availability of iron is low, and it has a relatively large intrinsic toxicity based on the Fenton reaction, which yields highly reactive species that can peroxidize cellular membranes [187]. Thus, other contrast generating mechanisms that can be compartmentalized inside encapsulins can be envisioned. For instance, it has been shown that the manganese ions can generate MR contrast, which has been introduced over two decades ago [188]. In Manganese-enhanced magnetic resonance imaging (MEMRI) paramagnetic manganese ions can generate substantial MR contrast by modulating the T_2 relaxation of surrounding water protons [189]. Interestingly, MEMRI has been applied in neuroscience for neuronal mapping during acoustic stimulation since manganese enters neurons via the same ion channels that conduct calcium ions during neuronal firing [190].

However, manganese also exhibits severe cellular toxicity and thus limits its potential applications. Thus, it would be desirable to mineralize manganese oxides inside the encapsulin lumen. This could be achieved by targeting bacterial protein complexes that were shown to bio-mineralize manganese at neutral pH such as the MNX complex of *Bacillus sp.* PL-12 into encapsulins [191]. A similar system has already been implemented by targeting a manganese peroxidase (MnP) into vault nanoparticles as an effective platform for pollutant biodegradation [168].

Similarly, other magnetic elements such as nickel and cobalt could be sequestered non-toxically inside encapsulins by decorating the inside of encapsulins with cobalt or nickel binding peptides [192, 193, 194]. With regards to hyperpolarized xenon MRI, encapsulins could be equipped with proteins that have a hydrophobic cavity enabling xenon binding such as urate oxidase and serve as a multidentate bio-molecular scaffold [195, 196]. Interestingly, such hyperpolarized xenon MRI has already been shown using bacterial gas vesicles [68].

5.1.3 Electron microscopy (EM)

The encapsulin shell monomer of *M.xanthus* auto-assembles into 32 nm diameter proteinaceous nanospheres that were shown to possess electron dense iron-mineral cores, as shown by single particle cryoEM, when they were purified from their organism of origin [138]. We have successfully translated this knowledge to mammalian cells and demonstrated that encapsulins can be robustly detected in mammalian cells via *in situ* cryoEM and that bio-mineralized iron inside the encapsulin lumen affords extra contrast [1]. Thus, encapsulins represent a superior class of EM gene reporters based on its larger size and additional iron-derived contrast. However, under cryoEM conditions, the iron

contrast is not essential for detection and thus represents an advantage over existing ferritin based EM reporters, that require the addition of extra iron to the biological system [197, 58, 198]. Since *in situ* cryoEM is a high-end method and availability of the necessary machinery is still sparse, it would be interesting to evaluate if eukaryotically-expressed iron-loaded and non-iron loaded encapsulins can be detected in routine TEM from plastic-embedded sections.

5.1.3.1 Multiplexed EM detection of encapsulins to report cellular identities and states

Furthermore, it would be valuable to introduce encapsulins of defined sizes from other bacterial species that would allow for multiplexed encapsulin detection. Then, it would also be possible to encode several different states by combining differently sized encapsulins at different densities. Another 'channel' or 'color' could be the state of electron density in the core, that could be controlled by either supplying extra iron or by expressing or omitting the genes required for mineralization. The generation of different 'colors' could also be empowered by recombinase-driven stochastic choice expression of differently sized encapsulins as it has been shown in the Brainbow system for fluorescent proteins [199, 200]. Another way of encoding 'color' using encapsulins would be to genetically target them to sub-cellular locations such as the cellular membranes via a C-terminal farnesylation signal [201], to the peroxisomes via a C-terminal peroxisomal targeting sequence (PTS), to the mitochondria via a mitochondrial targeting sequence (MTS) or to the cellular nucleus via a canonical nuclear targeting signal (NLS). With regards to reporting cellular identity on the EM scale, it would probably most interesting to generate detectable cellular EM barcodes by spatially patterning differently sized encapsulins inside a certain cell of interest. This could be achieved by connecting them via a SpyTag-SpyCatcher-based system, via orthogonal coiled-coil pairs or other bio-molecular scaffolds. Such an EM barcoding system would be particularly valuable for brain connectomics research, where it is necessary to show all connections of a certain cell in the context of a whole brain [202]. To detect and classify a particular cell type based on the encapsulin patterns or states envisioned above, it would be desirable to implement a machine-learning aided image classification pipeline to be able to cope with large data-sets [203, 204].

Besides reporting a cellular identity using encapsulins, it would certainly be very interesting to report on cellular analytes such as calcium or the neurotransmitter dopamine aided by encapsulin-based EM sensors. In order to generate an EM calcium sensor as a proxy for neuronal activity, it would be conceivable to generate an aggregation based sensor by attaching a calmodulin-binding peptide [205, 206], that binds an engineered multidentate version of calmodulin leading to measurable aggregation when elevated levels of calcium are present in a cell shortly after neuronal firing. This principle might be generalizable to other analytes if bi-molecular protein domains are described that lead to an interaction when the respective analyte is present.

However, such clustering of encapsulins might be difficult to detect in the densely crowded environment of a neuron, especially when looking at neuronal projections. Thus, another possibility would be to decorate the interior of the encapsulin with a single protein domain, which considerably changes its conformation upon binding of an analyte yielding a shapeshift of the internal encapsulin region that can be detected by TEM. For instance, a Troponin C domain [207, 208], as employed in the genetically-encodable fluorescence-based 'Twitch' calcium sensors, could be targeted into the encapsulin lumen via the transferable encapsulation signal. With respect to a genetically-encoded calcium sensor for EM-based on encapsulins, the C-terminus of the encapsulin could also be fused to a domain that depending on calcium occupation unfolds a farnesyl moiety and consequently re-locates the encapsulin to the plasma membrane [209].

5.1.3.2 Other contrast generating mechanisms in encapsulins for EM applications

Besides the mere electron densities from the protein shell and the extra electron densities derived from the mineralized iron core, there could be other possibly superior contrast generating mechanism with regards to EM applications.

As shown in Sigmund *et al.*, 2018, 3,3'-diaminobenzidine (DAB) can be polymerized inside the encapsulin lumen, which was achieved by targeting the engineered peroxidase APEX2 [78] into the encapsulin. Since DAB polymers are known to be osmiophilic, extra contrast from encapsulins that contain DAB polymers is to be expected. Similarly, we have shown that melanin polymers can be produced inside the encapsulin lumen by targeting a bacterial tyrosinase. Thus, extra contrast might arise from uranyl ions binding to the melanin polymer, when uranyl acetate counter-stains are utilized [210]. Moreover, a passive accumulation of uranyl ions inside the encapsulin lumen could also be achieved by fusing an engineered high-affinity uranyl binding protein (SUP) [211, 212] to the shell protein or by targeting it to the lumen via an encapsulation peptide tag. This system could also be enhanced by producing a multidentate version of SUP by combining it with SpyTag-SpyCatcher chemistry [213]. Likewise, lead-binding proteins such as delta-aminolevulinic acid dehydratase (ALAD) [214] could be targeted to encapsulins either as cargo or as a genetic fusion with the shell, when lead-citrate counter-stains are used. Furthermore, it is conceivable that farnesylated membrane-trafficked encapsulins could enhance contrast since their fatty acid modification might be osmiophilic as the cellular membranes. Another approach to bait commonly used EM counter-stains inside the encapsulin would be to equip its interior with an RNA-binding protein such as Poly (A) binding proteins [215] or a Cas13b [216] variant that would catch RNA molecules that would attract uranyl ions via its negatively charged phosphates. However, trapping RNA transcripts required for protein translational inside the encapsulin lumen might lead to toxic side effects, and thus the aforementioned approaches for attracting commonly used EM stains are more promising.

These approaches could be particularly interesting since they would enable the robust detection of encapsulins of well-defined sizes without any extra preparation steps as it is necessary when utilizing peroxidases such as APEX2 as EM-tags.

5.1.3.3 Possible limitations for EM applications

Encapsulins expressed in mammalian cells can be robustly detected in *in situ* cryoEM via their sphericity, size and extra iron-derived densities inside their core and thus can robustly label a cell and thereby report a cellular identity. However, some researchers also employ EM to study protein dynamics of certain protein complexes. In fluorescence imaging, GFP-like proteins were shown to be functional in all kinds of fusion to cellular proteins, allowing researchers to study their dynamics. However, this is enabled by the monomeric nature of these engineered GFP-like proteins and their relatively small size. In contrast, fusing the encapsulin shell to a cellular protein of interest will most likely not report on its dynamic since the Enc monomer is driven by auto-assembly. Also, in T=3 encapsulins the shell monomer occupies three possible positions in the shell and thus fusing larger proteins onto the outside might not be feasible based on geometrical reasons and size constraints. A possible workaround for reporting other proteins dynamics and localization in EM using encapsulins might be to use smaller affinity peptides or single chain antibodies [217], which are still tolerated as C-terminal external fusions on the encapsulin shell, that target the protein of interest inside cells.

5.1.4 Optoacoustic imaging

Melanin is a dark pigment with an absorbance spectrum extending into the near-infrared range that is formed in tissue from the precursor L-tyrosine. It generates intrinsic contrast that can be picked up by optoacoustic imaging. However, it has been demonstrated that Tyrosinase, the enzyme catalyzing the rate-limiting steps in melanin synthesis, can be transferred to other cell types that usually don not produce melanin and thus serve as a reporter gene for OA imaging [33]. However, when not stored in a specialized organelle called 'melanosome', melanin exhibits severe cellular toxicity [218, 219].

In motivation to upgrade tyrosinase into a OA gene reporter that can be used without toxic side effects in all cell types, we created genetically engineered 'nano-melanosomes' in mammalian cells by targeting a bacterial tyrosinase into the lumen of the *M.xanthus* encapsulin shell by fusing it to the native cargo protein MxEncD [1] thereby ameliorating some of the inflicted toxicity. The residual toxic effects that remain are likely to be caused by quinone intermediates leaking out through the pores again. A possibility to improve that aspect would be to engineer pores such that they impose a higher selectivity for quinones. By decreasing the pore sizes, it might be feasible to increase the mean residence time of oxidative intermediates such that the polymerization occurs more quickly and thus traps the large melanin polymer inside the encapsulins.

Since the encapsulins represent a platform for concentrating enzymes and reactants reaching higher local concentrations than in the bulk solution, other absorbing small molecules or polymers might be created inside the encapsulin lumen by targeting the enzymes required for their synthesis. For instance, the enzymes that catalyze the turnover of L-tryptophane to the absorbing small molecule 'Violacein' that were shown to be transferable to *E.coli* for optoacoustic detection as shown in Jiang, Sigmund *et al.*, 2015 could be targeted to the encapsulin lumen for more effective synthesis. However, optoacoustic imaging is optimized for using far-red or near-infrared probes and thus bacterial phytochrome-based fluorescent proteins are a promising class for gene reporters for OA imaging. However, they require phycocyanobilin as a co-factor that is not available in mammalian cells at sufficient levels. Thus, it might be feasible to target all genes required for effective phycocyanobilin synthesis into the encapsulin lumen in mammalian cells. Reconstruction of phycocyanobilin synthesis pathways by employing bacterial genes has already been accomplished by targeting the necessary genes into mitochondria [220, 221]. However, this targeting might disrupt mitochondrial function and targeting to encapsulins might represent an alternative approach enabling the usage of bacterial phytochromes as OA gene reporters.

5.1.4.1 Genetic sensors for OA based on encapsulins

To date, few responsive genetic tools for optoacoustic imaging are available [32]. Recently, a novel approach based on pigment aggregation upon external stimuli in frog melanophores has been introduced [222]. In this system, the aggregation of melanosomes leads to an increase in optoacoustic amplitude and to a discernible shift in frequency that can be detected using OA. This concept could be generalized when combining our bioengineered 'nano-melanosomes' with the general aggregation based strategy as described above.

5.1.5 Other applications in molecular imaging: Optical nanoscopy, encapsulated GCaMP, fiducial markers

Eukaryotically expressed encapsulins are a generalizable platform for molecular imaging across scales. Besides the aforementioned applications and concepts, there are several other niche applications that could be empowered by encapsulin expression in mammalian cells.

For instance, *in situ* cryoEM of vitrified cells is a powerful tool to study protein interactions in their cellular environment at nanometer resolution [223]. However, alignment of tilt-series may be aided by fiducial markers such as synthetic gold particles [224]. Thus, iron-filled electron dense encapsulins, that are evenly distributed throughout the cells could potentially serve as fully-genetic fiducial markers that don not require any additional preparation steps.

Similarly, in super-resolution optical techniques such as Photoactivated Localization Microscopy (PALM), stage drift can also be corrected using fiducial markers such as synthetic gold nanoparticles [225] that could be replaced by genetically encoded encapsulins that are filled with photoswitchable proteins such as mEos4b [226, 1]. Moreover, PALM has been shown to be able to resolve HIV-1 particles [227] that are in a similar size range as encapsulins. Thus, it might be possible to spatially pattern encapsulins of different sizes that are loaded with different switchable fluorescent proteins in order to label cells with a bar-code that might be de-codable using optical nanoscopy.

Calcium imaging using single component genetically-encoded calcium indicators such as GCaMP have revolutionized neuroscience by allowing for interrogation of neuronal activity on a single cell level in living animals [228]. However, concerns have arisen that the calmodulin domain in GCaMP can interfere with the gating of calcium conducting ion channels [213]. Thus, GCaMP could be encapsulated inside the encapsulin lumen by appending an encapsulation signal and thereby de-coupling it from any other cytosolic protein that is mediated by calmodulin.

5.1.6 Magnetic properties of encapsulins in the context of mammalian cells

Informed by the general motivation to create superior 'magnetogenetic' tools, the encapsulin system of *M.xanthus* was chosen to be expressed in mammalian cells. We comprehensively showed that iron loading of encapsulins in mammalian cells is feasible and that they can thus generate contrasts in different molecular imaging modalities across different scales. However, the ultimate goal of 'magnetogenetics' is to not only read-out information but also manipulate biological systems non-invasively based on the genetic modification and magnetic fields. In terms of manipulation via magnetic gradients, we have shown that HEK293T cells expressing iron-loaded encapsulins can be robustly sorted at modest rates using magnetic columns [1]. Although these sorting rates for encapsulin-expressing cells could undoubtedly still be improved, they represent a major step forward towards magnetically-controllable cells. Furthermore, we found that we could sort significantly more encapsulin-expressing cells than H-chain ferritin (HHF) expressing cells, which is notable since it has previously been reported that ferritin over-expressing cells can be sorted using magnetic gradients [229], which we were not able to reproduce in our sorting system. Besides the mere capability to move around hyper-magnetic cells, future studies need to clarify if ionic currents can also be elicited by targeting encapsulins to cellular membranes, tether them to force or thermo-sensitive ion channels and by exposing them to magnetic gradients or RF-magnetic fields.

In order to evaluate their potential as magnetogenetic actuators, a full-on characterization of the magnetic properties of encapsulins needs to be conducted in the future. In order to characterize the type of iron phase and the resulting magnetic moment of individual encapsulins, methods such as Vibrating Sample Magnetometery (VSM), magnetometry using a Superconducting Quantum Interference Device (SQUID), Ferromagnetic Resonance Spectroscopy (FMR), Mössbauer spectroscopy and bulk MR measurements

will be helpful. However, the current state of knowledge about iron-mineralizing encapsulin systems indicates that the iron phase is most likely also the weakly magnetic ferrihydrite since the oxidation mechanism is similar to canonical ferritins [139].

Markus Meister has published an article about whether currently published 'magnetogenetic' tools comply with basic laws of physics and he finds that all of the proposed working mechanism cannot explain the observed effects and are off by several orders of magnitude [125]. This begs the question if eukaryotically expressed encapsulins can move the field of magnetogenetic tools into a regime that is closer to what basic physics deems plausible. For instance, he notes that a ferritin complex pulling on a force-sensitive ion channel exerts a force that is 9 log units to small to cause channel opening [125]. If one assumes that the magnetic moment of a given protein particle loaded with ferrihydrite is linearly dependent on the number of iron atoms on the inside, a tethered encapsulin complex would be at least one log unit closer to complying with the laws of physics since the *M.xanthus* encapsulin contains on average 30,000 iron atoms [138], which is about 10 times more than canonical mammalian ferritins. However, he also pictures an example considering very strong fields, where the anisotropy of ferritin yields a strong enough torque that could generate measurable ionic currents across membranes when thousands of ion channels are actuated at the same time. Therefore, using encapsulins instead of ferritin moves that approach into an even more realistic regime. Moreover, patterning encapsulins into a linear shape, as envisioned in the previous chapters above, would increase its anisotropy and could benefit the proposed mechanism. Finally, Meister notes that if the genetically-encoded tools would yield bio-mineralized magnetite particles instead of ferrihydrite, as they are found in magnetotactic bacteria [230], they could generate much higher forces, torque or would generate more heat in RF magnetic fields and thus gaining a more realistic base of reason.

5.1.6.1 Molecular engineering of hyper-magnetic encapsulins

The calculations and the conclusion presented in the publication by Markus Meister summarized in the previous chapter demand genetic tools that yield bio-mineralized magnetite or at least an iron bio-mineral that is more magnetic than ferrihydrite. Since encapsulins have an inner cavity that could accommodate magnetite particles in the size range of 20 nm, that would have a permanent magnetic moment and offer the flexibility to co-target additional proteins or peptides that would aid the magnetite mineralization, they represent a promising platform to engineer a customized bio-nano-reactor for magnetite synthesis. We have previously attempted to modify the *M.xanthus* shell and cargo proteins MxB and C with peptides derived from the Mms 6 and 7 proteins from *Magnetospirillum magneticum* AMB-1 that were shown to control the shape of magnetite crystals and protect ferrous iron from oxidation [183]. Although we did not find any benefit in terms of iron loading [1] as judged by BN-PAGE analysis, there is the possibility that the resulting iron phase had already been altered. These encapsulin variants should be magnetically characterized as described above in future studies. Besides these templating peptides, there are other factors that determine if magnetite can

be formed. For instance, it has been demonstrated that co-precipitation of magnetite occurs at alkaline pH since ferrous iron precipitates at higher pH values [231]. Thus, it might be feasible to target enzymes into the encapsulin lumen, that consume protons and would yield a local increase in pH. For instance, the enzyme Urease, which belongs to the class of hydrolases, consumes protons while turning over urea to ammonia and CO_2 [232, 233]. Moreover, in order for magnetite to form, the ratio of ferrous to ferric iron needs to be 1 to 2, and thus redox potential needs to be tightly controlled as well. In order to supply enough ferrous for magnetite precipitation, targeted reductases might be helpful. In that respect, the redox-controlling cytochrome c-like protein MamP of *Magnetospirillum magneticum* AMB-1 could be targeted into the encapsulin lumen via an encapsulation signal to mediate the necessary iron redox state [183]. However, it is questionable if enough redox equivalents and enough substrate for the envisioned enzymatic reactions are available in the cytosol of a mammalian cell and if their passive diffusion into the encapsulin pores would be fast enough to locally sustain the required pH and redox conditions inside the encapsulin lumen. Despite the possible limitations described above, the generation of a 'low complexity-magnetosome' by equipping encapsulins with a reduced set of modules from the magnetosome gene repertoire seems like a realistic route to magnetite bio-mineralization in mammalian cells. According to a model, the mineral ferrihydrite that is formed inside mammalian ferritins and also most likely inside encapsulin is considered a precursor in the formation of magnetite inside magnetosomes as well as in magnetite chiton teeth [234, 235, 236, 237]. According to these models, a reductive transformation could occur that transmutes the ferrihydrite into magnetite. Thus, another viable approach might be to target ferric reductases to the encapsulin lumen, that would transform mineralized ferrihydrite to magnetite by gradually transmuting the surface of the ferrihydrite [238]. However, also in this hypothetical system, it remains unclear, whether enough redox equivalents are available and if they can enter the encapsulin pores fast enough. However, if such enzymes aiding to sustain pH and redox potential can be indeed targeted into the encapsulin lumen, *in vitro* synthesis can be performed, where co-factors and substrates can be added in desired quantities. In that way, it can be evaluated whether such a system could potentially work in a mammalian cell and establish a working concentration range.

Besides these rational approaches described above, directed evolution schemes might be applied to the encapsulin shell and cargo proteins with a subsequent magnetic selection for cells that contain hyper-magnetic variants. This approach has been already applied to the *P.furiosus* ferritin gene and has yielded hyper-magnetic variants featuring a higher loading factor [58, 59]. However, it might be advisable to conduct these directed evolution schemes already in mammalian cells employing dCas9 base-editor tools [239, 240] since screening in bacteria might yield variants that would only become hyper-magnetic in these organisms.

5.2 Potential applications of encapsulins in translational research

This thesis showed comprehensively that encapsulins of *M.xanthus* expressed in mammalian cells can serve as a gene reporter across different modalities and scales and enable manipulation of cells in magnetic gradients. Although these capabilities are currently restricted to basic research in pre-clinical models, several applications in translational research are conceivable.

5.2.1 Imaging of CAR-T cells using heterologously expressed encapsulins

CAR-T cells are a new class of cellular therapeutics that have been recently introduced and caused a small paradigm shift in the treatment of different types of difficult to treat cancers of the blood system. To create CAR-T cells, T-cells of a patient are collected from the patient's blood and genetically engineered so that the cells express a chimeric antigen receptor (CAR) that is presented on the cell surface and specifically targets tumor antigens [241]. In order to follow up on the bio-distribution and proliferation of CAR-T cells once re-injected into the patients, ways of labeling them for non-invasive imaging modalities such as PET or MRI are demanded [242].

Thus, in the future, CAR-T cells could be equipped with metal-mineralizing encapsulins for detection in MRI or melanin-producing encapsulins to empower non-invasive detection using optoacoustic imaging. Furthermore, it could be envisioned to install a genetically encoded secretion of encapsulins containing enzymatically-synthesized small molecules with anti-tumoral activity to enhance their therapeutic efficacy by delivering them to the tumor cells once recognized via the CAR. These secreted encapsulins could also carry an external tumor-targeting peptide, which would secure the specific targeting to the tumor cells as it has been previously demonstrated [148]. Finally, such secreted encapsulins could also be secreted into the bloodstream, sampling out cellular contents of the CAR-T cells and thereby report on cellular parameters and on their proliferation state. These secreted 'messages-in-a-bottle' could be then detected and read-out by pulling them out of the blood via C-terminally presented affinity tags such a FLAG or StrepTag-II epitope. Interestingly, the StrepTagII epitope has previously been engineered into CARs for purification and identification [243].

5.2.2 Encapsulins as drug delivery vehicles

More generally, therapeutic molecules, such as antibody fragments or even small molecules, could be en-caged in the encapsulin lumen and thereby be protected from degradation or prevent them from acting in non-targeted tissues. As described above, specific targeting could be achieved with tumor targeting peptides [148] or even small single chain antibody fragments targeting specific tumor antigens that could be attached to the external portion of the encapsulin shell. Once taken up by the targeted cell, lume-

nal contents could be set free via the acidic pH in the endocytotic vesicles [148]. Similar approaches have been demonstrated using *de novo* designed DNA origami-based containers [244, 245] but such vehicles might be prone to rapid degradation via nucleases. Furthermore, the cost for generation of larger amounts of such DNA-based vehicles has been a concern, but recently the Dietz laboratory has presented an approach for large-scale production of DNA origami at reasonable cost [246].

However, for these approaches to be applicable in translational research, it would be critical to characterize the immunogenicity of encapsulins.

5.3 Limitations of encapsulins as genetically-encoded tools in basic research and mammalian cell engineering

This dissertation alludes to several applications of genetically-encoded encapsulins in basic research and cell engineering in general but what are its limitations with respect to the gold standard of genetically-encoded tools for imaging, such as GFP-like proteins.

5.3.1 Encapsulins as a gene reporter for microscopy techniques

When considering microscopy techniques that aim to label sub-cellular structures, GFP-like proteins are extremely useful since they have been shown to work as fusions with different cellular proteins. Thus, they can report on the cellular localization and dynamics of endogenous proteins in many cases. Combined with optical nanoscopy techniques they even allow to resolve the topology of protein complexes consisting of several different proteins. In that regard, encapsulins will most likely not be able to compete with GFP-like proteins, since fusing monomers to cellular proteins will most likely disrupt the function of the cellular protein and the self-assembly of the encapsulin shells. In EM, researchers also demand tools that can report on the localization and dynamics of other cellular proteins and protein complexes. To this end, engineered monomeric peroxidase-based labels such as APEX that can be fused to the protein of interest [78] and ferritin fused to other cellular components has been shown to be functional in some cases [198]. It is questionable if encapsulins can compete with these techniques with respect to the functionality in protein fusions since the assembly of the *M.xanthus* encapsulin adopts a complex T=3 icosahedral symmetry and thus is more likely to be disrupted in fusions. Besides, the relatively large size of encapsulins in comparison to a single protein molecule inside the cell might create large artifacts when trying to use encapsulins as a proxy to report a precise localization. Despite these possible limitations, it might still be feasible to report on protein localization by either fusing short peptides or single chain antibodies to the encapsulin surface that target the protein of interest. Combined with the superior visibility due to size and iron-loading of encapsulins, it could be still be beneficial to use encapsulins instead of APEX or ferritin, especially

when considering that no extra steps in sample preparation are required.

Based on the concerns above, using encapsulins as cell identity markers especially with regards to connectomics research seems to be the more natural application. However, for connectomics research, it might be critical that expressed encapsulins reach the cellular projections of neurons. This might be limited due to the relatively large size of encapsulins with respect to the width of neuronal projections. If indeed encapsulins cannot reach projections passively, a strategy to overcome this limitation would be to fuse peptidic components of the axonal transport machinery [247] to the encapsulins surface and thereby possibly achieving active transport along axons and dendrites.

5.3.2 Encapsulins as a genetically-encoded bio-orthogonal 'nano-organelle'

Other groups heterologously expressed prokaryotic nano-compartments in yeast and designated them a 'synthetic' organelle [150]. However, this can be considered an overstatement since cellular organelles have many characteristics that are quite distinct from the proteinaceous encapsulins compartments. For instance, the mere size of organelles such as lysosomes enables the sequestration of millions of proteins whereas the relatively small encapsulins were shown to be able to accommodate only about 100 engineered cargo molecules [1]. In general, the larger capacity of cellular organelles allows for more complex reactions that require a larger number of different protein components. Furthermore, cellular organelles are membrane-enclosed, and thus there is basically no passive diffusion of reactants in and out of the organelle. In organelles, protein uptake and diffusion of ions have to be controlled by membrane proteins sitting in the organelle membrane. For, instance protein import into peroxisomes is mediated via a diverse set of so-called 'PEX' proteins [248]. Thus, turnover of molecules in and out of organelles is tightly controlled. In encapsulins, there is always a passive diffusion of reactants in and out of the compartment via the pore regions. Actual trapping of reaction products can thus be only achieved when the size of the product exceeds that of the pore region, which can be the case in polymerization reactions. It is probably difficult to engineer a selective import and export system into the proteinaceous encapsulin shell, and filtering can most likely only be achieved by increasing or decreasing pore sizes using molecular engineering. Thus, it seems to be difficult to sustain steep concentration gradients of protons or other molecular ions across the encapsulin shell. Despite these shortcomings with respect to membrane-enclosed organelles, encapsulins have the great benefit of forming an orthogonal semi-permeable compartment with just one protein component and thereby allowing synthetic biology researchers to create customized semi-permeable 'nano-organelles' with few components that can easily be genetically installed into the mammalian cell or tissue of interest.

5.3.3 Degradation and cellular interactions of encapsulins in mammalian cells

Although bacterial encapsulins are considered 'orthogonal' throughout this dissertation, related aspects of their expression in mammalian cells include their degradation and turn-over and possible un-predicted interactions with endogenous cellular machinery, which should be thoroughly addressed in future studies.

Although our toxicity studies did not show any adverse effects going beyond what the over-expression of fluorescent proteins cause, there might be more subtle alterations that might still be biology relevant. For instance, currently, it is not clear how encapsulins are being degraded in mammalian hosts. Because of their size, they are most likely not subjected to proteasomal degradation and are most likely degraded in the cellular lysosomes. This aspect can be studied in the future and also establish a half-life time of an encapsulin in the cytosol.

Furthermore, this dissertation has not yet addressed any possible other interactions with cellular machinery. For instance, native MS analysis of purified encapsulins from HEK293T cells revealed a phosphorylated serine residue in the external linker peptide [1]. Since phosphorylation is an important post-translational modification that is responsible for mediating many cell signaling pathways [249, 250] encapsulin phosphorylation should be studied in greater detail to evaluate possible consequences. If negative effects arise from this modification, the serine could also be replaced with another amino acid that cannot be phosphorylated. Likewise, encapsulins might also be glycosylated, which could be covered in future studies. Another aspect is the unspecific encapsulation of cytosolic proteins that might have an influence on cellular metabolism. This phenomenon might be also further characterized using native MS methods [251] in the future.

5.4 Gene reporters for OA based on enzymatically amplified chromophore generation

In Jiang, Sigmund et al., 2015 we have demonstrated that the enzymatically produced small molecule chromophore 'Violacein' can robustly be detected in optoacoustic imaging [2]. To that end, we genetically modified *E.coli* by introducing the Vio operon (*VioABCDE*) of *Chromobacterium violaceum* encoding the five enzymes responsible for the sequential turn-over of the amino acid L-tryptophane to Violacein. The strong production of Violacein in engineered *E.coli* enabled their *in vivo* detection in murine tumors in depths up to several mm using multi-spectral optoacoustic tomography.

5.4.1 Characteristics of Violacein and benefits over GFP-like reporters

Violacein has a peak absorption at about 600 nm and furthermore has substantial absorption at wavelengths extending into the near-infrared region. Besides, these ab-

sorption characteristics it is non-fluorescent and thus is expected to generate a strong optoacoustic signal. Furthermore, we found that Violacein is resistant to photobleaching, which is an important feature for optoacoustic probes since large doses of laser energy are typically used. This is a major advantage over GFP-based genetic reporters for OA imaging since most of them are typically prone to rapid photo-bleaching [26]. Another benefit of enzymatically produced chromophores is the enzymatic amplification effect since one enzyme molecule can turn-over many millions of substrate molecules and could potentially yield higher concentrations of absorbing molecules in comparison to GFP-like proteins. This effect has already been exploited previously in enzyme-based MRI reporters [44]. Interestingly, Violacein has been shown to possess cytotoxic effects in several tumor cell lines and could thus serve as a 'theranostic' tool in future studies. In such system, engineered bacteria would passively or actively enrich in tumors and could be detected using optoacoustic imaging and at the same time release Violacein for therapeutic intervention. With regards to its limitations, Violacein, when produced by the respective enzymes is not targeted and can thus not easily label sub-cellular structures. However, this might not be relevant in optoacoustic tomography applications because the resolution is too low to resolve sub-cellular structures. Another disadvantage is that the genes encoding VioABCDE combined require the transfer of much more genetic information than for a GFP-like protein and dependent on the model system might not be feasible.

5.4.2 Violacein as a reporter for OA imaging in mammalian cells

We have demonstrated that genetically-controlled Violacein generation can be utilized as a reporter for bacterial tumor imaging using optoacoustics. However, transferring the genes coding for VioABCDE into mammalian systems should also be feasible. In an attempt to produce Violacein in mammalian cells, we transfected plasmids coding for each of the Vio genes into HEK293T cells. However, we did not observe pigment formation. This could be due to several reasons: 1.) One or more of the bacterial proteins do not express in mammalian cells, or they lack a certain co-factor not readily available in mammalian cells. 2.) The enzymes required for the turnover are spatially separated and cannot execute the whole enzymatic cascade. 3.) The precursor L-tryptophane might not be abundant enough. 4.) The cells that actually do produce larger quantities of Violacein die off because of the toxic effects that are described for tumor cell lines [252, 253, 254]. In order to systematically approach the problem, a reasonable first step would be to tag all five proteins with different epitope tags, co-transfect all constructs and detect protein expression via western blotting. If all proteins can be detected using western blots, their localization should be monitored via immunocytochemistry.

5.4.2.1 Violacein synthesis in mammalian cells employing encapsulins

If the enzymes encoded by the Vio genes are indeed functionally expressed but spatially separated due to differential targeting, one approach to overcome this problem

would be to C-terminally append encapsulation signals to *VioABCDE* and thereby target them into the encapsulin lumen. Thereby, it would be expected that all the proteins required are in close proximity and thus the turn-over of L-tryptophane would be expected to be more efficient due to substrate channeling effects [181]. We have previously shown, that the amino acid L-tyrosine can cross the pores of the *M.xanthus* encapsulin and thus it is likely that L-tryptophane can also enter these pores. By sequestering Violacein inside the encapsulin lumen, it would furthermore plausible to assume that the cytotoxic effects, that have been described for cancer cell lines but might also apply to non-malignant cells, could be ameliorated.

5.4.3 Other absorbing pigments or natural polymers qualifying as OA probes

Violacein is a small molecule pigment with interesting optical and anti-tumoral properties that might empower theranostic approaches combining OA imaging for cancer detection and treatment. However, its optical properties are not ideal for OA imaging since its NIR absorption is quite low. Thus, other bleaching-resistant biological pigments or absorbing polymers, for which their biosynthetic pathways and the required enzymes for turn-over are well described, might serve as superior OA probes when installed into mammalian cells or bacteria.

For instance, the class of bacteriochlorophylls, produced in light harvesting photosynthetic bacteria, cover the spectral region between 700 and 1000 nm and thus would be ideal with regards to their absorption profile [255, 256, 257]. However, the biosynthetic routes to these molecules are quite complex and require many enzymes. Thus, it is questionable if it makes sense to re-create these pathways in other organisms. Furthermore, it is not clear if such bacteriochlorophylls are well-tolerated in mammalian cells. Another interesting pigment produced in the fungal species *Chlorociboria aeruginosa* and *Chlorociboria aeruginascens* called 'Xylindein' has a favorable absorption spectrum with two peaks around 630 and 700 nm and thus qualify as an ideal OA probe [258]. Unfortunately, to date, the exact biosynthetic route and the necessary enzymes for its synthesis are not fully described. Thus, it is currently not possible to re-create the bio-synthesis of Xylindein in heterologous hosts.

Bibliography

[1] F. Sigmund, C. Massner, P. Erdmann, A. Stelzl, H. Rolbieski, M. Desai, S. Bricault, T. P. Wörner, J. Snijder, A. Geerlof, H. Fuchs, M. Hrabě de Angelis, A. J. R. Heck, A. Jasanoff, V. Ntziachristos, J. Plitzko, and G. G. Westmeyer. Bacterial encapsulins as orthogonal compartments for mammalian cell engineering. *Nat. Commun.*, 9(1):1990, 2018. URL: https://doi.org/10.1038/s41467-018-04227-3, doi:10.1038/s41467-018-04227-3.

[2] Y. Jiang, F. Sigmund, J. Reber, X. Luís Deán-Ben, S. Glasl, M. Kneipp, H. Estrada, D. Razansky, V. Ntziachristos, and G. G. Westmeyer. Violacein as a genetically-controlled, enzymatically amplified and photobleaching-resistant chromophore for optoacoustic bacterial imaging. *Scientific Reports*, 5:11048 EP –, 2015. URL: https://doi.org/10.1038/srep11048, doi:10.1038/srep11048.

[3] M. Doubrovin, I. Serganova, P. Mayer-Kuckuk, V. Ponomarev, and R. G. Blasberg. Multimodality in vivo molecular-genetic imaging. *Bioconjug Chem*, 15(6):1376–1388, 2004. URL: https://www.ncbi.nlm.nih.gov/pubmed/15546205, doi:10.1021/bc0498572.

[4] H. Youn and J. K. Chung. Reporter gene imaging. *AJR Am J Roentgenol*, 201(2):W206–14, 2013. URL: https://www.ncbi.nlm.nih.gov/pubmed/23883235, doi:10.2214/AJR.13.10555.

[5] A. E. Palmer, Y. Qin, J. G. Park, and J. E. McCombs. Design and application of genetically encoded biosensors. *Trends in Biotechnology*, 29(3):144–152, 2011. URL: http://www.sciencedirect.com/science/article/pii/S0167779910002155, doi:10.1016/j.tibtech.2010.12.004.

[6] R. Y. Tsien. The green fluorescent protein. *Annual Review of Biochemistry*, 67(1):509–544, 1998. doi:10.1146/annurev.biochem.67.1.509.

[7] V. Ntziachristos. Fluorescence molecular imaging. *Annual Review of Biomedical Engineering*, 8(1):1–33, 2006. doi:10.1146/annurev.bioeng.8.061505.095831.

[8] O. Shimomura, F. H. Johnson, and Y. Saiga. Extraction, purification and properties of aequorin, a bioluminescent protein from the luminous hydromedusan, aequorea. *Journal of Cellular and Comparative Physiology*, 59(3):223–239, 1962. doi:10.1002/jcp.1030590302.

[9] D. C. Prasher, V. K. Eckenrode, W. W. Ward, F. G. Prendergast, and M. J. Cormier. Primary structure of the aequorea victoria green-fluorescent protein.

Gene, 111(2):229–233, 1992. URL: http://www.sciencedirect.com/science/article/pii/037811199290691H, doi:10.1016/0378-1119(92)90691-H.

[10] M. Chalfie, Y. Tu, G. Euskirchen, W. W. Ward, and D. C. Prasher. Green fluorescent protein as a marker for gene expression. *Science*, 263(5148):802, 1994. doi:10.1126/science.8303295.

[11] S. Inouye and F. I. Tsuji. Aequorea green fluorescent protein. *FEBS Letters*, 341(2-3):277–280, 1994. doi:10.1016/0014-5793(94)80472-9.

[12] A. B. Cubitt, R. Heim, S. R. Adams, A. E. Boyd, L. A. Gross, and R. Y. Tsien. Understanding, improving and using green fluorescent proteins. *Trends in Biochemical Sciences*, 20(11):448–455, 1995. URL: http://www.sciencedirect.com/science/article/pii/S0968000400890994, doi:10.1016/S0968-0004(00)89099-4.

[13] R. Heim, D. C. Prasher, and R. Y. Tsien. Wavelength mutations and posttranslational autoxidation of green fluorescent protein. *Proceedings of the National Academy of Sciences*, 91(26):12501, 1994. doi:10.1073/pnas.91.26.12501.

[14] G. Zhang, V. Gurtu, and S. R. Kain. An enhanced green fluorescent protein allows sensitive detection of gene transfer in mammalian cells. *Biochemical and Biophysical Research Communications*, 227(3):707–711, 1996. URL: http://www.sciencedirect.com/science/article/pii/S0006291X96915739, doi:10.1006/bbrc.1996.1573.

[15] R. Heim and R. Y. Tsien. Engineering green fluorescent protein for improved brightness, longer wavelengths and fluorescence resonance energy transfer. *Current Biology*, 6(2):178–182, 1996. URL: http://www.sciencedirect.com/science/article/pii/S0960982202004505, doi:10.1016/S0960-9822(02)00450-5.

[16] R. N. Day and M. W. Davidson. The fluorescent protein palette: tools for cellular imaging. *Chemical Society reviews*, 38(10):2887–2921, 2009. URL: https://www.ncbi.nlm.nih.gov/pubmed/19771335, doi:10.1039/b901966a.

[17] A. Germond, H. Fujita, T. Ichimura, and T. M. Watanabe. Design and development of genetically encoded fluorescent sensors to monitor intracellular chemical and physical parameters. *Biophysical reviews*, 8(2):121–138, 2016. URL: https://www.ncbi.nlm.nih.gov/pubmed/28510054, doi:10.1007/s12551-016-0195-9.

[18] J. Nakai, M. Ohkura, and K. Imoto. A high signal-to-noise ca2+ probe composed of a single green fluorescent protein. *Nature Biotechnology*, 19:137 EP –, 2001. URL: https://doi.org/10.1038/84397, doi:10.1038/84397.

[19] T.-W. Chen, T. J. Wardill, Y. Sun, S. R. Pulver, S. L. Renninger, A. Baohan, E. R. Schreiter, R. A. Kerr, M. B. Orger, V. Jayaraman, L. L. Looger, K. Svoboda, and D. S. Kim. Ultrasensitive fluorescent proteins for imaging neuronal activity. *Nature*,

499:295 EP –, 2013. URL: https://doi.org/10.1038/nature12354, doi:10.1038/nature12354.

[20] M. B. Ahrens, M. B. Orger, D. N. Robson, J. M. Li, and P. J. Keller. Whole-brain functional imaging at cellular resolution using light-sheet microscopy. *Nature Methods*, 10:413 EP –, 2013. URL: https://doi.org/10.1038/nmeth.2434, doi:10.1038/nmeth.2434.

[21] A. Taruttis and V. Ntziachristos. Advances in real-time multispectral optoacoustic imaging and its applications. *Nature Photonics*, 9:219 EP –, 2015. URL: http://dx.doi.org/10.1038/nphoton.2015.29, doi:10.1038/nphoton.2015.29.

[22] E. Herzog, A. Taruttis, N. Beziere, A. A. Lutich, D. Razansky, and V. Ntziachristos. Optical imaging of cancer heterogeneity with multispectral optoacoustic tomography. *Radiology*, 263(2):461–468, 2012. doi:10.1148/radiol.11111646.

[23] D. Razansky, M. Distel, C. Vinegoni, R. Ma, N. Perrimon, R. W. Köster, and V. Ntziachristos. Multispectral opto-acoustic tomography of deep-seated fluorescent proteins in vivo. *Nature Photonics*, 3:412 EP –, 2009. URL: http://dx.doi.org/10.1038/nphoton.2009.98, doi:10.1038/nphoton.2009.98.

[24] D. M. Shcherbakova, M. Baloban, and V. V. Verkhusha. Near-infrared fluorescent proteins engineered from bacterial phytochromes. *Curr. Opin. Chem. Biol.*, 27:52–63, 2015. URL: http://www.sciencedirect.com/science/article/pii/S136759311500068X, doi:10.1016/j.cbpa.2015.06.005.

[25] G. S. Filonov, K. D. Piatkevich, L.-M. Ting, J. Zhang, K. Kim, and V. V. Verkhusha. Bright and stable near-infrared fluorescent protein for in vivo imaging. *Nature Biotechnology*, 29:757 EP –, 2011. URL: http://dx.doi.org/10.1038/nbt.1918, doi:10.1038/nbt.1918.

[26] J. Laufer, A. Jathoul, M. Pule, and P. Beard. In vitro characterization of genetically expressed absorbing proteins using photoacoustic spectroscopy. *Biomedical Optics Express*, 4(11):2477–2490, 2013. doi:10.1364/BOE.4.002477.

[27] A. C. Stiel, X. L. Deán-Ben, Y. Jiang, V. Ntziachristos, D. Razansky, and G. G. Westmeyer. High-contrast imaging of reversibly switchable fluorescent proteins via temporally unmixed multispectral optoacoustic tomography. *Optics Letters*, 40(3):367–370, 2015. doi:10.1364/OL.40.000367.

[28] P. Vetschera, K. Mishra, J. P. Fuenzalida-Werner, A. Chmyrov, V. Ntziachristos, and A. C. Stiel. Characterization of reversibly switchable fluorescent proteins in optoacoustic imaging. *Analytical Chemistry*, 90(17):10527–10535, 2018. doi:10.1021/acs.analchem.8b02599.

[29] J. Yao, A. A. Kaberniuk, L. Li, D. M. Shcherbakova, R. Zhang, L. Wang, G. Li, V. V. Verkhusha, and L. V. Wang. Multiscale photoacoustic tomography using reversibly switchable bacterial phytochrome as a near-infrared photochromic probe.

Nature Methods, 13:67 EP –, 2015. URL: http://dx.doi.org/10.1038/nmeth.3656, doi:10.1038/nmeth.3656.

[30] Li Li, Roger J. Zemp, Gina F. Lungu, George Stoica, and Lihong V. Wang. Photoacoustic imaging of lacz gene expression in vivo. 12 IS -:020504–12–3, 2007. URL: https://doi.org/10.1117/1.2717531.

[31] L. I. LI, H. F. ZHANG, R. J. ZEMP, K. MASLOV, and L. V. Wang. Simultaneous imaging of a lacz-marked tumor and microvasculature morphology in vivo by dual-wavelength photoacoustic microscopy. *Journal of Innovative Optical Health Sciences*, 01(02):207–215, 2008. doi:10.1142/S1793545808000212.

[32] Joanna Brunker, Junjie Yao, Jan Laufer, and Sarah E. Bohndiek. Photoacoustic imaging using genetically encoded reporters: a review. 22 IS -:070901–22–18, 2017. URL: https://doi.org/10.1117/1.JBO.22.7.070901.

[33] A. P. Jathoul, J. Laufer, O. Ogunlade, B. Treeby, B. Cox, E. Zhang, P. Johnson, A. R. Pizzey, B. Philip, T. Marafioti, M. F. Lythgoe, R. B. Pedley, M. A. Pule, and P. Beard. Deep in vivo photoacoustic imaging of mammalian tissues using a tyrosinase-based genetic reporter. *Nature Photonics*, 9:239 EP –, 2015. URL: http://dx.doi.org/10.1038/nphoton.2015.22, doi:10.1038/nphoton.2015.22.

[34] R. J. Paproski, A. E. Forbrich, K. Wachowicz, M. M. Hitt, and R. J. ZEMP. Tyrosinase as a dual reporter gene for both photoacoustic and magnetic resonance imaging. *Biomedical Optics Express*, 2(4):771–780, 2011. doi:10.1364/BOE.2.000771.

[35] R. J. Paproski, A. Heinmiller, K. Wachowicz, and R. J. ZEMP. Multi-wavelength photoacoustic imaging of inducible tyrosinase reporter gene expression in xenograft tumors. *Scientific Reports*, 4:5329 EP –, 2014. URL: http://dx.doi.org/10.1038/srep05329, doi:10.1038/srep05329.

[36] J. Stritzker, L. Kirscher, M. Scadeng, N. C. Deliolanis, S. Morscher, P. Symvoulidis, K. Schaefer, Q. Zhang, L. Buckel, M. Hess, U. Donat, W. G. Bradley, V. Ntziachristos, and A. A. Szalay. Vaccinia virus-mediated melanin production allows mr and optoacoustic deep tissue imaging and laser-induced thermotherapy of cancer. *Proceedings of the National Academy of Sciences*, 110(9):3316, 2013. doi:10.1073/pnas.1216916110.

[37] R. W. Brown, Y.-C. N. Cheng, E. M. Haacke, M. R. Thompson, R. Venkatesan, and Y.-C. N. Cheng. *Magnetic Resonance Imaging: Physical Principles and Sequence Design*. Wiley, Newark, NJ, 2nd ed. edition, 2014. URL: https://ebookcentral.proquest.com/lib/gbv/detail.action?docID=4444970.

[38] R. B. Buxton. *An introduction to functional magnetic resonance imaging: Principles and techniques*. Cambridge University Press, New York and Cambridge, 2nd ed. edition, 2009. URL: http://site.ebrary.com/lib/alltitles/docDetail.action?docID=10338504.

[39] A. A. Gilad, K. Ziv, M. T. McMahon, P. C. M. van Zijl, M. Neeman, and J. W. M. Bulte. Mr reporter genes. *Journal of nuclear medicine : official publication, Society of Nuclear Medicine*, 49(12):1905–1908, 2008. URL: http://www.ncbi.nlm.nih.gov/pmc/articles/PMC2730187/, doi:10.2967/jnumed.108.053520.

[40] A. P. Koretsky, M. J. Brosnan, L. H. Chen, J. D. Chen, and T. van Dyke. Nmr detection of creatine kinase expressed in liver of transgenic mice: determination of free adp levels. *Proceedings of the National Academy of Sciences*, 87(8):3112, 1990. doi:10.1073/pnas.87.8.3112.

[41] Z. Li, H. Qiao, C. Lebherz, S. R. Choi, X. Zhou, G. Gao, H. F. Kung, D. J. Rader, J. M. Wilson, J. D. Glickson, and R. Zhou. Creatine kinase, a magnetic resonance-detectable marker gene for quantification of liver-directed gene transfer. *Human Gene Therapy*, 16(12):1429–1438, 2005. doi:10.1089/hum.2005.16.1429.

[42] A. Y. Louie, M. M. Hüber, E. T. Ahrens, U. Rothbächer, R. Moats, R. E. Jacobs, S. E. Fraser, and T. J. Meade. In vivo visualization of gene expression using magnetic resonance imaging. *Nature Biotechnology*, 18:321 EP –, 2000. URL: http://dx.doi.org/10.1038/73780, doi:10.1038/73780.

[43] H. Alfke, H. Stöppler, F. Nocken, J. T. Heverhagen, B. Kleb, F. Czubayko, and K. J. Klose. In vitro mr imaging of regulated gene expression. *Radiology*, 228(2):488–492, 2003. doi:10.1148/radiol.2282012006.

[44] G. G. Westmeyer, Y. Durocher, and A. Jasanoff. A secreted enzyme reporter system for mri. *Angew. Chem. Int. Ed Engl.*, 49(23):3909–3911, 2010. doi:10.1002/anie.200906712.

[45] G. G. Westmeyer, E. G. Emer, J. Lintelmann, and A. Jasanoff. Mri-based detection of alkaline phosphatase gene reporter activity using a porphyrin solubility switch. *Chemistry & biology*, 21(3):422–429, 2014. URL: http://www.ncbi.nlm.nih.gov/pmc/articles/PMC4073233/, doi:10.1016/j.chembiol.2014.01.012.

[46] R. Weissleder, A. Moore, U. Mahmood, R. Bhorade, H. Benveniste, E. A. Chiocca, and J. P. Basilion. In vivo magnetic resonance imaging of transgene expression. *Nature Medicine*, 6:351 EP –, 2000. URL: http://dx.doi.org/10.1038/73219, doi:10.1038/73219.

[47] T. Ichikawa, D. Högemann, Y. Saeki, E. Tyminski, K. Terada, R. Weissleder, E. A. Chiocca, and J. P. Basilion. Mri of transgene expression: correlation to therapeutic gene expression. *Neoplasia (New York, N.Y.)*, 4(6):523–530, 2002. URL: https://www.ncbi.nlm.nih.gov/pubmed/12407446, doi:10.1038/sj.neo.7900266.

[48] P. M. Harrison and P. Arosio. The ferritins: molecular properties, iron storage function and cellular regulation. *Biochimica et Biophysica Acta (BBA) - Bioenergetics*, 1275(3):161–203, 1996. URL: http://www.sciencedirect.com/science/article/pii/0005272896000229, doi:10.1016/0005-2728(96)00022-9.

[49] R. A. Brooks, J. Vymazal, R. B. Goldfarb, J. W. M. Bulte, and P. Aisen. Relaxometry and magnetometry of ferritin. *Magnetic Resonance in Medicine*, 40(2):227–235, 2005. doi:10.1002/mrm.1910400208.

[50] B. Cohen, H. Dafni, G. Meir, A. Harmelin, and M. Neeman. Ferritin as an endogenous mri reporter for noninvasive imaging of gene expression in c6 glioma tumors. *Neoplasia (New York, N.Y.)*, 7(2):109–117, 2004. URL: http://www.ncbi.nlm.nih.gov/pmc/articles/PMC1501126/.

[51] B. Cohen, K. Ziv, V. Plaks, T. Israely, V. Kalchenko, A. Harmelin, L. E. Benjamin, and M. Neeman. Mri detection of transcriptional regulation of gene expression in transgenic mice. *Nature Medicine*, 13:498 EP –, 2007. URL: http://dx.doi.org/10.1038/nm1497, doi:10.1038/nm1497.

[52] G. Genove, U. DeMarco, H. Xu, W. F. Goins, and E. T. Ahrens. A new transgene reporter for in vivo magnetic resonance imaging. *Nature Medicine*, 11:450 EP –, 2005. URL: http://dx.doi.org/10.1038/nm1208, doi:10.1038/nm1208.

[53] A. E. Deans, Y. Z. Wadghiri, L. M. Bernas, X. Yu, B. K. Rutt, and D. H. Turnbull. Cellular mri contrast via coexpression of transferrin receptor and ferritin. *Magnetic Resonance in Medicine*, 56(1):51–59, 2006. URL: http://www.ncbi.nlm.nih.gov/pmc/articles/PMC4079558/, doi:10.1002/mrm.20914.

[54] B. Iordanova, C. S. Robison, and E. T. Ahrens. Design and characterization of a chimeric ferritin with enhanced iron loading and transverse nmr relaxation rate. *Journal of biological inorganic chemistry : JBIC : a publication of the Society of Biological Inorganic Chemistry*, 15(6):957–965, 2010. URL: http://www.ncbi.nlm.nih.gov/pmc/articles/PMC2936821/, doi:10.1007/s00775-010-0657-7.

[55] B. Iordanova, C. S. Robison, W. F. Goins, and E. T. Ahrens. Single chain ferritin chimera as an improved mri gene reporter. *Prilozi*, 31(2):151–155, 2010. URL: http://www.ncbi.nlm.nih.gov/pmc/articles/PMC5796773/.

[56] B. Iordanova and E. T. Ahrens. In vivo magnetic resonance imaging of ferritin-based reporter visualizes native neuroblast migration. *NeuroImage*, 59(2):1004–1012, 2012. URL: http://www.sciencedirect.com/science/article/pii/S1053811911009852, doi:10.1016/j.neuroimage.2011.08.068.

[57] B. Iordanova, T. K. Hitchens, C. S. Robison, and E. T. Ahrens. Engineered mitochondrial ferritin as a magnetic resonance imaging reporter in mouse olfactory epithelium. *PLoS One*, 8(8):e72720, 2013. URL: https://doi.org/10.1371/journal.pone.0072720, doi:10.1371/journal.pone.0072720.

[58] Y. Matsumoto, R. Chen, P. Anikeeva, and A. Jasanoff. Engineering intracellular biomineralization and biosensing by a magnetic protein. *Nature Communications*, 6:8721 EP –, 2015. URL: http://dx.doi.org/10.1038/ncomms9721, doi:10.1038/ncomms9721.

[59] X. Liu, P. A. Lopez, T. W. Giessen, M. Giles, J. C. Way, and P. A. Silver. Engineering genetically-encoded mineralization and magnetism via directed evolution. *Scientific Reports*, 6:38019 EP –, 2016. URL: http://dx.doi.org/10.1038/srep38019, doi:10.1038/srep38019.

[60] P. S. Patrick, T. B. Rodrigues, M. I. Kettunen, S. K. Lyons, A. A. Neves, and K. M. Brindle. Development of timd2 as a reporter gene for mri. *Magnetic Resonance in Medicine*, 75(4):1697–1707, 2015. URL: http://www.ncbi.nlm.nih.gov/pmc/articles/PMC4832381/, doi:10.1002/mrm.25750.

[61] S. Geninatti Crich, M. Cadenazzi, S. Lanzardo, L. Conti, R. Ruiu, D. Alberti, F. Cavallo, J. C. Cutrin, and S. Aime. Targeting ferritin receptors for the selective delivery of imaging and therapeutic agents to breast cancer cells. *Nanoscale*, 7(15):6527–6533, 2015. URL: http://dx.doi.org/10.1039/C5NR00352K, doi:10.1039/C5NR00352K.

[62] O. Zurkiya, A. W. S. Chan, and X. Hu. Maga is sufficient for producing magnetic nanoparticles in mammalian cells, making it an mri reporter. *Magnetic Resonance in Medicine*, 59(6):1225–1231, 2008. URL: http://www.ncbi.nlm.nih.gov/pmc/articles/PMC4416408/, doi:10.1002/mrm.21606.

[63] M. G. Shapiro, G. G. Westmeyer, P. A. Romero, J. O. Szablowski, B. Küster, A. Shah, C. R. Otey, R. Langer, F. H. Arnold, and A. Jasanoff. Directed evolution of a magnetic resonance imaging contrast agent for noninvasive imaging of dopamine. *Nature Biotechnology*, 28:264 EP –, 2010. URL: http://dx.doi.org/10.1038/nbt.1609, doi:10.1038/nbt.1609.

[64] T. Lee, L. X. Cai, V. S. Lelyveld, A. Hai, and A. Jasanoff. Molecular-level functional magnetic resonance imaging of dopaminergic signaling. *Science*, 344(6183):533, 2014. doi:10.1126/science.1249380.

[65] K. Ward, A. Aletras, and R. Balaban. A new class of contrast agents for mri based on proton chemical exchange dependent saturation transfer (cest). *Journal of Magnetic Resonance*, 143(1):79–87, 2000. URL: http://www.sciencedirect.com/science/article/pii/S1090780799919560, doi:10.1006/jmre.1999.1956.

[66] C. T. Farrar, J. S. Buhrman, G. Liu, A. Kleijn, M. L. M. Lamfers, M. T. McMahon, A. A. Gilad, and G. Fulci. Establishing the lysine-rich protein cest reporter gene as a cest mr imaging detector for oncolytic virotherapy. *Radiology*, 275(3):746–754, 2015. doi:10.1148/radiol.14140251.

[67] S. Meier, A. A. Gilad, J. A. Brandon, C. Qian, E. Gao, J. F. Abisambra, and M. Vandsburger. Non-invasive detection of adeno-associated viral gene transfer using a genetically encoded cest-mri reporter gene in the murine heart. *Sci. Rep.*, 8(1):4638, 2018. URL: https://doi.org/10.1038/s41598-018-22993-4, doi:10.1038/s41598-018-22993-4.

[68] M. G. Shapiro, R. M. Ramirez, L. J. Sperling, G. Sun, J. Sun, A. Pines, D. V. Schaffer, and V. S. Bajaj. Genetically encoded reporters for hyperpolarized xenon magnetic resonance imaging. *Nature Chemistry*, 6:629 EP –, 2014. URL: http://dx.doi.org/10.1038/nchem.1934, doi:10.1038/nchem.1934.

[69] A. Lakshmanan, G. J. Lu, A. Farhadi, S. P. Nety, M. Kunth, A. Lee-Gosselin, D. Maresca, R. W. Bourdeau, M. Yin, J. Yan, C. Witte, D. Malounda, F. S. Foster, L. Schröder, and M. G. Shapiro. Preparation of biogenic gas vesicle nanostructures for use as contrast agents for ultrasound and mri. *Nature Protocols*, 12:2050 EP –, 2017. URL: http://dx.doi.org/10.1038/nprot.2017.081, doi:10.1038/nprot.2017.081.

[70] G. J. Lu, A. Farhadi, J. O. Szablowski, A. Lee-Gosselin, S. R. Barnes, A. Lakshmanan, R. W. Bourdeau, and M. G. Shapiro. Acoustically modulated magnetic resonance imaging of gas-filled protein nanostructures. *Nature Materials*, 17(5):456–463, 2018. URL: https://doi.org/10.1038/s41563-018-0023-7, doi:10.1038/s41563-018-0023-7.

[71] A. Mukherjee, Di Wu, H. C. Davis, and M. G. Shapiro. Non-invasive imaging using reporter genes altering cellular water permeability. *Nature Communications*, 7:13891 EP –, 2016. URL: https://doi.org/10.1038/ncomms13891, doi:10.1038/ncomms13891.

[72] F. Schilling, S. Ros, D.-E. Hu, P. D'Santos, S. McGuire, R. Mair, A. J. Wright, E. Mannion, R. J. M. Franklin, A. A. Neves, and K. M. Brindle. Mri measurements of reporter-mediated increases in transmembrane water exchange enable detection of a gene reporter. *Nature Biotechnology*, 35:75 EP –, 2016. URL: http://dx.doi.org/10.1038/nbt.3714, doi:10.1038/nbt.3714.

[73] L. F. Kourkoutis, J. M. Plitzko, and W. Baumeister. Electron microscopy of biological materials at the nanometer scale. *Annual Review of Materials Research*, 42(1):33–58, 2012. doi:10.1146/annurev-matsci-070511-155004.

[74] M. Marko, C. Hsieh, R. Schalek, J. Frank, and C. Mannella. Focused-ion-beam thinning of frozen-hydrated biological specimens for cryo-electron microscopy. *Nature Methods*, 4:215 EP –, 2007. URL: https://doi.org/10.1038/nmeth1014, doi:10.1038/nmeth1014.

[75] R. Shigemoto and M. Joesch. The genetic encoded toolbox for electron microscopy and connectomics. *Wiley Interdisciplinary Reviews: Developmental Biology*, 6(6):e288, 2017. doi:10.1002/wdev.288.

[76] K. Kristensson and Y. Olsson. Retrograde axonal transport of protein. *Brain Research*, 29(2):363–365, 1971. URL: http://www.sciencedirect.com/science/article/pii/0006899371900448, doi:10.1016/0006-8993(71)90044-8.

[77] J. D. Martell, T. J. Deerinck, Y. Sancak, T. L. Poulos, V. K. Mootha, G. E. Sosinsky, M. H. Ellisman, and A. Y. Ting. Engineered ascorbate peroxidase as a genetically encoded reporter for electron microscopy. *Nat. Biotechnol.*, 30(11):1143–1148, 2012. URL: http://dx.doi.org/10.1038/nbt.2375https://www.ncbi.nlm.nih.gov/pubmed/23086203https://www.ncbi.nlm.nih.gov/pmc/articles/PMC3699407, doi:10.1038/nbt.2375.

[78] S. S. Lam, J. D. Martell, K. J. Kamer, T. J. Deerinck, M. H. Ellisman, V. K. Mootha, and A. Y. Ting. Directed evolution of apex2 for electron microscopy and proximity labeling. *Nat. Methods*, 12(1):51–54, 2015. URL: http://dx.doi.org/10.1038/nmeth.3179https://www.ncbi.nlm.nih.gov/pubmed/25419960https://www.ncbi.nlm.nih.gov/pmc/articles/PMC4296904, doi:10.1038/nmeth.3179.

[79] X. Shu, V. Lev-Ram, T. J. Deerinck, Y. Qi, E. B. Ramko, M. W. Davidson, Y. Jin, M. H. Ellisman, and R. Y. Tsien. A genetically encoded tag for correlated light and electron microscopy of intact cells, tissues, and organisms. *PLoS Biol*, 9(4):e1001041, 2011. URL: http://dx.doi.org/10.1371/journal.pbio.1001041https://www.ncbi.nlm.nih.gov/pubmed/21483721https://www.ncbi.nlm.nih.gov/pmc/articles/PMC3071375http://dx.plos.org/10.1371/journal.pbio.1001041, doi:10.1371/journal.pbio.1001041.

[80] C. Bouchet-Marquis, M. Pagratis, R. Kirmse, and A. Hoenger. Metallothionein as a clonable high-density marker for cryo-electron microscopy. *J. Struct. Biol.*, 177(1):119–127, 2012. URL: https://www.ncbi.nlm.nih.gov/pubmed/22068155, doi:10.1016/j.jsb.2011.10.007.

[81] P. Rajasethupathy, E. Ferenczi, and K. Deisseroth. Targeting neural circuits. *Cell*, 165(3):524–534, 2016. doi:10.1016/j.cell.2016.03.047.

[82] S. M. Sternson and B. L. Roth. Chemogenetic tools to interrogate brain functions. *Annual Review of Neuroscience*, 37(1):387–407, 2014. doi:10.1146/annurev-neuro-071013-014048.

[83] O. Hikosaka and R. H. Wurtz. Modification of saccadic eye movements by gaba-related substances. i. effect of muscimol and bicuculline in monkey superior colliculus. *Journal of Neurophysiology*, 53(1):266–291, 1985. doi:10.1152/jn.1985.53.1.266.

[84] B. Glenn Stanley, L. H. Ha, L. C. Spears, and M. G. Dee. Lateral hypothalamic injections of glutamate, kainic acid,d,l-a-amino-3-hydroxy-5-methyl-isoxazole propionic acid or n-methyl-d-aspartic acid rapidly elicit intense transient eating in rats. *Brain Research*, 613(1):88–95, 1993. URL: http://www.sciencedirect.com/science/article/pii/000689939390458Y, doi:10.1016/0006-8993(93)90458-Y.

[85] E. M. Slimko, S. McKinney, D. J. Anderson, N. Davidson, and H. A. Lester. Selective electrical silencing of mammalian neurons in vitro by the use of invertebrate ligand-gated chloride channels. *The Journal of Neuroscience*, 22(17):7373, 2002. doi:10.1523/JNEUROSCI.22-17-07373.2002.

[86] Li Ping, Slimko Eric M, and Lester Henry A. Selective elimination of glutamate activation and introduction of fluorescent proteins into a caenorhabditis elegans chloride channel. *FEBS Letters*, 528(1-3):77–82, 2002. doi:10.1016/S0014-5793(02)03245-3.

[87] T. Lynagh and J. W. Lynch. An improved ivermectin-activated chloride channel receptor for inhibiting electrical activity in defined neuronal populations. *Journal of Biological Chemistry*, 285(20):14890–14897, 2010. doi:10.1074/jbc.M110.107789.

[88] A. D. Güler, A. Rainwater, J. G. Parker, G. L. Jones, E. Argilli, B. R. Arenkiel, M. D. Ehlers, A. Bonci, L. S. Zweifel, and R. D. Palmiter. Transient activation of specific neurons in mice by selective expression of the capsaicin receptor. *Nature Communications*, 3:746 EP –, 2012. URL: http://dx.doi.org/10.1038/ncomms1749, doi:10.1038/ncomms1749.

[89] P. Gau, J. Poon, C. Ufret-Vincenty, C. D. Snelson, S. E. Gordon, D. W. Raible, and A. Dhaka. The zebrafish ortholog of trpv1 is required for heat-induced locomotion. *The Journal of Neuroscience*, 33(12):5249, 2013. doi:10.1523/JNEUROSCI.5403-12.2013.

[90] S.-L. Chen, L. J. Guo, and X. Wang. All-optical photoacoustic microscopy. *Photoacoustics*, 3(4):143–150, 2015. URL: http://www.sciencedirect.com/science/article/pii/S2213597915300069, doi:10.1016/j.pacs.2015.11.001.

[91] M. S. Farrell and B. L. Roth. Pharmacosynthetics: Reimagining the pharmacogenetic approach. *Brain Research*, 1511:6–20, 2013. URL: http://www.sciencedirect.com/science/article/pii/S0006899312016046, doi:10.1016/j.brainres.2012.09.043.

[92] C. D. Strader, T. Gaffney, E. E. Sugg, M. R. Candelore, R. Keys, A. A. Patchett, and R. A. Dixon. Allele-specific activation of genetically engineered receptors. *Journal of Biological Chemistry*, 266(1):5–8, 1991.

[93] B. N. Armbruster and B. L. Roth. Mining the receptorome. *Journal of Biological Chemistry*, 280(7):5129–5132, 2005. URL: http://www.jbc.org/content/280/7/5129.short, doi:10.1074/jbc.R400030200.

[94] B. N. Armbruster, X. Li, M. H. Pausch, S. Herlitze, and B. L. Roth. Evolving the lock to fit the key to create a family of g protein-coupled receptors potently activated by an inert ligand. *Proceedings of the National Academy of Sciences*, 104(12):5163, 2007. doi:10.1073/pnas.0700293104.

[95] S. Dong, S. C. Rogan, and B. L. Roth. Directed molecular evolution of dreadds: a generic approach to creating next-generation rassls. *Nature Protocols*, 5:561 EP –, 2010. URL: http://dx.doi.org/10.1038/nprot.2009.239, doi:10.1038/nprot.2009.239.

[96] S. C. Rogan, B. L. Roth, and A. L. Morrow. Remote control of neuronal signaling. *Pharmacological Reviews*, 63(2):291, 2011. doi:10.1124/pr.110.003020.

[97] J.-M. Guettier, D. Gautam, M. Scarselli, I. R. de Azua, J. H. Li, E. Rosemond, X. Ma, F. J. Gonzalez, B. N. Armbruster, H. Lu, B. L. Roth, and J. Wess. A chemical-genetic approach to study g protein regulation of b cell function in vivo. *Proceedings of the National Academy of Sciences*, 106(45):19197, 2009. doi:10.1073/pnas.0906593106.

[98] K.-i. Nakajima and J. Wess. Design and functional characterization of a novel, arrestin-biased designer g protein-coupled receptor. *Molecular Pharmacology*, 82(4):575, 2012. doi:10.1124/mol.112.080358.

[99] J. L. Gomez, J. Bonaventura, W. Lesniak, W. B. Mathews, P. Sysa-Shah, L. A. Rodriguez, R. J. Ellis, C. T. Richie, B. K. Harvey, R. F. Dannals, M. G. Pomper, A. Bonci, and M. Michaelides. Chemogenetics revealed: Dreadd occupancy and activation via converted clozapine. *Science*, 357(6350):503, 2017. doi:10.1126/science.aan2475.

[100] J. G. Bernstein, P. A. Garrity, and E. S. Boyden. Optogenetics and thermogenetics: technologies for controlling the activity of targeted cells within intact neural circuits. *Current Opinion in Neurobiology*, 22(1):61–71, 2012. URL: http://www.sciencedirect.com/science/article/pii/S0959438811001905, doi:10.1016/j.conb.2011.10.023.

[101] T. Kitamoto. Conditional modification of behavior in drosophila by targeted expression of a temperature-sensitive shibire allele in defined neurons. *Journal of Neurobiology*, 47(2):81–92, 2001. doi:10.1002/neu.1018.

[102] J. H. Simpson. Chapter 3 mapping and manipulating neural circuits in the fly brain. In *Advances in Genetics : Genetic Dissection of Neural Circuits and Behavior*, volume 65, pages 79–143. Academic Press, 2009. URL: http://www.sciencedirect.com/science/article/pii/S0065266009650033, doi:10.1016/S0065-2660(09)65003-3.

[103] M. Tominaga and M. J. Caterina. Thermosensation and pain. *Journal of Neurobiology*, 61(1):3–12, 2004. doi:10.1002/neu.20079.

[104] S. R. Pulver, S. L. Pashkovski, N. J. Hornstein, P. A. Garrity, and L. C. Griffith. Temporal dynamics of neuronal activation by channelrhodopsin-2 and trpa1 determine behavioral output in drosophila larvae. *Journal of Neurophysiology*, 101(6):3075–3088, 2009. doi:10.1152/jn.00071.2009.

[105] N. C. Peabody, J. B. Pohl, F. Diao, A. P. Vreede, D. J. Sandstrom, H. Wang, P. K. Zelensky, and B. H. White. Characterization of the decision network for wing expansion in drosophila using targeted expression of the trpm8 channel. *The Journal of Neuroscience*, 29(11):3343, 2009. doi:10.1523/JNEUROSCI.4241-08.2009.

[106] D. E. Bath, J. R. Stowers, D. Hörmann, A. Poehlmann, B. J. Dickson, and A. D. Straw. Flymad: rapid thermogenetic control of neuronal activity in freely walking drosophila. *Nature Methods*, 11:756 EP –, 2014. URL: http://dx.doi.org/10.1038/nmeth.2973, doi:10.1038/nmeth.2973.

[107] F. Zhang, J. Vierock, O. Yizhar, L. E. Fenno, S. Tsunoda, A. Kianianmomeni, M. Prigge, A. Berndt, J. Cushman, J. Polle, J. Magnuson, P. Hegemann, and K. Deisseroth. The microbial opsin family of optogenetic tools. *Cell*, 147(7):1446–1457, 2011. doi:10.1016/j.cell.2011.12.004.

[108] V. Gradinaru, F. Zhang, C. Ramakrishnan, J. Mattis, R. Prakash, I. Diester, I. Goshen, K. R. Thompson, and K. Deisseroth. Molecular and cellular approaches for diversifying and extending optogenetics. *Cell*, 141(1):154–165, 2010. doi:10.1016/j.cell.2010.02.037.

[109] E. S. Boyden, F. Zhang, E. Bamberg, G. Nagel, and K. Deisseroth. Millisecond-timescale, genetically targeted optical control of neural activity. *Nature Neuroscience*, 8:1263 EP –, 2005. doi:10.1038/nn1525.

[110] K. Deisseroth, G. Feng, A. K. Majewska, G. Miesenböck, A. Ting, and M. J. Schnitzer. Next-generation optical technologies for illuminating genetically targeted brain circuits. *The Journal of Neuroscience*, 26(41):10380, 2006. doi:10.1523/JNEUROSCI.3863-06.2006.

[111] Alexander M Aravanis and Li-Ping Wang and Feng Zhang and Leslie A Meltzer and Murtaza Z Mogri and M Bret Schneider and Karl Deisseroth. An optical neural interface: in vivo control of rodent motor cortex with integrated fiberoptic and optogenetic technology. *Journal of Neural Engineering*, 4(3):S143, 2007.

[112] A. R. Adamantidis, F. Zhang, A. M. Aravanis, K. Deisseroth, and L. de Lecea. Neural substrates of awakening probed with optogenetic control of hypocretin neurons. *Nature*, 450:420 EP –, 2007. URL: http://dx.doi.org/10.1038/nature06310, doi:10.1038/nature06310.

[113] K. Deisseroth. Optogenetics: 10 years of microbial opsins in neuroscience. *Nature Neuroscience*, 18:1213 EP –, 2015. doi:10.1038/nn.4091.

[114] H. E. Kato, F. Zhang, O. Yizhar, C. Ramakrishnan, T. Nishizawa, K. Hirata, J. Ito, Y. Aita, T. Tsukazaki, S. Hayashi, P. Hegemann, A. D. Maturana, R. Ishitani, K. Deisseroth, and O. Nureki. Crystal structure of the channelrhodopsin light-gated cation channel. *Nature*, 482:369 EP –, 2012. doi:10.1038/nature10870.

[115] A. Berndt, S. Y. Lee, C. Ramakrishnan, and K. Deisseroth. Structure-guided transformation of channelrhodopsin into a light-activated chloride channel. *Science*, 344(6182):420, 2014. doi:10.1126/science.1252367.

[116] J. Wietek, J. S. Wiegert, N. Adeishvili, F. Schneider, H. Watanabe, S. P. Tsunoda, A. Vogt, M. Elstner, T. G. Oertner, and P. Hegemann. Conversion of channelrhodopsin into a light-gated chloride channel. *Science*, 344(6182):409, 2014. doi:10.1126/science.1249375.

[117] H. Huang, S. Delikanli, H. Zeng, D. M. Ferkey, and A. Pralle. Remote control of ion channels and neurons through magnetic-field heating of nanoparticles. *Nature Nanotechnology*, 5:602 EP –, 2010. URL: http://dx.doi.org/10.1038/nnano.2010.125, doi:10.1038/nnano.2010.125.

[118] S. Chen, C. N. Chiu, K. L. McArthur, J. R. Fetcho, and D. A. Prober. Trp channel mediated neuronal activation and ablation in freely behaving zebrafish. *Nature Methods*, 13:147 EP –, 2015. URL: http://dx.doi.org/10.1038/nmeth.3691, doi:10.1038/nmeth.3691.

[119] S. A. Stanley, J. E. Gagner, S. Damanpour, M. Yoshida, J. S. Dordick, and J. M. Friedman. Radio-wave heating of iron oxide nanoparticles can regulate plasma glucose in mice. *Science*, 336(6081):604, 2012. doi:10.1126/science.1216753.

[120] S. A. Stanley, J. Sauer, R. S. Kane, J. S. Dordick, and J. M. Friedman. Corrigendum: Remote regulation of glucose homeostasis in mice using genetically encoded nanoparticles. *Nat Med*, 21(5):537, 2015. URL: https://www.ncbi.nlm.nih.gov/pubmed/25951532, doi:10.1038/nm0515-537b.

[121] S. A. Stanley, L. Kelly, K. N. Latcha, S. F. Schmidt, X. Yu, A. R. Nectow, J. Sauer, J. P. Dyke, J. S. Dordick, and J. M. Friedman. Bidirectional electromagnetic control of the hypothalamus regulates feeding and metabolism. *Nature*, 531:647 EP –, 2016. URL: http://dx.doi.org/10.1038/nature17183, doi:10.1038/nature17183.

[122] M. A. Wheeler, C. J. Smith, M. Ottolini, B. S. Barker, A. M. Purohit, R. M. Grippo, R. P. Gaykema, A. J. Spano, M. P. Beenhakker, S. Kucenas, M. K. Patel, C. D. Deppmann, and A. D. Güler. Genetically targeted magnetic control of the nervous system. *Nature Neuroscience*, 19:756 EP –, 2016. URL: http://dx.doi.org/10.1038/nn.4265, doi:10.1038/nn.4265.

[123] S. Qin, H. Yin, C. Yang, Y. Dou, Z. Liu, P. Zhang, H. Yu, Y. Huang, J. Feng, J. Hao, J. Hao, L. Deng, X. Yan, X. Dong, Z. Zhao, T. Jiang, H.-W. Wang, S.-J. Luo, and C. Xie. A magnetic protein biocompass. *Nature Materials*, 15:217 EP –, 2015. URL: http://dx.doi.org/10.1038/nmat4484, doi:10.1038/nmat4484.

[124] X. Long, J. Ye, Di Zhao, and S.-J. Zhang. Magnetogenetics: remote non-invasive magnetic activation of neuronal activity with a magnetoreceptor. *Science Bul-*

letin, 60(24):2107–2119, 2015. URL: http://www.sciencedirect.com/science/article/pii/S2095927316302407, doi:10.1007/s11434-015-0902-0.

[125] M. Meister and D. E. Clapham. Physical limits to magnetogenetics. *Elife*, 5:e17210, 2016. doi:10.7554/eLife.17210.

[126] G. Duret, S. Polali, E. D. Anderson, A. M. Bell, C. N. Tzouanas, B. W. Avants, and J. T. Robinson. Magnetic entropy as a gating mechanism for magnetogenetic ion channels. *bioRxiv*, 2017. doi:10.1101/148379.

[127] J. Wu, R. Goyal, and J. Grandl. Localized force application reveals mechanically sensitive domains of piezo1. *Nature Communications*, 7:12939 EP –, 2016. URL: https://doi.org/10.1038/ncomms12939, doi:10.1038/ncomms12939.

[128] W. J. Tyler, Y. Tufail, M. Finsterwald, M. L. Tauchmann, E. J. Olson, and C. Majestic. Remote excitation of neuronal circuits using low-intensity, low-frequency ultrasound. *PLoS One*, 3(10):e3511, 2008. URL: https://doi.org/10.1371/journal.pone.0003511, doi:10.1371/journal.pone.0003511.

[129] W. J. Tyler. The mechanobiology of brain function. *Nature Reviews Neuroscience*, 13:867 EP –, 2012. URL: http://dx.doi.org/10.1038/nrn3383, doi:10.1038/nrn3383.

[130] Y. Tufail, A. Yoshihiro, S. Pati, M. M. Li, and W. J. Tyler. Ultrasonic neuromodulation by brain stimulation with transcranial ultrasound. *Nature Protocols*, 6:1453 EP –, 2011. URL: http://dx.doi.org/10.1038/nprot.2011.371, doi:10.1038/nprot.2011.371.

[131] S. Ibsen, A. Tong, C. Schutt, S. Esener, and S. H. Chalasani. Sonogenetics is a non-invasive approach to activating neurons in caenorhabditis elegans. *Nature Communications*, 6:8264 EP –, 2015. URL: http://dx.doi.org/10.1038/ncomms9264, doi:10.1038/ncomms9264.

[132] A. D. Güler, H. Lee, T. Iida, I. Shimizu, M. Tominaga, and M. Caterina. Heat-evoked activation of the ion channel, trpv4. *The Journal of Neuroscience*, 22(15):6408, 2002. doi:10.1523/JNEUROSCI.22-15-06408.2002.

[133] B. Alberts. *Molecular biology of the cell*. Garland Science, New York, 5th ed. edition, 2008.

[134] M. Krupovic and E. V. Koonin. Multiple origins of viral capsid proteins from cellular ancestors. *Proceedings of the National Academy of Sciences*, 2017. URL: http://www.pnas.org/content/pnas/early/2017/03/03/1621061114.full.pdf, doi:10.1073/pnas.1621061114.

[135] R. J. Nichols, C. Cassidy-Amstutz, T. Chaijarasphong, and D. F. Savage. Encapsulins: molecular biology of the shell. *Critical Reviews in Biochemistry and Molecular Biology*, 52(5):583–594, 2017. doi:10.1080/10409238.2017.1337709.

[136] M. Sutter, D. Boehringer, S. Gutmann, S. Günther, D. Prangishvili, M. J. Loessner, K. O. Stetter, E. Weber-Ban, and N. Ban. Structural basis of enzyme encapsulation into a bacterial nanocompartment. *Nat. Struct. Mol. Biol.*, 15(9):939–947, 2008. URL: `http://dx.doi.org/10.1038/nsmb.1473https://www.ncbi.nlm.nih.gov/pubmed/19172747`, `doi:10.1038/nsmb.1473`.

[137] T. W. Giessen and P. A. Silver. Widespread distribution of encapsulin nanocompartments reveals functional diversity. *Nature Microbiology*, 2:17029, 2017. URL: `http://dx.doi.org/10.1038/nmicrobiol.2017.29`, `doi:10.1038/nmicrobiol.2017.29`.

[138] C. A. McHugh, J. Fontana, D. Nemecek, N. Cheng, A. A. Aksyuk, J. B. Heymann, D. C. Winkler, A. S. Lam, J. S. Wall, A. C. Steven, and Others. A virus capsid-like nanocompartment that stores iron and protects bacteria from oxidative stress. *EMBO J*, 33(17):1896–1911, 2014.

[139] D. He, S. Hughes, S. Vanden-Hehir, A. Georgiev, K. Altenbach, E. Tarrant, C. L. Mackay, K. J. Waldron, D. J. Clarke, and J. Marles-Wright. Structural characterization of encapsulated ferritin provides insight into iron storage in bacterial nanocompartments. *Elife*, 5, 2016. URL: `http://dx.doi.org/10.7554/eLife.18972https://www.ncbi.nlm.nih.gov/pubmed/27529188https://www.ncbi.nlm.nih.gov/pmc/articles/PMC5012862https://doi.org/10.7554/eLife.18972`, `doi:10.7554/eLife.18972`.

[140] F. Akita, K. T. Chong, H. Tanaka, E. Yamashita, N. Miyazaki, Y. Nakaishi, M. Suzuki, K. Namba, Y. Ono, T. Tsukihara, and A. Nakagawa. The crystal structure of a virus-like particle from the hyperthermophilic archaeon pyrococcus furiosus provides insight into the evolution of viruses. *Journal of Molecular Biology*, 368(5):1469–1483, 2007. URL: `http://www.sciencedirect.com/science/article/pii/S0022283607002677`, `doi:10.1016/j.jmb.2007.02.075`.

[141] N. Valdés-Stauber and S. Scherer. Isolation and characterization of linocin m18, a bacteriocin produced by brevibacterium linens. *Applied and Environmental Microbiology*, 60(10):3809–3814, 1994.

[142] R. Rahman and B. T. D. H. Assembly in vitro of rhodococcus jostii rha1 encapsulin and peroxidase dypb to form a nanocompartment. *The FEBS Journal*, 280(9):2097–2104, 2013. `doi:10.1111/febs.12234`.

[143] W. F. Rurup, J. Snijder, M. S. T. Koay, A. J. R. Heck, and Cornelissen, Jeroen J. L. M. Self-sorting of foreign proteins in a bacterial nanocompartment. *J. Am. Chem. Soc.*, 136(10):3828–3832, 2014. `doi:10.1021/ja410891c`.

[144] J. Snijder, O. Kononova, I. M. Barbu, C. Uetrecht, W. F. Rurup, R. J. Burnley, M. S. T. Koay, Cornelissen, Jeroen J. L. M., W. H. Roos, V. Barsegov, G. J. L.

Wuite, and A. J. R. Heck. Assembly and mechanical properties of the cargo-free and cargo-loaded bacterial nanocompartment encapsulin. *Biomacromolecules*, 17(8):2522–2529, 2016. doi:10.1021/acs.biomac.6b00469.

[145] A. Tamura, Y. Fukutani, T. Takami, M. Fujii, Y. Nakaguchi, Y. Murakami, K. Noguchi, M. Yohda, and M. Odaka. Packaging guest proteins into the encapsulin nanocompartment from rhodococcus erythropolis n771. *Biotechnol. Bioeng.*, 112(1):13–20, 2015. URL: http://dx.doi.org/10.1002/bit.25322https://www.ncbi.nlm.nih.gov/pubmed/24981030, doi:10.1002/bit.25322.

[146] C. Cassidy-Amstutz, L. Oltrogge, C. C. Going, A. Lee, P. Teng, D. Quintanilla, A. East-Seletsky, E. R. Williams, and D. F. Savage. Identification of a minimal peptide tag for in vivo and in vitro loading of encapsulin. *Biochemistry*, 55(24):3461–3468, 2016. doi:10.1021/acs.biochem.6b00294.

[147] T. W. Giessen and P. A. Silver. Encapsulation as a strategy for the design of biological compartmentalization. *Journal of Molecular Biology*, 428(5 Pt B):916–927, 2016. URL: http://dx.doi.org/10.1016/j.jmb.2015.09.009https://www.ncbi.nlm.nih.gov/pubmed/26403362https://linkinghub.elsevier.com/retrieve/pii/S0022-2836(15)00520-3http://www.sciencedirect.com/science/article/pii/S0022283615005203, doi:10.1016/j.jmb.2015.09.009.

[148] H. Moon, J. Lee, J. Min, and S. Kang. Developing genetically engineered encapsulin protein cage nanoparticles as a targeted delivery nanoplatform. *Biomacromolecules*, 15(10):3794–3801, 2014. URL: http://dx.doi.org/10.1021/bm501066mhttps://www.ncbi.nlm.nih.gov/pubmed/25180761https://dx.doi.org/10.1021/bm501066m, doi:10.1021/bm501066m.

[149] H. Moon, J. Lee, H. Kim, S. Heo, J. Min, and S. Kang. Genetically engineering encapsulin protein cage nanoparticle as a scc-7 cell targeting optical nanoprobe. *Biomaterials Research*, 18(1):21, 2014. URL: https://doi.org/10.1186/2055-7124-18-21, doi:10.1186/2055-7124-18-21.

[150] Y. H. Lau, T. W. Giessen, W. J. Altenburg, and P. A. Silver. Prokaryotic nanocompartments form synthetic organelles in a eukaryote. *Nat. Commun.*, 9(1):1311, 2018. doi:10.1038/s41467-018-03768-x.

[151] M. Kanekiyo, W. Bu, M. G. Joyce, G. Meng, J. R. R. Whittle, U. Baxa, T. Yamamoto, S. Narpala, J.-P. Todd, S. S. Rao, A. B. McDermott, R. A. Koup, M. G. Rossmann, J. R. Mascola, B. S. Graham, J. I. Cohen, and G. J. Nabel. Rational design of an epstein-barr virus vaccine targeting the receptor-binding site. *Cell*, 162(5):1090–1100, 2015. URL: http://dx.doi.org/10.1016/j.cell.2015.07.043https://www.ncbi.nlm.nih.gov/pubmed/26279189https://www.ncbi.nlm.nih.gov/pmc/articles/PMC4757492https://linkinghub.elsevier.com/retrieve/pii/S0092-8674(15)00959-9, doi:10.1016/j.cell.2015.07.043.

[152] B. Choi, H. Moon, S. J. Hong, C. Shin, Y. Do, S. Ryu, and S. Kang. Effective delivery of antigen–encapsulin nanoparticle fusions to dendritic cells leads to antigen-specific cytotoxic t cell activation and tumor rejection. *ACS Nano*, 10(8):7339–7350, 2016. doi:10.1021/acsnano.5b08084.

[153] P. Lagoutte, C. Mignon, G. Stadthagen, S. Potisopon, S. Donnat, J. Mast, A. Lugari, and B. Werle. Simultaneous surface display and cargo loading of encapsulin nanocompartments and their use for rational vaccine design. *Vaccine*, 36(25):3622–3628, 2018. doi:10.1016/j.vaccine.2018.05.034.

[154] M. Delarue, G. P. Brittingham, S. Pfeffer, I. V. Surovtsev, S. Pinglay, K. J. Kennedy, M. Schaffer, J. I. Gutierrez, D. Sang, G. Poterewicz, J. K. Chung, J. M. Plitzko, J. T. Groves, C. Jacobs-Wagner, B. D. Engel, and L. J. Holt. mtorc1 controls phase separation and the biophysical properties of the cytoplasm by tuning crowding. *Cell*. doi:10.1016/j.cell.2018.05.042.

[155] M. Comellas-Aragonès, H. Engelkamp, V. I. Claessen, Sommerdijk, Nico A. J. M., A. E. Rowan, P. C. M. Christianen, J. C. Maan, B. J. M. Verduin, Cornelissen, Jeroen J. L. M., and R. J. M. Nolte. A virus-based single-enzyme nanoreactor. *Nat. Nanotechnol.*, 2(10):635–639, 2007. URL: http://dx.doi.org/10.1038/nnano.2007.299https://www.ncbi.nlm.nih.gov/pubmed/18654389, doi:10.1038/nnano.2007.299.

[156] T. Douglas, E. Strable, D. Willits, A. Aitouchen, M. Libera, M. Young, and Others. Protein engineering of a viral cage for constrained nanomaterials synthesis. *Adv. Mater.*, 14(6):415, 2002. URL: http://www.academia.edu/download/46867919/1521-4095_2820020318_2914_3A6_3C415_3A_3Aaid-adma415_3E3.0.co_3B2-w20160628-6344-1yi49kt.pdf.

[157] O'Neil Alison, Reichhardt Courtney, Johnson Benjamin, Prevelige Peter E., and Douglas Trevor. Genetically programmed in vivo packaging of protein cargo and its controlled release from bacteriophage p22. *Angew. Chem. Int. Ed Engl.*, 50(32):7425–7428, 2011. doi:10.1002/anie.201102036.

[158] A. O'Neil, P. E. Prevelige, G. Basu, and T. Douglas. Coconfinement of fluorescent proteins: spatially enforced communication of gfp and mcherry encapsulated within the p22 capsid. *Biomacromolecules*, 13(12):3902–3907, 2012. URL: http://dx.doi.org/10.1021/bm301347xhttps://www.ncbi.nlm.nih.gov/pubmed/23121071https://dx.doi.org/10.1021/bm301347x, doi:10.1021/bm301347x.

[159] D. P. Patterson, P. E. Prevelige, and T. Douglas. Nanoreactors by programmed enzyme encapsulation inside the capsid of the bacteriophage p22. *ACS Nano*, 6(6):5000–5009, 2012. URL: http://dx.doi.org/10.1021/nn300545zhttps://www.ncbi.nlm.nih.gov/pubmed/22624576https://dx.doi.org/10.1021/nn300545z, doi:10.1021/nn300545z.

[160] D. P. Patterson, B. Schwarz, R. S. Waters, T. Gedeon, and T. Douglas. Encapsulation of an enzyme cascade within the bacteriophage p22 virus-like particle. *ACS Chem. Biol.*, 9(2):359–365, 2014. URL: http://dx.doi.org/10.1021/cb4006529https://www.ncbi.nlm.nih.gov/pubmed/24308573https://dx.doi.org/10.1021/cb4006529, doi:10.1021/cb4006529.

[161] S. Choudhary, M. B. Quin, M. A. Sanders, E. T. Johnson, and C. Schmidt-Dannert. Engineered protein nano-compartments for targeted enzyme localization. *PLoS One*, 7(3):e33342, 2012. doi:10.1371/journal.pone.0033342.

[162] M. Held, A. Kolb, S. Perdue, S.-Y. Hsu, S. E. Bloch, M. B. Quin, and C. Schmidt-Dannert. Engineering formation of multiple recombinant eut protein nanocompartments in e. coli. *Sci. Rep.*, 6:24359, 2016. URL: http://dx.doi.org/10.1038/srep24359https://www.ncbi.nlm.nih.gov/pubmed/27063436https://www.ncbi.nlm.nih.gov/pmc/articles/PMC4827028https://www.nature.com/articles/srep24359?WT.feed_name=subjects_biotechnology, doi:10.1038/srep24359.

[163] F. Cai, M. Sutter, S. L. Bernstein, J. N. Kinney, and C. A. Kerfeld. Engineering bacterial microcompartment shells: Chimeric shell proteins and chimeric carboxysome shells. *ACS Synthetic Biology*, 4(4):444–453, 2015. doi:10.1021/sb500226j.

[164] E. J. Young, R. Burton, J. P. Mahalik, B. G. Sumpter, M. Fuentes-Cabrera, C. A. Kerfeld, and D. C. Ducat. Engineering the bacterial microcompartment domain for molecular scaffolding applications. *Frontiers in Microbiology*, 8:1441, 2017. doi:10.3389/fmicb.2017.01441.

[165] N. L. Kedersha, J. E. Heuser, D. C. Chugani, and L. H. Rome. Vaults. iii. vault ribonucleoprotein particles open into flower-like structures with octagonal symmetry. *J. Cell Biol.*, 112(2):225–235, 1991. URL: https://www.ncbi.nlm.nih.gov/pubmed/1988458https://www.ncbi.nlm.nih.gov/pmc/articles/PMC2288824http://jcb.rupress.org/cgi/pmidlookup?view=long&pmid=1988458.

[166] V. A. Kickhoefer, Y. Garcia, Y. Mikyas, E. Johansson, J. C. Zhou, S. Raval-Fernandes, P. Minoofar, J. I. Zink, B. Dunn, P. L. Stewart, and L. H. Rome. Engineering of vault nanocapsules with enzymatic and fluorescent properties. *Proc. Natl. Acad. Sci. U. S. A.*, 102(12):4348–4352, 2005. URL: http://dx.doi.org/10.1073/pnas.0500929102https://www.ncbi.nlm.nih.gov/pubmed/15753293https://www.ncbi.nlm.nih.gov/pmc/articles/PMC555531http://www.pnas.org/cgi/pmidlookup?view=long&pmid=15753293, doi:10.1073/pnas.0500929102.

[167] M. Slesina, E. M. Inman, A. E. Moore, J. I. Goldhaber, L. H. Rome, and W. Volknandt. Movement of vault particles visualized by gfp-tagged major vault protein.

Cell Tissue Res, 324(3):403–410, 2006. URL: http://dx.doi.org/10.1007/s00441-006-0158-8https://www.ncbi.nlm.nih.gov/pubmed/16505994https://dx.doi.org/10.1007/s00441-006-0158-8http://link.springer.com/article/10.1007/s00441-006-0158-8, doi:10.1007/s00441-006-0158-8.

[168] M. Wang, D. Abad, V. A. Kickhoefer, L. H. Rome, and S. Mahendra. Vault nanoparticles packaged with enzymes as an efficient pollutant biodegradation technology. *ACS Nano*, 9(11):10931–10940, 2015. URL: http://dx.doi.org/10.1021/acsnano.5b04073https://www.ncbi.nlm.nih.gov/pubmed/26493711https://dx.doi.org/10.1021/acsnano.5b04073, doi:10.1021/acsnano.5b04073.

[169] M. C. Huber, A. Schreiber, P. von Olshausen, B. R. Varga, O. Kretz, B. Joch, S. Barnert, R. Schubert, S. Eimer, P. Kele, and S. M. Schiller. Designer amphiphilic proteins as building blocks for the intracellular formation of organelle-like compartments. *Nat. Mater.*, 14(1):125–132, 2015. URL: http://dx.doi.org/10.1038/nmat4118https://www.ncbi.nlm.nih.gov/pubmed/25362355, doi:10.1038/nmat4118.

[170] Y. Hsia, J. B. Bale, S. Gonen, D. Shi, W. Sheffler, K. K. Fong, U. Nattermann, C. Xu, P.-S. Huang, R. Ravichandran, S. Yi, T. N. Davis, T. Gonen, N. P. King, and D. Baker. Design of a hyperstable 60-subunit protein icosahedron. *Nature*, 535:136 EP –, 2016. doi:10.1038/nature18010.

[171] J. B. Bale, S. Gonen, Y. Liu, W. Sheffler, D. Ellis, C. Thomas, D. Cascio, T. O. Yeates, T. Gonen, N. P. King, and D. Baker. Accurate design of megadalton-scale two-component icosahedral protein complexes. *Science*, 353(6297):389, 2016. doi:10.1126/science.aaf8818.

[172] G. L. Butterfield, M. J. Lajoie, H. H. Gustafson, D. L. Sellers, U. Nattermann, D. Ellis, J. B. Bale, S. Ke, G. H. Lenz, A. Yehdego, R. Ravichandran, S. H. Pun, N. P. King, and D. Baker. Evolution of a designed protein assembly encapsulating its own rna genome. *Nature*, 552:415 EP –, 2017. doi:10.1038/nature25157.

[173] P. Anikeeva and A. Jasanoff. Problems on the back of an envelope. *Elife*, 5:e19569, 2016. doi:10.7554/eLife.19569.

[174] R. K. Huang, R. Khayat, K. K. Lee, I. Gertsman, R. L. Duda, R. W. Hendrix, and J. E. Johnson. The prohead-i structure of bacteriophage hk97: Implications for scaffold-mediated control of particle assembly and maturation. *Journal of Molecular Biology*, 408(3):541–554, 2011. URL: http://www.sciencedirect.com/science/article/pii/S0022283611000337, doi:10.1016/j.jmb.2011.01.016.

[175] B. Zakeri, J. O. Fierer, E. Celik, E. C. Chittock, U. Schwarz-Linek, V. T. Moy, and M. Howarth. Peptide tag forming a rapid covalent bond to a protein, through engineering a bacterial adhesin. *Proceedings of the National Academy of Sciences*, 109(12):E690, 2012. doi:10.1073/pnas.1115485109.

[176] T. W. Giessen. Encapsulins: microbial nanocompartments with applications in biomedicine, nanobiotechnology and materials science. *Curr. Opin. Chem. Biol.*, 34:1–10, 2016. URL: http://dx.doi.org/10.1016/j.cbpa.2016.05.013https://www.ncbi.nlm.nih.gov/pubmed/27232770https://linkinghub.elsevier.com/retrieve/pii/S1367-5931(16)30053-9, doi:10.1016/j.cbpa.2016.05.013.

[177] G. Veggiani, T. Nakamura, M. D. Brenner, R. V. Gayet, J. Yan, C. V. Robinson, and M. Howarth. Programmable polyproteams built using twin peptide superglues. *Proceedings of the National Academy of Sciences*, 113(5):1202, 2016. doi:10.1073/pnas.1519214113.

[178] H. Gradišar, S. Božič, T. Doles, D. Vengust, I. Hafner-Bratkovič, A. Mertelj, B. Webb, A. Šali, S. Klavžar, and R. Jerala. Design of a single-chain polypeptide tetrahedron assembled from coiled-coil segments. *Nature Chemical Biology*, 9:362 EP –, 2013. URL: https://doi.org/10.1038/nchembio.1248, doi:10.1038/nchembio.1248.

[179] A. Ljubetič, F. Lapenta, H. Gradišar, I. Drobnak, J. Aupič, Ž. Strmšek, D. Lainšček, I. Hafner-Bratkovič, A. Majerle, N. Krivec, M. Benčina, T. Pisanski, T. Ć. Veličković, A. Round, J. M. Carazo, R. Melero, and R. Jerala. Design of coiled-coil protein-origami cages that self-assemble in vitro and in vivo. *Nature Biotechnology*, 35:1094 EP –, 2017. URL: https://doi.org/10.1038/nbt.3994, doi:10.1038/nbt.3994.

[180] F. Lapenta, J. Aupič, Ž. Strmšek, and R. Jerala. Coiled coil protein origami: from modular design principles towards biotechnological applications. *Chemical Society reviews*, 47(10):3530–3542, 2018. URL: http://dx.doi.org/10.1039/C7CS00822H, doi:10.1039/C7CS00822H.

[181] I. Wheeldon, S. D. Minteer, S. Banta, S. C. Barton, P. Atanassov, and M. Sigman. Substrate channelling as an approach to cascade reactions. *Nature Chemistry*, 8:299 EP –, 2016. URL: https://doi.org/10.1038/nchem.2459, doi:10.1038/nchem.2459.

[182] J. P. Liuzzi, F. Aydemir, H. Nam, M. D. Knutson, and R. J. Cousins. Zip14 (slc39a14) mediates non-transferrin-bound iron uptake into cells. *Proceedings of the National Academy of Sciences*, 103(37):13612, 2006. doi:10.1073/pnas.0606424103.

[183] S. R. Jones, T. D. Wilson, M. E. Brown, L. Rahn-Lee, Y. Yu, L. L. Fredriksen, E. Ozyamak, A. Komeili, and M. C. Y. Chang. Genetic and biochemical investigations of the role of mamp in redox control of iron biomineralization in magnetospirillum magneticum. *Proc. Natl. Acad. Sci. U. S. A.*, 112(13):3904–3909, 2015. URL: http://dx.doi.org/10.1073/pnas.1417614112https://www.ncbi.nlm.nih.gov/pubmed/25775527https://www.ncbi.nlm.nih.

gov/pmc/articles/PMC4386411http://www.pnas.org/cgi/pmidlookup?view=long&pmid=25775527, doi:10.1073/pnas.1417614112.

[184] A. Yamagishi, M. Tanaka, J. J. M. Lenders, J. Thiesbrummel, Sommerdijk, Nico A. J. M., T. Matsunaga, and A. Arakaki. Control of magnetite nanocrystal morphology in magnetotactic bacteria by regulation of mms7 gene expression. *Scientific Reports*, 6:29785 EP –, 2016. URL: https://doi.org/10.1038/srep29785, doi:10.1038/srep29785.

[185] A. Arakaki, A. Yamagishi, A. Fukuyo, M. Tanaka, and T. Matsunaga. Coordinated functions of mms proteins define the surface structure of cubo-octahedral magnetite crystals in magnetotactic bacteria. *Molecular Microbiology*, 93(3):554–567, 2014. doi:10.1111/mmi.12683.

[186] M. Radoul, L. Lewin, B. Cohen, R. Oren, S. Popov, G. Davidov, M. H. Vandsburger, A. Harmelin, R. Bitton, J.-M. Greneche, M. Neeman, and R. Zarivach. Genetic manipulation of iron biomineralization enhances mr relaxivity in a ferritin-m6a chimeric complex. *Scientific Reports*, 6:26550 EP –, 2016. URL: https://doi.org/10.1038/srep26550, doi:10.1038/srep26550.

[187] C. C. Winterbourn. Toxicity of iron and hydrogen peroxide: the fenton reaction. *Toxicology Letters*, 82-83:969–974, 1995. URL: http://www.sciencedirect.com/science/article/pii/037842749503532X, doi:10.1016/0378-4274(95)03532-X.

[188] R. E. London, G. Toney, S. A. Gabel, and A. Funk. Magnetic resonance imaging studies of the brains of anesthetized rats treated with manganese chloride. *Brain Research Bulletin*, 23(3):229–235, 1989. URL: http://www.sciencedirect.com/science/article/pii/0361923089901524, doi:10.1016/0361-9230(89)90152-4.

[189] A. P. Koretsky and A. C. Silva. Manganese-enhanced magnetic resonance imaging (memri). *NMR in Biomedicine*, 17(8):527–531, 2004. doi:10.1002/nbm.940.

[190] X. Yu, Y. Z. Wadghiri, D. H. Sanes, and D. H. Turnbull. In vivo auditory brain mapping in mice with mn-enhanced mri. *Nature Neuroscience*, 8:961 EP –, 2005. URL: https://doi.org/10.1038/nn1477, doi:10.1038/nn1477.

[191] C. A. Romano, M. Zhou, Y. Song, V. H. Wysocki, A. C. Dohnalkova, L. Kovarik, L. Paša-Tolić, and B. M. Tebo. Biogenic manganese oxide nanoparticle formation by a multimeric multicopper oxidase mnx. *Nat. Commun.*, 8(1):746, 2017. URL: https://doi.org/10.1038/s41467-017-00896-8, doi:10.1038/s41467-017-00896-8.

[192] M. k. Maruthamuthu, V. Selvamani, S. P. Nadarajan, H. Yun, Y.-K. Oh, G. T. Eom, and S. H. Hong. Manganese and cobalt recovery by surface display of metal binding peptide on various loops of ompc in escherichia coli. *Journal of Industrial*

Microbiology & Biotechnology, 45(1):31–41, 2018. URL: https://doi.org/10.1007/s10295-017-1989-x, doi:10.1007/s10295-017-1989-x.

[193] D. Bar-Or, G. Curtis, N. Rao, N. Bampos, and E. Lau. Characterization of the co2+ and ni2+ binding amino-acid residues of the n-terminus of human albumin. *European Journal of Biochemistry*, 268(1):42–48, 2001. doi:10.1046/j.1432-1327.2001.01846.x.

[194] J. Dong, C. Liu, J. Zhang, Z.-T. Xin, G. Yang, B. Gao, C.-q. Mao, N.-L. Liu, F. Wang, N.-S. Shao, M. Fan, and Y.-N. Xue. Selection of novel nickel-binding peptides from flagella displayed secondary peptide library. *Chemical Biology & Drug Design*, 68(2):107–112, 2006. doi:10.1111/j.1747-0285.2006.00421.x.

[195] G. Marassio, T. Prangé, H. N. David, J. Sopkova-de Oliveira Santos, L. Gabison, N. Delcroix, J. H. Abraini, and N. Colloc'h. Pressure-response analysis of anesthetic gases xenon and nitrous oxide on urate oxidase: a crystallographic study. *The FASEB Journal*, 25(7):2266–2275, 2011. doi:10.1096/fj.11-183046.

[196] S. M. Rubin, S.-Y. Lee, E. Ruiz, A. Pines, and D. E. Wemmer. Detection and characterization of xenon-binding sites in proteins by 129xe nmr spectroscopy. *Journal of Molecular Biology*, 322(2):425–440, 2002. URL: http://www.sciencedirect.com/science/article/pii/S0022283602007398, doi:10.1016/S0022-2836(02)00739-8.

[197] Q. Wang, C. P. Mercogliano, and J. Löwe. A ferritin-based label for cellular electron cryotomography. *Structure*, 19(2):147–154, 2011. URL: http://dx.doi.org/10.1016/j.str.2010.12.002https://www.ncbi.nlm.nih.gov/pubmed/21300284https://linkinghub.elsevier.com/retrieve/pii/S0969-2126(10)00438-7, doi:10.1016/j.str.2010.12.002.

[198] N. I. Clarke and S. J. Royle. Ferritag is a new genetically-encoded inducible tag for correlative light-electron microscopy. *Nat. Commun.*, 9(1):2604, 2018. URL: https://doi.org/10.1038/s41467-018-04993-0, doi:10.1038/s41467-018-04993-0.

[199] J. Livet, T. A. Weissman, H. Kang, R. W. Draft, J. Lu, R. A. Bennis, J. R. Sanes, and J. W. Lichtman. Transgenic strategies for combinatorial expression of fluorescent proteins in the nervous system. *Nature*, 450:56 EP –, 2007. URL: https://doi.org/10.1038/nature06293, doi:10.1038/nature06293.

[200] D. Cai, K. B. Cohen, T. Luo, J. W. Lichtman, and J. R. Sanes. Improved tools for the brainbow toolbox. *Nature Methods*, 10:540 EP –, 2013. URL: https://doi.org/10.1038/nmeth.2450, doi:10.1038/nmeth.2450.

[201] A. Apolloni, I. A. Prior, M. Lindsay, R. G. Parton, and J. F. Hancock. H-ras but not k-ras traffics to the plasma membrane through the exocytic pathway. *Molecular and cellular biology*, 20(7):2475–2487, 2000. URL: https://www.ncbi.nlm.nih.gov/pubmed/10713171.

[202] M. Helmstaedter. Cellular-resolution connectomics: challenges of dense neural circuit reconstruction. *Nature Methods*, 10:501 EP –, 2013. URL: https://doi.org/10.1038/nmeth.2476, doi:10.1038/nmeth.2476.

[203] M. Pak and S. Kim, editors. *A review of deep learning in image recognition: 2017 4th International Conference on Computer Applications and Information Processing Technology (CAIPT)*, 2017. doi:10.1109/CAIPT.2017.8320684.

[204] Tran Minh Quan, David G. C. Hildebrand, and Won-Ki Jeong. Fusionnet: A deep fully residual convolutional neural network for image segmentation in connectomics. *CoRR*, abs/1612.05360, 2016.

[205] D. F. Green, A. T. Dennis, P. S. Fam, B. Tidor, and A. Jasanoff. Rational design of new binding specificity by simultaneous mutagenesis of calmodulin and a target peptide. *Biochemistry*, 45(41):12547–12559, 2006. URL: https://www.ncbi.nlm.nih.gov/pubmed/17029410, doi:10.1021/bi060857u.

[206] E. Rodriguez, V. S. Lelyveld, T. Atanasijevic, S. Okada, and A. Jasanoff. Magnetic nanosensors optimized for rapid and reversible self-assembly. *Chem. Commun.*, 50(27):3595–3598, 2014. URL: http://dx.doi.org/10.1039/C4CC00314D, doi:10.1039/C4CC00314D.

[207] M. Mank, A. F. Santos, S. Direnberger, T. D. Mrsic-Flogel, S. B. Hofer, V. Stein, T. Hendel, D. F. Reiff, C. Levelt, A. Borst, T. Bonhoeffer, M. Hübener, and O. Griesbeck. A genetically encoded calcium indicator for chronic in vivo two-photon imaging. *Nature Methods*, 5:805 EP –, 2008. URL: https://doi.org/10.1038/nmeth.1243, doi:10.1038/nmeth.1243.

[208] T. Thestrup, J. Litzlbauer, I. Bartholomäus, M. Mues, L. Russo, H. Dana, Y. Kovalchuk, Y. Liang, G. Kalamakis, Y. Laukat, S. Becker, G. Witte, A. Geiger, T. Allen, L. C. Rome, T.-W. Chen, D. S. Kim, O. Garaschuk, C. Griesinger, and O. Griesbeck. Optimized ratiometric calcium sensors for functional in vivo imaging of neurons and t lymphocytes. *Nature Methods*, 11:175 EP –, 2014. URL: https://doi.org/10.1038/nmeth.2773, doi:10.1038/nmeth.2773.

[209] A. Kalinowski, Z. Qin, K. Coffey, R. Kodali, M. J. Buehler, M. Lösche, and K. N. Dahl. Calcium causes a conformational change in lamin a tail domain that promotes farnesyl-mediated membrane association. *Biophysical journal*, 104(10):2246–2253, 2013. URL: https://www.ncbi.nlm.nih.gov/pubmed/23708364, doi:10.1016/j.bpj.2013.04.016.

[210] A. S. Saini and J. S. Melo. Biosorption of uranium by melanin: Kinetic, equilibrium and thermodynamic studies. *Bioresource Technology*, 149:155–162, 2013. URL: http://www.sciencedirect.com/science/article/pii/S0960852413014582, doi:10.1016/j.biortech.2013.09.034.

[211] L. Zhou, M. Bosscher, C. Zhang, S. Özçubukçu, L. Zhang, W. Zhang, C. J. Li, J. Liu, M. P. Jensen, L. Lai, and C. He. A protein engineered to bind uranyl selectively and with femtomolar affinity. *Nature Chemistry*, 6:236 EP –, 2014. URL: https://doi.org/10.1038/nchem.1856, doi:10.1038/nchem.1856.

[212] S. O. Odoh, G. D. Bondarevsky, J. Karpus, Q. Cui, C. He, R. Spezia, and L. Gagliardi. Uo22+ uptake by proteins: Understanding the binding features of the super uranyl binding protein and design of a protein with higher affinity. *J. Am. Chem. Soc.*, 136(50):17484–17494, 2014. doi:10.1021/ja5087563.

[213] Y. Yang, N. Liu, Y. He, Y. Liu, L. Ge, L. Zou, S. Song, W. Xiong, and X. Liu. Improved calcium sensor gcamp-x overcomes the calcium channel perturbations induced by the calmodulin in gcamp. *Nat. Commun.*, 9(1):1504, 2018. URL: https://doi.org/10.1038/s41467-018-03719-6, doi:10.1038/s41467-018-03719-6.

[214] H. C. Gonick. Lead-binding proteins: a review. *Journal of Toxicology*, 2011:686050, 2011. doi:10.1155/2011/686050.

[215] U. Kühn and E. Wahle. Structure and function of poly(a) binding proteins. *Biochimica et Biophysica Acta (BBA) - Gene Structure and Expression*, 1678(2):67–84, 2004. URL: http://www.sciencedirect.com/science/article/pii/S016747810400079X, doi:10.1016/j.bbaexp.2004.03.008.

[216] A. A. Smargon, D. B. Cox, N. K. Pyzocha, K. Zheng, I. M. Slaymaker, J. S. Gootenberg, O. A. Abudayyeh, P. Essletzbichler, S. Shmakov, K. S. Makarova, E. V. Koonin, and F. Zhang. Cas13b is a type vi-b crispr-associated rna-guided rnase differentially regulated by accessory proteins csx27 and csx28. *Molecular Cell*, 65(4):618–630.e7, 2017. doi:10.1016/j.molcel.2016.12.023.

[217] S. Muyldermans. Nanobodies: Natural single-domain antibodies. *Annual Review of Biochemistry*, 82(1):775–797, 2013. doi:10.1146/annurev-biochem-063011-092449.

[218] D. G. Graham, S. M. Tiffany, and F. S. Vogel. The toxicity of melanin precursors. *Journal of Investigative Dermatology*, 70(2):113–116, 1978. URL: http://www.sciencedirect.com/science/article/pii/S0022202X1545211X, doi:10.1111/1523-1747.ep12541249.

[219] G. Raposo and M. S. Marks. Melanosomes–dark organelles enlighten endosomal membrane transport. *Nat. Rev. Mol. Cell Biol.*, 8(10):786–797, 2007. URL: http://dx.doi.org/10.1038/nrm2258https://www.ncbi.nlm.nih.gov/pubmed/17878918https://www.ncbi.nlm.nih.gov/pmc/articles/PMC2786984https://www.ncbi.nlm.nih.gov/pmc/articles/PMC2786984/, doi:10.1038/nrm2258.

[220] Y. Uda, Y. Goto, S. Oda, T. Kohchi, M. Matsuda, and K. Aoki. Efficient synthesis of phycocyanobilin in mammalian cells for optogenetic control of cell signaling.

Proceedings of the National Academy of Sciences, 114(45):11962, 2017. doi:10.1073/pnas.1707190114.

[221] K. Müller, R. Engesser, J. Timmer, F. Nagy, M. D. Zurbriggen, and W. Weber. Synthesis of phycocyanobilin in mammalian cells. *Chem. Commun.*, 49(79):8970–8972, 2013. URL: http://dx.doi.org/10.1039/C3CC45065A, doi:10.1039/C3CC45065A.

[222] A. Lauri, D. Soliman, M. Omar, A. Stelzl, V. Ntziachristos, and G. G. Westmeyer. Photoacoustic pigment relocalization sensor. *bioRxiv*, page 455022, 2018. doi:10.1101/455022.

[223] S. Asano, B. D. Engel, and W. Baumeister. In situ cryo-electron tomography: A post-reductionist approach to structural biology. *Journal of Molecular Biology*, 428(2, Part A):332–343, 2016. URL: http://www.sciencedirect.com/science/article/pii/S0022283615005537, doi:10.1016/j.jmb.2015.09.030.

[224] R. F. Thompson, M. Walker, C. A. Siebert, S. P. Muench, and N. A. Ranson. An introduction to sample preparation and imaging by cryo-electron microscopy for structural biology. *Methods*, 100:3–15, 2016. URL: http://www.sciencedirect.com/science/article/pii/S1046202316300330, doi:10.1016/j.ymeth.2016.02.017.

[225] H. Ma, J. Xu, J. Jin, Y. Huang, and Y. Liu. A simple marker-assisted 3d nanometer drift correction method for superresolution microscopy. *Biophysical journal*, 112(10):2196–2208, 2017. URL: http://www.sciencedirect.com/science/article/pii/S0006349517304411, doi:10.1016/j.bpj.2017.04.025.

[226] M. G. Paez-Segala, M. G. Sun, G. Shtengel, S. Viswanathan, M. A. Baird, J. J. Macklin, R. Patel, J. R. Allen, E. S. Howe, G. Piszczek, H. F. Hess, M. W. Davidson, Y. Wang, and L. L. Looger. Fixation-resistant photoactivatable fluorescent proteins for clem. *Nat. Methods*, 12(3):215–8, 4 p following 218, 2015. URL: http://dx.doi.org/10.1038/nmeth.3225https://www.ncbi.nlm.nih.gov/pubmed/25581799https://www.ncbi.nlm.nih.gov/pmc/articles/PMC4344411, doi:10.1038/nmeth.3225.

[227] W. Muranyi, S. Malkusch, B. Müller, M. Heilemann, and H.-G. Kräusslich. Super-resolution microscopy reveals specific recruitment of hiv-1 envelope proteins to viral assembly sites dependent on the envelope c-terminal tail. *PLOS Pathogens*, 9(2):e1003198, 2013. URL: https://doi.org/10.1371/journal.ppat.1003198, doi:10.1371/journal.ppat.1003198.

[228] L. Tian, S. A. Hires, T. Mao, D. Huber, M. E. Chiappe, S. H. Chalasani, L. Petreanu, J. Akerboom, S. A. McKinney, E. R. Schreiter, C. I. Bargmann, V. Jayaraman, K. Svoboda, and L. L. Looger. Imaging neural activity in worms, flies and mice with improved gcamp calcium indicators. *Nature Methods*, 6:875 EP –, 2009. URL: https://doi.org/10.1038/nmeth.1398, doi:10.1038/nmeth.1398.

[229] T. Kim, D. Moore, and M. Fussenegger. Genetically programmed superparamagnetic behavior of mammalian cells. *Journal of Biotechnology*, 162(2):237–245, 2012. URL: http://www.sciencedirect.com/science/article/pii/S0168165612006736, doi:10.1016/j.jbiotec.2012.09.019.

[230] D. A. Bazylinski and R. B. Frankel. Magnetosome formation in prokaryotes. *Nature Reviews Microbiology*, 2:217 EP –, 2004. URL: https://doi.org/10.1038/nrmicro842, doi:10.1038/nrmicro842.

[231] T. Ahn, J. H. Kim, H.-M. Yang, J. W. Lee, and J.-D. Kim. Formation pathways of magnetite nanoparticles by coprecipitation method. *The Journal of Physical Chemistry C*, 116(10):6069–6076, 2012. doi:10.1021/jp211843g.

[232] E. Del Grosso, A.-M. Dallaire, A. Vallée-Bélisle, and F. Ricci. Enzyme-operated dna-based nanodevices. *Nano Letters*, 15(12):8407–8411, 2015. doi:10.1021/acs.nanolett.5b04566.

[233] A. Idili, A. Vallée-Bélisle, and F. Ricci. Programmable ph-triggered dna nanoswitches. *J. Am. Chem. Soc.*, 136(16):5836–5839, 2014. doi:10.1021/ja500619w.

[234] M. L. Fdez-Gubieda, A. Muela, J. Alonso, A. García-Prieto, L. Olivi, R. Fernández-Pacheco, and J. M. Barandiarán. Magnetite biomineralization in magnetospirillum gryphiswaldense: Time-resolved magnetic and structural studies. *ACS Nano*, 7(4):3297–3305, 2013. doi:10.1021/nn3059983.

[235] J. Baumgartner, G. Morin, N. Menguy, T. Perez Gonzalez, M. Widdrat, J. Cosmidis, and D. Faivre. Magnetotactic bacteria form magnetite from a phosphate-rich ferric hydroxide via nanometric ferric (oxyhydr)oxide intermediates. *Proc. Natl. Acad. Sci. U. S. A.*, 110(37):14883–14888, 2013. URL: https://www.ncbi.nlm.nih.gov/pubmed/23980143, doi:10.1073/pnas.1307119110.

[236] J. L. Kirschvink and H. A. Lowenstam. Mineralization and magnetization of chiton teeth: paleomagnetic, sedimentologic, and biologic implications of organic magnetite. *Earth and Planetary Science Letters*, 44(2):193–204, 1979. URL: http://www.sciencedirect.com/science/article/pii/0012821X79901687, doi:10.1016/0012-821X(79)90168-7.

[237] L. M. Gordon, J. K. Román, R. M. Everly, M. J. Cohen, J. J. Wilker, and D. Joester. Selective formation of metastable ferrihydrite in the chiton tooth. *Angew. Chem. Int. Ed Engl.*, 53(43):11506–11509, 2014. doi:10.1002/anie.201406131.

[238] Y. Noguchi, T. Fujiwara, K. Yoshimatsu, and Y. Fukumori. Iron reductase for magnetite synthesis in the magnetotactic bacterium magnetospirillum magnetotacticum. *Journal of bacteriology*, 181(7):2142–2147, 1999. URL: https://www.ncbi.nlm.nih.gov/pubmed/10094692.

[239] G. T. Hess, L. Frésard, K. Han, C. H. Lee, A. Li, K. A. Cimprich, S. B. Montgomery, and M. C. Bassik. Directed evolution using dcas9-targeted somatic hypermutation in mammalian cells. *Nature Methods*, 13:1036 EP –, 2016. URL: https://doi.org/10.1038/nmeth.4038, doi:10.1038/nmeth.4038.

[240] Y. Zong, Y. Wang, C. Li, R. Zhang, K. Chen, Y. Ran, J.-L. Qiu, D. Wang, and C. Gao. Precise base editing in rice, wheat and maize with a cas9-cytidine deaminase fusion. *Nature Biotechnology*, 35:438 EP –, 2017. URL: https://doi.org/10.1038/nbt.3811, doi:10.1038/nbt.3811.

[241] C. H. June, R. S. O'Connor, O. U. Kawalekar, S. Ghassemi, and M. C. Milone. Car t cell immunotherapy for human cancer. *Science*, 359(6382):1361, 2018. doi:10.1126/science.aar6711.

[242] N. Emami-Shahri, J. Foster, R. Kashani, P. Gazinska, C. Cook, J. Sosabowski, J. Maher, and S. Papa. Clinically compliant spatial and temporal imaging of chimeric antigen receptor t-cells. *Nat. Commun.*, 9(1):1081, 2018. URL: https://doi.org/10.1038/s41467-018-03524-1, doi:10.1038/s41467-018-03524-1.

[243] L. Liu, D. Sommermeyer, A. Cabanov, P. Kosasih, T. Hill, and S. R. Riddell. Inclusion of strep-tag ii in design of antigen receptors for t-cell immunotherapy. *Nature Biotechnology*, 34:430 EP –, 2016. URL: https://doi.org/10.1038/nbt.3461, doi:10.1038/nbt.3461.

[244] A. V. Pinheiro, D. Han, W. M. Shih, and H. Yan. Challenges and opportunities for structural dna nanotechnology. *Nature Nanotechnology*, 6:763 EP –, 2011. URL: https://doi.org/10.1038/nnano.2011.187, doi:10.1038/nnano.2011.187.

[245] V. Linko, A. Ora, and M. A. Kostiainen. Dna nanostructures as smart drug-delivery vehicles and molecular devices. *Trends in Biotechnology*, 33(10):586–594, 2015. doi:10.1016/j.tibtech.2015.08.001.

[246] F. Praetorius, B. Kick, K. L. Behler, M. N. Honemann, D. Weuster-Botz, and H. Dietz. Biotechnological mass production of dna origami. *Nature*, 552:84 EP –, 2017. URL: https://doi.org/10.1038/nature24650, doi:10.1038/nature24650.

[247] S. Maday, A. E. Twelvetrees, A. J. Moughamian, and E. L. F. Holzbaur. Axonal transport: cargo-specific mechanisms of motility and regulation. *Neuron*, 84(2):292–309, 2014. URL: https://www.ncbi.nlm.nih.gov/pubmed/25374356, doi:10.1016/j.neuron.2014.10.019.

[248] P. K. Kim and E. H. Hettema. Multiple pathways for protein transport to peroxisomes. *Journal of Molecular Biology*, 427(6 Pt A):1176–1190, 2015. URL: https://www.ncbi.nlm.nih.gov/pubmed/25681696, doi:10.1016/j.jmb.2015.02.005.

[249] F. Ardito, M. Giuliani, D. Perrone, G. Troiano, and L. Lo Muzio. The crucial role of protein phosphorylation in cell signaling and its use as targeted therapy (review). *International journal of molecular medicine*, 40(2):271–280, 2017. URL: https://www.ncbi.nlm.nih.gov/pubmed/28656226, doi:10.3892/ijmm.2017.3036.

[250] T. Pawson and J. D. Scott. Protein phosphorylation in signaling – 50 years and counting. *Trends in Biochemical Sciences*, 30(6):286–290, 2005. doi:10.1016/j.tibs.2005.04.013.

[251] J. Snijder, R. J. Rose, D. Veesler, J. E. Johnson, and A. J. R. Heck. Studying 18 mda virus assemblies with native mass spectrometry. *Angew. Chem. Int. Ed Engl.*, 52(14):4020–4023, 2013. URL: https://www.ncbi.nlm.nih.gov/pubmed/23450509, doi:10.1002/anie.201210197.

[252] D. D. de Carvalho, F. T. Costa, N. Duran, and M. Haun. Cytotoxic activity of violacein in human colon cancer cells. *Toxicology in Vitro*, 20(8):1514–1521, 2006. URL: http://www.sciencedirect.com/science/article/pii/S0887233306001202, doi:10.1016/j.tiv.2006.06.007.

[253] D. Platt, S. Amara, T. Mehta, K. Vercuyssee, E. L. Myles, T. Johnson, and V. Tiriveedhi. Violacein inhibits matrix metalloproteinase mediated cxcr4 expression: potential anti-tumor effect in cancer invasion and metastasis. *Biochemical and Biophysical Research Communications*, 455(1-2):107–112, 2014. URL: https://www.ncbi.nlm.nih.gov/pubmed/25450700, doi:10.1016/j.bbrc.2014.10.124.

[254] S. M. Hashimi, T. Xu, and M. Q. Wei. Violacein anticancer activity is enhanced under hypoxia. *Oncology reports*, 33(4):1731–1736, 2015. doi:10.3892/or.2015.3781.

[255] J. S. Lindsey, O. Mass, and C.-Y. Chen. Tapping the near-infrared spectral region with bacteriochlorin arrays. *New Journal of Chemistry*, 35(3):511–516, 2011. URL: http://dx.doi.org/10.1039/C0NJ00977F, doi:10.1039/C0NJ00977F.

[256] P. Vairaprakash, E. Yang, T. Sahin, M. Taniguchi, M. Krayer, J. R. Diers, A. Wang, D. M. Niedzwiedzki, C. Kirmaier, J. S. Lindsey, D. F. Bocian, and D. Holten. Extending the short and long wavelength limits of bacteriochlorin near-infrared absorption via dioxo- and bisimide-functionalization. *The Journal of Physical Chemistry B*, 119(12):4382–4395, 2015. doi:10.1021/jp512818g.

[257] A. G. M. Chew and D. A. Bryant. Chlorophyll biosynthesis in bacteria: The origins of structural and functional diversity. *Annual Review of Microbiology*, 61(1):113–129, 2007. doi:10.1146/annurev.micro.61.080706.093242.

[258] G. Giesbers, J. van Schenck, S. Vega Gutierrez, S. Robinson, and O. Ostroverkhova. Fungi-derived pigments for sustainable organic (opto)electronics. *MRS Advances*, 3(59):3459–3464, 2018. doi:10.1557/adv.2018.446.

[259] J. Akerboom, J. D. V. Rivera, M. M. R. Guilbe, E. C. A. Malavé, H. H. Hernandez, L. Tian, S. A. Hires, J. S. Marvin, L. L. Looger, and E. R. Schreiter. Crystal structures of the gcamp calcium sensor reveal the mechanism of fluorescence signal change and aid rational design. *Journal of Biological Chemistry*, 284(10):6455–6464, 2009. doi:10.1074/jbc.M807657200.

[260] M. Gunkel, F. Erdel, K. Rippe, P. Lemmer, R. Kaufmann, C. Hörmann, R. Amberger, and C. Cremer. Dual color localization microscopy of cellular nanostructures. *Biotechnology Journal*, 4(6):927–938, 2009. doi:10.1002/biot.200900005.

[261] F. L. Tansi, R. Rüger, A. M. Kollmeier, M. Rabenhold, F. Steiniger, R. E. Kontermann, U. K. Teichgraeber, A. Fahr, and I. Hilger. Endoglin based in vivo near-infrared fluorescence imaging of tumor models in mice using activatable liposomes. *Biochimica et Biophysica Acta (BBA) - General Subjects*, 1862(6):1389–1400, 2018. URL: http://www.sciencedirect.com/science/article/pii/S0304416518300746, doi:10.1016/j.bbagen.2018.03.012.

[262] L. Valon, A. Marín-Llauradó, T. Wyatt, G. Charras, and X. Trepat. Optogenetic control of cellular forces and mechanotransduction. *Nat. Commun.*, 8:14396, 2017. URL: https://www.ncbi.nlm.nih.gov/pubmed/28186127, doi:10.1038/ncomms14396.

[263] E. C. Pama, L. Colzato, and B. Hommel. Optogenetics as a neuromodulation tool in cognitive neuroscience. *Frontiers in Psychology*, 4:610, 2013. URL: https://www.frontiersin.org/article/10.3389/fpsyg.2013.00610, doi:10.3389/fpsyg.2013.00610.

[264] A. Krumholz, D. M. Shcherbakova, J. Xia, L. V. Wang, and V. V. Verkhusha. Multicontrast photoacoustic in vivo imaging using near-infrared fluorescent proteins. *Scientific Reports*, 4:3939 EP –, 2014. URL: https://doi.org/10.1038/srep03939, doi:10.1038/srep03939.

[265] R. Chen, G. Romero, M. G. Christiansen, A. Mohr, and P. Anikeeva. Wireless magnetothermal deep brain stimulation. *Science*, 347(6229):1477, 2015. doi:10.1126/science.1261821.

[266] X. Luís Deán-Ben and D. Razansky. Adding fifth dimension to optoacoustic imaging: volumetric time-resolved spectrally enriched tomography. *Light: Science &Amp; Applications*, 3:e137 EP –, 2014. URL: https://doi.org/10.1038/lsa.2014.18, doi:10.1038/lsa.2014.18.

[267] W. J. Tyler, S. W. Lani, and G. M. Hwang. Ultrasonic modulation of neural circuit activity. *Current Opinion in Neurobiology*, 50:222–231, 2018. URL: http://www.sciencedirect.com/science/article/pii/S0959438817302015, doi:10.1016/j.conb.2018.04.011.

[268] S. S. Kang, S. H. Shin, C.-K. Auh, and J. Chun. Human skeletal dysplasia caused by a constitutive activated transient receptor potential vanilloid 4 (trpv4) cation channel mutation. *Experimental &Amp; Molecular Medicine*, 44:707 EP –, 2012. URL: https://doi.org/10.3858/emm.2012.44.12.080, doi:10.3858/emm.2012.44.12.080.

[269] J. Foiret, H. Zhang, T. Ilovitsh, L. Mahakian, S. Tam, and K. W. Ferrara. Ultrasound localization microscopy to image and assess microvasculature in a rat kidney. *Sci. Rep.*, 7(1):13662, 2017. URL: https://doi.org/10.1038/s41598-017-13676-7, doi:10.1038/s41598-017-13676-7.

[270] E. M. Brustad, V. S. Lelyveld, C. D. Snow, N. Crook, S. T. Jung, F. M. Martinez, T. J. Scholl, A. Jasanoff, and F. H. Arnold. Structure-guided directed evolution of highly selective p450-based magnetic resonance imaging sensors for dopamine and serotonin. *Journal of Molecular Biology*, 422(2):245–262, 2012. URL: http://www.sciencedirect.com/science/article/pii/S0022283612004275, doi:10.1016/j.jmb.2012.05.029.

[271] B. Iordanova, T. K. Hitchens, C. S. Robison, and E. T. Ahrens. Engineered mitochondrial ferritin as a magnetic resonance imaging reporter in mouse olfactory epithelium. *PLoS One*, 8(8):e72720, 2013. URL: https://doi.org/10.1371/journal.pone.0072720, doi:10.1371/journal.pone.0072720.

[272] F. L. Langhauser, P. M. Heiler, S. Grudzenski, A. Lemke, A. Alonso, L. R. Schad, M. G. Hennerici, S. Meairs, and M. Fatar. Thromboembolic stroke in c57bl/6 mice monitored by 9.4 t mri using a 1h cryo probe. *Experimental & Translational Stroke Medicine*, 4(1):18, 2012. URL: https://doi.org/10.1186/2040-7378-4-18, doi:10.1186/2040-7378-4-18.

[273] H. Zhao, J. Wang, Z. Lu, Q. Wu, H. Lv, H. Liu, and X. Gong. Superficial siderosis of the central nervous system induced by a single-episode of traumatic subarachnoid hemorrhage: A study using mri-enhanced gradient echo t2 star-weighted angiography. *PLoS One*, 10(2):e0116632, 2015. URL: https://doi.org/10.1371/journal.pone.0116632, doi:10.1371/journal.pone.0116632.

[274] E. C. Abenojar, S. Wickramasinghe, J. Bas-Concepcion, and A. C. S. Samia. Structural effects on the magnetic hyperthermia properties of iron oxide nanoparticles. *Progress in Natural Science: Materials International*, 26(5):440–448, 2016. URL: http://www.sciencedirect.com/science/article/pii/S1002007116300995, doi:10.1016/j.pnsc.2016.09.004.

[275] S. Nimpf and D. A. Keays. Is magnetogenetics the new optogenetics? *The EMBO Journal*, 36(12):1643, 2017. doi:10.15252/embj.201797177.

A Appendix

Please note that the appended first author publications are licensed under the Creative Commons Attribution 4.0 International License and thus do not require any further permission to be used in this cumulative dissertation.

Imagery in Figure 3.1 and 3.2 was taken from the the following publications licensed under the Creative Commons Attribution and do not require further permission for reproduction: Akerboom *et al.*, 2009 [259], Gunkel*et al.*, 2009 [260], Tansi *et al.*, 2018 [261], Valon *et al.*, 2017 [262], Pama *et al.*, 2013 [263], Paproski *et al.*, 2014 [35], Krumholz *et al.*, 2014 [264], Chen *et al.*, 2015 [265], Herzog *et al.*, 2012 [22], Deán-Ben *et al.*, 2014 [266], Tyler *et al.*, 2018 [267], Ibsen *et al.*, 2015 [131], Kang *et al.*, 2012 [268], Bourdeau *et al.*, 2018, Shapirop *et al.*, 2014 [68], Foiret *et al.*, 2017 [269], Brustad *et al.*, 2012 [270], Iordonova *et al.*, 2013 [271], Langhauser *et al.*, 2012 [272], Zhao *et al.*, 2015 [273], Abenojar *et al.*, 2016 [274], Wu *et al.*, 2016 [127], Nimpf *et al.*, 2017 [275] and Held *et al.*, 2016 [162].

The renderings of the protein compartments as shown in Figure 3.2 were produced using UCSF Chimera and the respective PDB file.

The bibliography appended to this document contains all literature referenced in the introduction and discussion. Please note that some of the references can be already contained in the bibliography of the first author publications Sigmund *et al.*, 2018 or Jiang, Sigmund *et al.*, 2015.